Thermal spray as a processing tool for the functional oxides

A Dissertation Presented

by

Su Jung Han

to

The Graduate School

in Partial Fulfillment of the

Requirements

for the Degree of

Doctor of Philosophy

in

Materials Science and Engineering

Stony Brook University

December 2015

Stony Brook University

The Graduate School

Su Jung Han

We, the dissertation committee for the above candidate for the

Doctor of Philosophy degree, hereby recommend

acceptance of this dissertation.

Prof. Sanjay Sampath – Dissertation Advisor
Distinguished Professor, Materials Science and Engineering

Prof. David O. Welch – Dissertation Examining Committee Chair
Adjunct Professor, Materials Science and Engineering

Prof. Jason Trelewicz
Assistant Professor, Materials Science and Engineering

Dr. Jeff Brogan
CEO, MesoScribe Technologies, Inc.

This dissertation is accepted by the Graduate School

Charles Taber
Dean of the Graduate School

Abstract of the Dissertation

Thermal spray as a processing tool for the functional oxides

by

Su Jung Han

Doctor of Philosophy

in

Materials Science and Engineering

Stony Brook University

2015

Functional oxides are important classes of materials that show a wide range of electrical and magnetic behaviors for electronics, sensors and energy harvesting/storage applications. In order to utilize these materials and their electrical characteristics, many fabrication methods are being used, such as chemical vapor deposition, physical vapor deposition and screen printing, to build thin or thick film multi-layer electronic devices. However, those existing methods require high temperature or numerous sintering processes following the deposition which restrict substrate and material selection due to chemical/mechanical stability requirements among the multi-layers. Also, in some conditions, they need a sizable vacuum chamber for a large scale deposition in order to commercialize the devices, and even then the cost of manufacturing is still expensive.

Thermal spray is a directed melt-spray-deposition process in which powdered feedstock is injected into a high temperature thermal plasma/flame and propelled towards a prepared substrate with high velocity. The coating is built up by successive impingement and rapid

solidification of the impacting droplets. The process allows significant material versatility and application flexibility with inherent scalability, with near ambient substrate temperatures. However, upon rapid quenching, the particles contain structural disorder and produce architectural defects such as pores, cracks, and interfaces within the coating. Compositional changes of the particles via decomposition or preferential species volatilization from the thermal and chemical gradient interactions experienced are also included in the deposit. These factors, together with process-induced residual stresses can affect electrical properties and functional performance, and have limited the application area only to the protective coatings such as thermal barrier, wear and corrosion resistance coatings.

The goal of this dissertation is to elucidate the new opportunities for thermal spray as a fabrication method for functional oxide coatings by deliberately controlling the process parameters in order to achieve the required functionalities. The aims of this thesis are to provide a scientific understanding of thermal spray parametric effects, using the plasma/flame as an energetic reactive source that affects stoichiometry of the functional oxide materials and trapped states due to rapid solidification. These depositional parameters affect the electrical/magnetic and protective functional performances which are evaluated by examination of the process-microstructure-phase-functional properties relations for solid oxide fuel cells and thermoelectric applications.

Dedication

Dedicated

To

my Mother and Father

and

my Husband, Dr. Seongchan Pack

and

my lovely Son, Stewart

-감사하고 사랑합니다-

Table of Contents

9. References

List of schemes/figures

List of tables

Acknowledgments

I would like to gratefully take this opportunity to express my sincere appreciations to my adviser Prof. Sanjay Sampath for not only his guidance of all about thermal spray process but also his generous understanding about my dual positions; PhD student mom. Without his countless supports, I could not complete this academic journey. Also, I would like to thank my co-adviser Late Prof. Richard J. Gambino for his guidance of electrical/magnetic analysis. Also, I would like to dedicate my last chapter (Chapter 8) of this dissertation to him.

I would like to thank my dissertation committee members, Prof. David O. Welch, Prof. Jason Trelewicz and Dr. Jeff Brogan for their precious comments, discussions and suggestions.

I would like to thank Dr. Brian W. Choi (who brought me to join this group), Dr. Gopal Dwivedi (who is always willing to become CTSR101 for me), Drs. Ramachandran C. S. and Yikai Chen (who prepared for all of my plasma sprayed specimens), Dr. Atin Sharma (who came to Stony Brook to train me the instruments and measured inductive coupled plasma), Dr. Kentaro Shinoda (who reviewed my MCO paper and gave precious comments).

Also, I would like to thank my CTSR colleagues, Vaishak Viswanathan (thank my six and half year old friend, I'm going to miss you), Andrew Vackel (for your HVOF samples and many discussions), Hwasoo Lee (for joining this group^^), Gregory Smith (for the HV2000 samples), Ari Sagiv (for measuring SEM and image analysis), Mr. Glenn Bancke, Chris Jensen, Travis Wentz, Micheals (Flynn, Miller, Resnick), Ed , Amey, Albert, Nick, Gerard, Mr. Park, Dr. Ravi Dey (for all of copies of references), Dr. Katherine Flynn, Dr. Raja, Dr. Emma Li, Gordon, Jongkwon, Junghan, Sal, Matt, Sean, Julia.

I am so glad to work with Dr. James Quinn so that I can get awesome SEM/EDX images and I am grateful to Dr. Zdenek Pala (IPP) for your XRD and Rietveld analysis works. Also, thanks to Jiri to introduce me Zdenek.

I would like to thank Ms. Sarena Romano, Ms. Chandrani Roy, Ms. Shauntae Smith and Ms. Debby Michienzi for their administration helps.

I would like to express my appreciation to my friends, Drs. Bora Park, Jayon Lihm, Hyejin Ryu, Jusang Lee, and Kiwon Yun, Doohee Lee, Jae Wha Yang, Nahyun Cho, for sharing their precious time. They made my phd life more joyful and peaceful.

Lastly, I would like to express my endless love and appreciation to my parents, sister, husband (Dr. Seongchan Pack), son, and my parents and brother in-law for their encouragements and supports. In addition, thanks for their patience and endless love.

Vita, Publications and/or Fields of Study

Education

Ph.D. in Materials Science & Engineering, Stony Brook University, Stony Brook, NY. *08/2009-Present*
Ph.D. candidate in Electrochemistry, Ewha Womans University, Seoul, South Korea. *03/2007-07/2009*
M.S. in Electrochemistry, Ewha Womans University, Seoul, South Korea. *03/2005-02/2007*
B.S. in Chemistry and Physics, Ewha Womans University, Seoul, South Korea. *03/2001-02/2005*

Publications

1. **S. J. Han**, Z. Pala, S. Sampath, Plasma Sprayed Manganese-Cobalt Spinel Coatings: Process Sensitivity on Phase, Electrical and Protective Performance. *Journal of Power sources* **304** (2016) 234-243.
2. **S. J. Han**, Y. Chen, S. Sampath, Role of process conditions on the microstructure, stoichiometry and functional performance of atmospheric plasma sprayed La(Sr)MnO_3 coatings. *Journal of Power Sources* **259** (2014) 245-254.
3. I. K. Dimitrov, W. Si, W. Ku, **S. J. Han**, J. Jaroszynski, Unusual persistence of superconductivity against high magnetic fields in the strongly-correlated iron-chalcogenide film FeTe:O_x. *Low Temperature Physics* **39** (2013), 680-684.
4. Z. Stegen, **S. J. Han**, J. Wu, A. K. Pramanik, M. Hücker, G. Gu, Q. Li, J. H. Park, Evolution of superconducting correlations within magnetic-field-decoupled $La_{2-x}Ba_x$ CuO_4 (x= 0.095). *Physical Review B* **87** (2013), 064509.
5. W. Si, **S. J. Han**, X. Shi, S. N. Ehrlich, J. Jaroszynski, A. Goyal, Q. Li, High current superconductivity in $FeSe_{0.5}Te_{0.5}$-coated conductors at 30 tesla. *Nature Communications* **4** (2013) 1347.
6. Y. Chen, **S. J. Han**, S. Sampath, Process-Property Correlations in Thermal Spray Functional Oxides. *Advanced Materials & Processes* **170** (2012), 49-50.
7. Q. Jie, **S. J. Han**, I. Dimitrov, J. M. Tranquada, Q. Li, Transport properties of stripe-ordered high T c cuprates. *Physica C: Superconductivity* **481** (2012) 46-54.
8. J. Y. Jung, **S. J. Han**, J. Chun, C. Lee, J. Yoon, New thiazolothiazole derivatives as fluorescent chemosensors for Cr^{3+} and Al^{3+}. *Dyes and Pigments* **94** (2012), 423-426.
9. J. Wen, Q. Jie, Q. Li, M. Hücker, M. Zimmermann, **S. J. Han**, Z. Xu, D. K. Singh, Uniaxial linear resistivity of superconducting $La_{1.905}Ba_{0.095}CuO_4$ induced by an external magnetic field. *Physical Review B* **85** (2012) 134513.
10. T. A. Tyson, T. Yu, **S. J. Han**, M. Croft, G. D. Gu, I. K. Dimitrov, Q. Li, Local structure of the superconductor $K_{0.8}Fe_{1.6+x}Se_2$: Evidence of large structural disorder. *Physical Review B* **85** (2012) 024504.
11. Y. Zhou, J. Jung, **S. J. Han**, Y. H. Jang, D. H. Kim, C. Lee, J. Yoon, Novel Bi-Nuclear Boron Complexes with Pyrene Ligand: Synthesis, Photoluminescence, and Electrochemistry Properties. *Notes* **32** (2011) 3097.

12. **S. J. Han**, H. J. Jung, J. H. Shim, H. C. Kim, S. J. Sung, B. Yoo, D. H. Lee, C. Lee, Y. Lee, Non-platinum oxygen reduction electrocatalysts based on carbon-supported metal–polythiophene composites. *Journal of Electroanalytical Chemistry* **655** (2011) 39-44.
13. Y. Zhou, J. W. Kim, M. J. Kim, W. J. Son, **S. J. Han**, H. N. Kim, S. Han, Y. Kim, C. Lee, Novel bi-nuclear boron complex with pyrene ligand: red-light emitting as well as electron transporting material in organic light-emitting diodes. *Organic letters* **12** (2010), 1272-1275.
14. Z. Xu, **S. J. Han**, C. Lee, J. Yoon, D. R. Spring, Development of off–on fluorescent probes for heavy and transition metal ions. *Chemical Communications* **46** (2010), 1679-1681.
15. H. J. Son, W. S. Han, **S. J. Han**, C. Lee, S. O. Kang, Electrochemically Active Dendrimers for the Manufacture of Multilayer Films: Electrochemical Deposition or Polymerization Process by End-Capped Triarylamine or Carbazole Dendrimer. *The Journal of Physical Chemistry C* **114** (2009) 1064-1072.
16. X. Qi, S. K. Kim, **S. J. Han**, L. Xu, A. Y. Jee, H. N. Kim, C. Lee, Y. Kim, M. Lee, Study on the BODIPY-triazine-based tripod fluorescent systems: various structures from similar procedure. *Supramolecular Chemistry* **21** (2009) 455-464.
17. J. D. Lee, T. J. Kim, W. S. Han, **S. J. Han**, C. Lee, J. Ko, S. O. Kang, C2-Symmetric Group 4 Metal Complexes Adorned with Chiral N, O Chelates: Synthesis and Structural Characterization of Helical Hexacoordinate Metal Dichlorides Derived from 6-Isopropyl-3-methyl-2-(4-isopropyl-4, 5-dihydrooxazol-2-yl) phenol Ligands. *Zeitschrift für anorganische und allgemeine Chemie* **635** (2009) 1435-1441.
18. Z. Xu, S. K. Kim, **S. J. Han**, C. Lee, G. Kociok-Kohn, T. D. James, J. Yoon, Ratiometric fluorescence sensing of fluoride ions by an asymmetric bidentate receptor containing a boronic acid and imidazolium group. *European Journal of Organic Chemistry* **(**2009) 3058-3065.
19. H. J. Son, W. S. Han, K. R. Wee, J. Y. Chun, K. B. Choi, **S. J. Han**, S. N. Kwon, J. Ko, Systematic Electronic Control in Ambipolar Compounds Optimizes Their Photoluminescence Properties: Synthesis, Characterization, and Device Fabrication of Four-Coordinate Boron Compounds Containing an N, O-Chelating Oxazolylphenolate Ligand. *European Journal of Inorganic Chemistry* **(**2009) 1503-1513.
20. Z. Xu, G. H. Kim, **S. J. Han**, M. J. Jou, C. Lee, I. Shin, J. Yoon, An NBD-based colorimetric and fluorescent chemosensor for Zn^{2+} and its use for detection of intracellular zinc ions. *Tetrahedron* **65** (2009) 2307-2312.
21. S. K. Kim, D. Seo, **S. J. Han**, G. Son, I. J. Lee, C. Lee, K. D. Lee, J. Yoon, A new imidazolium acridine derivative as fluorescent chemosensor for pyrophosphate and dihydrogen phosphate. Tetrahedron 64 (2008) 6402-6405.
22. H. J. Son, W. S. Han, J. Y. Chun, B. K. Kang, S. N. Kwon, J. Ko, **S. J. Han**, C. Lee, Generation of blue light-emitting zinc complexes by band-gap control of the oxazolylphenolate ligand system: syntheses, characterizations, and organic light emitting device applications of 4-coordinated Bis (2-oxazolylphenolate) Zinc (II) complexes. *Inorganic chemistry* **47** (2008) 5666-5676.
23. X. Qi, S. K. Kim, **S. J. Han**, L. Xu, A. Y. Jee, H. N. Kim, C. Lee, Y. Kim, M. Lee, S. J. Kim, New BODIPY–triazine based tripod fluorescent systems. *Tetrahedron Letters* **49** (2008) 261-264.

24. Z. Xu, S. Kim, H. N. Kim, **S. J. Han**, C. Lee, J. S. Kim, X. Qian, J. Yoon, A naphthalimide–calixarene as a two-faced and highly selective fluorescent chemosensor for Cu^{2+} or F^{-}. *Tetrahedron Letters* **48** (2007) 9151-9154.
25. K. M. K. Swamy, M. S. Park, **S. J. Han**, S. K. Kim, J. H. Kim, C. Lee, H. Bang, Y. Kim, New pyrrolopyridazine derivatives as blue organic luminophors. *Tetrahedron* **61** (2005) 10227-10234.

1. Introduction

Functional oxides are important classes of materials because of a tunability of their physical properties due to their structural characteristics: cations with mixed valence states, and anions with deficiencies [1]. By controlling either cations (dopants and ratio of doping) or anions (level of oxygen vacancies) or both, the electrical, optical, magnetic and chemical properties can be varied. The structural diversity of functional oxides induces new phenomena and applications such as dielectricity, semiconductivity, superconductivity, ferroelectricity, and magnetism for emerging technologies such as electronic components (complementary metal–oxide–semiconductor (CMOS)), sensors and energy harvesting/storage (solid oxide fuel cells (SOFCs), thermoelectrics, batteries) applications [2]. In addition, their thermal stability with a small range of thermal expansion as well as high toughness compared to those of metals has enabled a focus on these materials for high temperature applications with robust performance. The functional oxide materials are classified by their functional application area and summarized in Table 1.1.

Traditionally, functional oxide materials are widely used for dielectric application such as capacitors, resonators, antennas and metal-oxide-semiconductor field-effect transistors (MOSFETs) due to their stable and excellent electrical isolation properties. In order to enhance the performance (high dielectric constant, low dissipation factor, yet resistance to ionization) with reducing cost for commercialization, countless endeavors are being made in both research and industry sides by discovering new class of materials and processes as well as new designs of device architecture. For example, silicon dioxide (SiO_2) has been widely used as a gate oxide material in MOSFET due to its good electrical insulation and high chemical stability [3]. However, leakage currents comprised of tunneling, which deteriorates power consumption and device reliability, drastically increased as demanding of decrease in size of device as well as gate thickness accordingly in order to increase the gate capacitance and thereby easily drive current, raising device performance [4]. Thus, replacing the silicon dioxide gate dielectric with a high-κ material such as $HfSiO_4$, $ZrSiO_4$, HfO_2, and ZrO_2 depositing via atomic layer deposition (ALD) is considered to increase gate capacitance without the associated leakage [5-8].

The most notable part that made be paid attention to the functional oxides is semiconducting behaviors. Metal oxide semiconductors are crystalline or amorphous solids with size of band gap usually lesser than 3 eV that attribute temperature (T) dependent electrical characteristics, i.e. electrical conductivity increases as T increase. There are two types of semiconductors, p- and n-types classified by types of charge carriers, holes and electrons. The charge carrier concentration can be controlled by either cations (dopants and ratio of doping) or anions (level of oxygen vacancies), thus, the electrical conductivity of oxide materials could be manipulated. The potential bias is generated by making junction with different charge carrier (concentration) of semiconductors, this junction enables the metal oxide semiconductors as good candidates for diodes, transistors and all modern electronic and energy harvesting applications. For example, indium tin oxide (In_2O_3-SnO_2, ITO) is one of the widely utilized electrode materials for flat and flexible displays as well as solar cell applications due to its ability of transparency with thermal and chemical stability and suitability of highest occupied molecular orbital (HOMO) and lowest unoccupied molecular orbital (LUMO) energy levels to the other cell components for electrical transport [9-10]. LSM ($La_{1-x}Sr_xMnO_3, 0 \leq x \leq 0.5$) perovskite is a popular cathode material in SOFCs because it provides high electrical conductivity and good electrochemical performance with oxygen affinity [11-12]. In addition, thermoelectric property of oxide semiconducting materials plays an important role in sensor and thermoelectric generator/refrigerator applications. For instance, TiO_2 could be a good alternative oxygen sensing materials in catalytic convertor instead of expensive noble metals [13].

Oxide phosphors are often transition metal compounds that exhibit luminescence i.e. includes both phosphorescence (shows a slow decay in brightness (> 1 ms)) and fluorescence (the emission decay takes place over tens of nanoseconds). Phosphorescent materials are known for their use in radar screens and glow-in-the-dark toys, whereas fluorescent materials are common in cathode ray tube (CRT) and plasma video display screens, sensors, and scintillator in white light emitting diodes (LEDs). Inorganic phosphors emit light by luminescence through emission centers not by all atoms and these inhomogeneities in the crystal structure are created usually by addition of a trace amount of dopants (impurities) called activators. For example, cerium(III)-doped yttrium aluminum garnet (Ce-YAG, or Ce^{3+}-$Y_3Al_5O_{12}$) is often coated on blue light emitting material for generating white-LEDs by absorbs the light from the blue LED and emits in a broad spectra from green to red [14]. Another application of the oxide phosphors is phosphor thermometry in thermal barrier coating (TBC) in gas turbine engine (yttria-stabilized zirconia co-doped with europia (Eu-YSZ) [15] and YSZ co-doped with dysprosia (Dy-YSZ) by capturing temperature dependent decay [16].

Superconductors which carry electrical current without energy dissipation when they are cooled below critical temperature or superconducting transition temperature (T_c) are one of important roles of functional oxide materials. The superconducting state emerges at T_c from interactions of electrons that first form Cooper pairs. These Cooper pairs condense into the superconducting state, marked by macroscopic spatial coherence that results in the zero-resistance state. High-T_c superconductivity (HTS), which shows zero resistivity above liquid N_2 temperature, is discovered oxide system (Ba-La-Cu-O) in 1986 by Bednorz and Muller [17].

Since HTS materials have been discovered, scientists have been continuously trying to employ HTS oxide materials in the electricity transmission and utility industry due to their potential cost saving by using N_2. There are several criteria which the “ideal” superconductor for energy transportation and storage must meet such as the highest possible critical current density (J_c) and higher upper critical field (H_{c2}). Superconductor has the ability of attaining high magnetic field, important for superconducting motors, generators, and SMES (superconducting magnetic energy storage). The upper critical field (H_{c2}) is the highest field at which superconductivity is finally suppressed, and hence sets the limit for high field applications. The current-carrying capability, measured by J_c, is governed by vortex pinning strength, which depends fundamentally on the intrinsic anisotropy of the superconducting state, and is determined by the ability of defects in superconductors to pin the superconducting vortices carrying the magnetic flux [18]. In addition, the superconducting state is affected by mass anisotropy and critical current anisotropy, which would ideally be minimized. Superconductivity can be suppressed or maintained depending on the orientation of the crystallographic axis with respect to the applied magnetic field. Thus, developing higher T_c, J_c and H_{c2} materials while understanding the origins of their field anisotropic properties are important issues to be solved in order for develop superconductors for energy applications.

Ferrite are electrical insulating and magnetic moment containing transition metal oxides composed of iron oxide ($MO\text{-}Fe_2O_3$) combined chemically with one or more additional divalent metallic ions (M) such as Co^{2+}, Fe^{2+}, Mg^{2+}, Mn^{2+}, Ni^{2+}, Zn^{2+}[19-21]. Ferrites can be divided into two families based on the value of magnetic coercivity; value of applied external magnetic field to be demagnetized. Hard ferrites having high coercivity are usually composed of iron oxide and alkali earth metal ions such as $BaFe_{12}O_{19}$ and $SrFe_{12}O_{19}$. They are used to make magnets, for devices such as refrigerator magnets, loudspeakers and small electric motors. Soft ferrites having low coercivity are useful in the electronics industry to make ferrite cores for inductors and transformers, and in various microwave components.

Many fabrication methods such as atomic layer deposition (ALD), chemical vapor deposition (CVD), physical vapor deposition (PVD), dip coating, electrophoretic deposition, spark plasma sintering and screen printing are being developed to build thin or thick film multi-layer electronic devices with the functional oxide materials (see Scheme 1.1). CVD is one of the popular methods for depositing refractory functional oxide thin films by a chemical reaction at the vicinity of any given substrates using thermal activation [22]. Thin film transistors (TFTs) are three terminal field-effect devices, whose working principle relies on the modulation of the current flowing in a semiconductor placed between two electrodes (source and drain). A dielectric layer is inserted between the semiconductor and a transversal electrode (gate), being the current modulation achieved by the capacitive injection of carriers close to the dielectric/semiconductor interface [23-24]. Scheme 1.2 shows the most common TFT structures. This multicomponent-subsequent thin layered device structure is accomplished by usually state of the art CVD process but also the processes above. Despite their ability to be deposited from nanometer scale to traditional thick-film-based mesoscale 10 μm to millimeter dimension to facilitate new generation electronic devices, these existing methods require multiple steps during fabrication involving high temperature and associated numerous sintering processes, following right after the deposition. These treatments restrict substrate and material selection due to chemical/mechanical stability among the multi-layers. The comparison of the substrate temperature and applicable thickness of coating deposition techniques are presented in Scheme 1.3. In addition, fabrication-under-vacuum schemes in a large scale deposition are generally required to commercialize the devices, however this raises the cost of manufacturing significantly. Moreover, the relatively slow production rate of existing methods is a barrier for the commercialization of the devices to keep up with the excess energy demand. Thus, fabrication techniques that enable large scale manufacturing with material flexibility, efficient productivity and reasonable cost are in demand.

Thermal spray process is a surface coating deposit method by injecting desired feedstock materials (powder or wire) into a high thermal energy source such as electric arc (6,000 to 15,000 °C) or combusted flame (95 to 205 °C for wire flame, 2500 to 3100 °C for high-velocity oxy fuel) [25]. The molten/semi-molten particles are accelerated with high velocity (50 – 1000 m s^{-1}) and impacted on the substrate. The resultant deposit is built up by successive impingement of these rapidly quenched (10^6 K s^{-1}) droplets (splats) resulting in a thick film or coating (50 μm – several mm thickness scale) (see Scheme 1.4). Since Schoop firstly deposited metallic coatings by pouring molten metal into a gas stream in 1910, there has been successful progression for more than five decades for depositing metallic and ceramic coatings in wide ranging applications from aero- and land-based gas turbines, engineering machinery, biomedical implants and for reclamation. (See Scheme 1.5) The high throughput, material/substrate versatilities, low substrate temperature and scalability with respect to component size and number has allowed thermal spray to be a highly competitive and cost effective materials manufacturing technology [26-29]. However, upon rapid quenching, the particles contain structural disorder (metastable phases) and produce architectural defects such as pores, cracks, and interfaces within the coating (see Scheme 1.6). Compositional changes of the particles via decomposition or preferential species volatilization from the thermal and chemical gradient interactions experienced during flight are also included in the deposit. These factors, together with process-induced residual stresses can affect electrical properties and functional performance.

In recent years, the scientific methodologies have been established to extend the capabilities of thermal spray for functional systems [30-33]. The concept of process maps, stress and microstructure evolution dynamics, and property assessments developed for the zirconia-based thermal barrier coating systems can be readily extended to functional oxides i.e. La(Sr)MnO_3 (LSM). However, additional requirements of phase stability, chemical stoichiometry, and disorder should be considered during process parametric analysis to retain the material functionalities. Finding optimum performance is highly complex to interpret and map, but is needed to direct and accelerate materials and process development. For example, plasma sprayed MnZn ferrite coatings (MZF) with feedstock stoichiometry of $Mn_{0.52}Zn_{0.48}Fe_2O_4$ are extensively studied by Yan et al. in order to provide scientific understanding of the plasma spray process-structure-functional property relationships of ferrites [33-38]. First of all, the as-sprayed coating contains wustite (FeO) phase at the grain boundaries attributed to oxygen loss in the reductive environments in the plasma flame, but the resultant secondary phase is readily converted to hematite (Fe_2O_3) upon post annealing treatment (500 °C for 30 min in air). This indicates that the oxidation state of Fe changed during processing from Fe^{3+} to Fe^{2+}. Second, the stoichiometry of as-deposited coating shows deviations from that of the original feedstock due to the preferential Zn vaporization during plasma spraying which led to disorder in the structure. Thus, the compositional changes in as-sprayed coating affect degradation of saturated magnetization. Recently, systematic study in parametric effect on stoichiometry, microstructure, and magnetic properties of plasma sprayed MZF was conducted by Shinoda et al. [32].

In this dissertation, thermally sprayed functional oxide coatings were deposited by deliberate control the spray parametric variables to investigate the effect of thermal exposure on the feedstock functional oxide materials and their coatings. The main goal of this work is providing a scientific foundation for the functional oxide materials based on process-structure-properties relationship and demonstrating the feasibility of thermal spray process as alternative fabrication methods for the electronic industry. Specifically, this thesis investigated two test baths as the possible opportunities in power generation applications of thermal spray process; oxide scale protection layer for cathode in solid oxide fuel cells (SOFCs) and thermoelectric generators (TEGs). There are several key requirements that can be highlighted to make the thermal spray process functional for the electronic device applications. The processing must provide coatings with dense microstructure yet low residual stress, mechanical strength, minimum thermal expansion mismatch with the other components and minimal phase decomposition in order to get the desired properties with robust performance. For example, the protection layer for cathode protection in SOFCs requires prerequisites of high electrical conductivity (> 50 S cm^{-1}) at the cell operation temperature (600 – 800 °C) with providing oxide scale growth barrier (sluggish the oxide scale growth rate than the system without coating). Moreover, the thermoelectric coating system also requires low thermal conductivity, high Seebeck coefficient without any reduction of electrical conductivity.

1.1 Solid oxide fuel cells (SOFCs)

Solid oxide fuel cells (SOFCs) are ceramic fuel cells which generate electrical power with high efficiency by using natural gas which is reformed into hydrogen in situ as their fuel with air which provides oxygen for the electrochemical reaction [39]. SOFCs are multicomponent, multilayer systems comprising of a cathode, anode, electrolyte, and interconnect, with specific material and microstructure attributes to meet a system level function. The principle of conversion chemical into electrical energy is that hydrogen and carbon monoxide are oxidized with oxygen ions at the porous anode electrode to form water and carbon dioxide, respectively. Electrons are generated via the oxidation reactions, and transported to the porous cathode side through an external interconnect. At the cathode, oxygen from air is reduced to oxygen ion by electrochemical reaction with the resulting electron. This generated oxygen ions are transported to the anode through an electrolyte where having a dense microstructure for gas-tightness with high affinity of oxygen ion yet no electron transport to avoid electrical short. Scheme 1.7 shows the typical planar type SOFC structure with chemical reactions at the each component [40]. The most studied SOFC system is Ni-YSZ (Y_2O_3-ZrO_2) cermet anode, 8YSZ (8 mol% Y_2O_3-92 mol% ZrO_2) electrolyte, and LSM ($La_{1-x}Sr_xMnO_{3-\delta}$, typically, x =0.15 – 0.30) cathode for high temperature operation (750 – 1000 °C) due to their limited ionic/electrical transport and catalytic properties. Recently, doped ceria electrolytes ($Ce_{0.9}X_{0.1}O_{2-\delta}$, X = Gd or Sm) are utilized with LSCF ($La_{0.6}Sr_{0.4}Co_{0.2}Fe_{0.8}O_{3-\delta}$) cathode for the intermediate temperature operation (< 700 °C). Table 1.2 summaries the material requirements for each desired function of SOFC components [41].

Numerous techniques have been investigated to fabricate multilayers onto substrates i.e. electrode (anode/cathode)-supported or electrolyte-supported SOFCs such as pulsed laser deposition (PLD) [42], electrophoretic deposition (EPD) [43-44], high temperature sintering in reducing atmosphere [45-47], screen printing [48-50], slurry-spraying [51], electroplating [52], and vacuum [53-55] and air [56-58] plasma spraying, etc. Among them, plasma spray process is a promising method, offering scalability and cost effective manufacturing for SOFC applications.

Historically, thermal spray used SOFC was firstly attempted in 1967 by producing the electrodes-electrolyte assembly using plasma spray process and documented by a Swiss patent [59]. In 1990, Gruner and Tannenberger produced cathode supported entire fuel cell (A porous Ni-zirconia cermet served as anode, a 250 μm thick YSZ used as electrolyte, the porous cathode of $LaSrMnO_3$ also sprayed) by vacuum plasma spray process [60]. Then, their results were opened to the public in 1994 [61]. They obtained a maximum power density of 230 mW cm^{-2} at an operation temperature of 910 °C with applying humidified H_2 as fuel. As soon as the opening, numerous research regarding each component of SOFC has been attempted to develop industrialize level of cells via thermal spray processes in terms of materials and optimization of spray conditions because of the versatility of plasma spray with respect to microstructural control that could be utilized in the SOFC industry to fabricate a range of materials and products: porous cathodes, porous dual phase (metal, oxide) anodes, dense electrolytes and oxide protection layers (the focus of this dissertation). Scheme 1.8 shows a SEM image of a single SOFC cell built by the plasma spray process [62]. Ma *et. al.* successfully fabricated fully integrated cells using air plasma spray (APS). They employed strontium and magnesium doped $LaGaO_3$ (LSGM), which has a lower melting point than yttria stabilized zirconia (YSZ), as electrolyte in order to overcome structural porosity and obtained cell power density as 80–150 mW cm^{-2} [63-64]. In addition, nanostructured YSZ/Ni cermet anode, LSGM electrolyte with ~60 μm in thickness and LSCF cathode with ~30 μm in thickness and ~30 % porosity SOFC cell is accomplished by

APS process. The output power densities of ~440 mW cm^{-2} at 800 °C, ~275 mW cm^{-2} at 750 °C and ~170 mW cm^{-2} at 700 °C are obtained by the novel nanostructure which is advantageous to enhance the area of triple phase boundaries [65].

A lot of the research carried out on electrolytes of SOFCs in order to improve its ionic conductivity and to lower operating temperatures without reducing oxygen ionic conductivity. Many electrolyte material candidates were considered in terms of reducing the resistivity to oxygen ion diffusion instead of yttria stabilized zirconia (YSZ), such as scandium doped zirconia (ScSZ), gadolinia-doped ceria (CGO), lanthanum gallate based perovskites (e.g., LSGM), apatite-type lanthanum silicate ($La_{10}(SiO_4)_6O_3$) [66-67]. Also, a lot of efforts have been made to understand spray parametric effect in terms of plasma gases, spray techniques (APS, low pressure plasma spray (LPPS), suspension plasma or HVOF spray (SPS)), size and types (fused and crushed, agglomerated and sintered) of feedstock YSZ in order to determine the influence of gas-tightness, microstructure, deposition efficiency and electrochemical performance as well of thinner YSZ electrolyte layers [68-73].

However, the particle based assemblage and high quench rates result in coatings with numerous process induced defects, including microcracks, pores, and interfaces. In addition, the large thermal gradients, high reactivity of the plume environment and rapid solidification result in non-equilibrium states, affecting microstructure, chemical composition, grain size and residual stress as well as electrical properties and functional performances [74-76]. In recognition of the above imperfections, this study investigates the relationships among process parameters, coating microstructure, electrical properties and Cr-poisoning protection performances of atmospheric plasma sprayed LSM and $Mn_{3-x}Co_xO_4$ (MCO) coatings. Both LSM and MCO coatings were synthesized through controlled processing conditions resulting in significantly different thermal exposures developed through a particle thermal energy-kinetic energy process map. The resultant coatings were not only characterized for phase, microstructure and stoichiometry, but also for functional attributes via temperature dependent DC electrical conductivity and magnetic properties. Thermal analysis was conducted to quantify the extent of manganese and oxygen recovery in the LSM and MCO coatings following process induced degradation. Lastly, the protective capability of the coating to prevent Cr-oxidation was assessed through analysis of oxide scales attributes underneath the various processed LSM and MCO coatings on ferritic steels. Such an integrated analysis of process-structure-properties and performance provides a framework for not only process design of optimal coatings but also identifying fundamental mechanisms involved in this class of defected functional systems.

1.2 Thermoelectrics

A thermoelectric generator (TEG) is one of the promising solutions for using wasting heat, which directly produces electricity through a thermal gradient along the TE materials. A TEG consists of many p-type and n-type junction pairs that are electrically in series and thermally in parallel that multiplies power generation. A schematic illustration of the power generation mechanism of a TEG is shown in Scheme 1.9. The ability for power generation with the TE materials can be characterized by the dimensionless figure of merit (*ZT*), defined as

$$ZT = \frac{S^2 \times \sigma}{(k_l + k_e)} \times T \quad \text{— (1.2.1)}$$

where S is the Seebeck coefficient, σ is the electrical conductivity, T is the absolute temperature, and k_l and k_e are the lattice and electrons thermal conductivities, respectively. For bulk materials, k_l and k_e are defined as

$$k_l = \frac{1}{3} v_s C_v L_{ph} \quad \text{— (1.2.2)}$$

$$k_e = \frac{1}{3} c_v v \Lambda = L \sigma T \quad \text{— (1.2.3)}$$

by Wiedemann-Franz-Lorenz's law [77], where v_s is the velocity of sound, C_v is the constant volume heat capacity, L_{ph} is the phonon mean free path, c_v is the electronic specific heat per volume, v is the electron velocity, Λ is the electron mean free path, and L is the Lorenz number, respectively [78]. Scheme 1.10 shows the interdependent relationship of thermoelectric terms, S, σ and k as a function of carrier concentration (n); electrical conductivity increases with increasing carrier concentration as well as thermal conductivity due to the proportionality of σ and k_e, while Seebeck coefficient decreases because the electrical potential cannot be maintained within the high electrical transport materials. As a result of optimization of the interdependent terms, the maximum *ZT* can be obtained from the range of carrier concentration $10^{19} < n < 10^{20}$, where indicates heavily doped semiconductors as good TE materials. Despite numerous efforts made to increase the value of *ZT* to above 1 for being practically useful, no significant enhancement of *ZT* has been reported in literature after the $(Bi, Sb)_2(Te, Se)_3$-based alloys were found as TE materials due to the complex interdependence of S, σ and k_e [79].

In order to overcome the interdependence, many strategies have been tried to control the thermoelectric variables beyond the optimization of carrier concentrations. Since k_l is the only independent term, many studies started from suppression of the phonon contribution, k_l, without the deterioration of optimized electronic transport through disorder within unit cell such as interstitials, partial occupancies, or rattling atoms (see Scheme 1.11) [80-82]. Likewise, filling the voids with rare-earth or heavy atoms such as La or Ce can reduce k_l by a rattling effect that scatters a larger spectrum of phonons in skutterudites and clathrates. Recently, introducing complex structure including two physical properties nanosheets fascinates researchers to design electronic-crystal phonon-glass structure such as cobaltite oxides ($(Na, Ca)_xCoO_2$)[83-85] and the molecular design and examples are shown in Scheme 1.12. In addition, it is proved from theoretical and experimental results that low dimensional systems [86-91] provide independent control of the thermoelectric terms by manipulating density of electronic states (see Scheme 1.13) [88]. For example, a thin-film superlattice structure based on the Bi_2Te_3 system offered an enhanced *ZT* up to ~2.4 at 300 K by significantly increasing carrier mobility and reducing k_l [86]. However, it is challenging to build such a good device due to the requirement of improving the electrical and thermal contacts of these tiny materials. Kanatzidis *et al.* have demonstrated that nanostructured bulk materials lowered the thermal conductivity by directly comparing the solid solution form and the nanostructured form of PbTe-10%PbS [92-93]. Bulk nano-grain materials synthesized by existing fabrication methods can generate polycrystalline materials containing randomly oriented grain boundaries that may lead to phonon-boundary scattering which reduces k_l, whereas the reduction of electron transport concurrently occurs via electron scattering at the interfaces [94-98].

Since Birkholz *et al.* first applied $FeSi_2$-based TEG to vehicle exhaust systems in 1988 [99], intensive efforts have been made to commercialize TEG as a self-powered boiler and switching alternator, enabled by waste heat recovery from heater/furnace and engine exhaust/catalytic converter in vehicles, respectively. After that, Bi_2Te_3-based materials used as TEG modules have been commercially available. However, Bi_2Te_3-based materials still are limited to use at temperatures as high as 250 ^oC due both to the lack of chemical stability at high temperatures in air and the toxicity. Also, the cost of TEG modules is still expensive owing to the cost of the materials required as well as the cost of manufacturing. Thus, the thermal spray process is considered an alternative method of producing TEG materials, to provide cost-effective and scalable/additive processing flexibility compared to existing fabrication methods such as melt-spinning, hot press and spark plasma sintering. Sampath *et al.* have demonstrated the capability of thermal spray (TS) coatings for electronic applications such as dielectrics, sensors, solid oxide fuel cells (SOFCs) and thermoelectrics [100-105]. Due to the process-induced imperfections such as pores, voids, microcracks, nanograins and metastability, a significant reduction of thermal conduction can be obtained in the TS coatings compared to that in bulk materials. This process induced thermal property enables the TS technique to be a most competitive thermal-barrier-coating (TBC) fabrication method in gas turbine industries [106]. Recently, Fu *et al.* produced sprayed Mg_2Si coatings in air and vacuum plasma which yielded *ZT* values of 0.002 at 390 K and 0.16 at 700 K, respectively [107-108]. Muthiah *et al.*

also reported a *ZT* value of 0.56 at 873 K for 2 at% Pb doped Mg_2Si because of the enormous enhancement of electrical conductivity, about three orders of magnitude, with only a nominal decrease in thermal conductivity [109]. HR-TEM revealed that there were Pb-rich grain boundaries which could provide carrier transport paths, like a brick-layer model. Similarly, Sharma *et al.* found an ease of the in-plane electrical transport in plasma sprayed TiO_2 coatings due to the generation of oxygen vacancy carriers at the splat boundaries [110]. Therefore, thermal spray process can be a promising candidate for the fabrication of bulk nanostructured TEG materials containing randomly oriented nano polycrystalline grains with conducting splat boundaries, which are formed by the rapid solidification nature (~10^6 K s^{-1}), even though it causes electrons scattering at the interfaces that concurrently reduces both the electrical and thermal conductivities [111].

For the last two decades, many researchers shed light on metal-oxide semiconductors as good candidates for high temperature TEG due to their nontoxicity, thermal/chemical stability and Earth-abundance [79,112-115]. In particular, studies of the thermal and electrical properties of titanium oxides have gradually increased since Andersson reported the existence of the Magnéli phases in 1957 (see the phase diagram of Ti-O system in Scheme 1.14), which was understood in scattering process and electrical conduction mechanisms via point defects in Rutile and reduced titanium oxides [116-120]. Since Okinaka and Akiyama recently published a brief report of $TiO_{1.1}$ attaining *ZT* of 1.64 at 800 °C, the study of the non-stoichiometric titanium oxides as promising thermoelectric materials has accelerated [121]. Later, Lu *et al.* reported a power factor up to 1 μW cm^{-1} K^{-2} at 1373 K for reduced TiO_{2-x} using carbon powders [122]. Harada *et al.* also prepared the Magnéli phase TiO_{2-x} (x=0.05, 0.10, 0.15, and 0.20) by hot-pressing to vary oxygen deficiency and then reported their electrical conduction as well as the carrier concentration, which increased with increasing oxygen deficiency while lattice thermal conductivity decreased [123]. They obtained *ZT* of 0.12 at 773 K for $TiO_{1.90}$. More recently, an enhanced *ZT* up to 0.35 at 700 °C was obtained by co-doping N- and Nb- in Rutile that induced a locally distorted TiO_{2-x} and enhanced the asymmetrical carrier transport [124]. Nevertheless, limited scientific research has been reported about thermal spray processing for practical TEG applications using there promising non-stoichiometric TiO_{2-x} materials that satisfy all of the requirements such as cost, Earth-abundance and environmental symbioses.

In this work, the thermoelectric properties of thermally sprayed TiO_{2-x} coatings were investigated with respect to the process-induced stoichiometric and crystallographic structure changes. The microstructures of TiO_{2-x} splats as well as coatings were carefully studied using SEM/EDX to discover a relationship between defect structures and electrical/thermal conductivities. The aim of this work is to provide a scientific understanding of the parametric effects of the thermal spray process to use the plasma/flame as an energetic reactive source that affects stoichiometry of the TiO_{2-x} and followed by rapid solidification to trap the states. In addition, the aim is to understand how the process affects the thermoelectric and electrical properties. Moreover, this work introduces the TS technique as a possible cost-effective synthesis method for thermoelectric devices using the non-stoichiometric TiO_{2-x} without post-reduction processes.

2. Statement of Problem

In order to cope with the depletion of fossil fuels, there are significant worldwide efforts at developing efficient power generation. Currently, international oil prices are soaring above $ 50 a barrel and now more than ever there is a need for alternative energy sources and advanced energy materials. Despite the rapid commercialization of alternative energy sources, such as fuel cells, solar cells, electricity from wind, and geothermal sources, conventional energy sources cannot be fully replaced due to the cost of the materials and processing. Thus, earth-abundant and environmental friendly materials with highly efficient processing methods are currently being sought.

Thermal spray is a directed melt-spray-deposition process in which powdered feedstock is injected into high temperature thermal plasma and propelled towards a prepared substrate with high velocity. The coating is built up by successive impingement and rapid solidification of the impacting droplets (splats). The process allows significant material versatility and application flexibility as wide ranging alloys and oxides can be deposited on to numerous substrate and component types. The inherent scalability of the process, along with the ability to apply coatings at near ambient substrate temperatures, has allowed thermal spray to be a highly competitive and cost effective materials manufacturing technology. Despite the many benefits of the thermal spray processes, perfection of the sprayed coatings, particular for electronic industries, remains challenging because the feedstock particles are exposed to high temperature with large gradients which cause preferential elemental vaporization. Also, particles are exposed to hydrogen content in the plasma/flame that attributed to loss of oxygen. Moreover, the interaction between the particles and flame/plasma is sensitively affected by location in the plume as well as size of the particles because of the difference of thermal and kinetic energy transfer which directly influences to the particle melting status; fully-, semi- and un-molten. In addition, particles could be re-oxidized from the surface regime during the flight depending on spray distance. Upon rapid quenching at the substrate, ~10^6 K s^{-1}, meta-stable phase or distorted lattice could be trapped in the crystallographic structure. Also, the single splat contains microstructural defects such as microcracks, droplet splashing with un-moltens due to complex effects of the above process induced factors which cause architectural defects, voids, globular and interlamellar pores, and microcracks in the coating upon successive impingements. These crystallographic and architectural defects crucially influence interparticle contact, porosity, adhesion/cohesion, stresses, delamination, compliance, macrocracks, electrical contacts which end up affect phase, microstructure, and electrical conductivity. (see Scheme 2.1) Hence, understanding the process-property-performance interplay for thermal sprayed functional oxide coatings is an important endeavor towards development of reliable electronic devices.

Despite an interesting scientific challenge, there are only limited scientific research approaches via thermal spray processes that have been reported for functional oxide materials compared to TBCs and tribological applications. This dissertation focuses on elucidating the relationships among thermal spray process-structure-properties of functional oxide materials for SOFCs and thermoelectric applications as parts of case studies to demonstrate the applicability of the thermal spray process. In order to provide scientific understand as well as find the optimized condition for the desired properties, functional oxide coatings were synthesized by thermal spray processes through controlled processing conditions resulting in significantly different thermal exposures developed through a particle thermal energy–kinetic energy process map. Such excursions allowed assessment of thermal decomposition, structural changes and coating density effects. Particle characteristics were measured through in-flight temperature and velocity measurements and mapped to visualize the resultant effects and process correlations. The resultant coatings were characterized for phase content, microstructure and stoichiometry. In addition, thermal analysis measurements were used to understand the thermo-physical and thermo-chemical changes. For SOFC protection layer application, the electrical and magnetic properties of the coatings were measured through four-point probe techniques over a range of temperatures, while vibrating sample magnetometer was used to assess the change in magnetic characteristics of the sprayed materials for various process conditions. Lastly, the protective capability of the coating to prevent Cr-oxidation was assessed through analysis of oxide scales attributes underneath the various processed LSM or MCO coatings on ferritic steels. For thermoelectric application, substoichiometric TiO_{2-x} was chosen as an n-type TE material due to its low cost and ease of availability. Thermoelectric variables, Seebeck coefficient and electrical/thermal conductivities, of TiO_{2-x} coatings were assessed to understand the dependence upon phase contents and microstructure of the coatings was assessed. The variables were investigated as a function of temperature and process conditions to find the optimized condition for future device application.

3. Experimental Methods

3.1 Coating Deposition

3.1.1 Powder Feedstock Matierials

The feedstock materials used in all coatings were YSZ (9024, -75+10 µm, Saint-Gobain Coating Solutions Thermal Spray Powders, Northampton, MA, USA), LSM ($(La_{0.8}Sr_{0.2})_{0.99}MnO_3$, Metco 6801, -53+20 µm, Sulzer Metco, Westbury, NY, USA) and MCO ($Mn_{1.5}Co_{1.5}O_4$, Metco 6820, -45+15 µm, Oerlikon Metco, Westbury, NY, USA) for SOFC Cr-poisoning protection coatings. Two different stoichiometric feedstock powders were chosen for thermoelectrics; $TiO_{1.9}$ (Metco 102, -45+11 µm, fused and crushed, Oerlikon Metco, Westbury, NY, USA) and $TiO_{1.7}$ (Metco 6231A, -105+32 µm, agglomerated and sintered, Oerlikon Metco, Westbury, NY, USA). Stoichiometry was selected based on the commercial availability of sprayable sized powders. The size of the feedstock particles were measured by laser diffraction particle size analyzer (LS™ 13 320, Beckman Coulter) and the distribution results are provided with their electron micrographs in Figure 3.1 – 3.4.

3.1.2 Coating Preparation and Particles Temperature and Velocity Diagnostics

LSM and MCO coatings were produced by air plasma spray (APS) with five different spray conditions (A-E), which were obtained through strategic variations to plasma H_2 content, overall gas mass flow rate, applied power and spray hardware configurations. The coatings were prepared with thickness of ~ 50 µm for LSM and ~ 70 µm for MCO on 18 % chromium (Cr) containing ferritic steel (FS) substrate (1`` diameter, 0.133`` thickness, ATI441HP^{TM}) for oxide scale growth test. Electrical conductivity samples were deposited through a bar-shaped mask (0.196`` W × 1`` L) on yttria stabilized zirconia (YSZ) coated 316 Stainless steel (SS) in order to confine coating geometry of the conductive coating deposit within the surface area of the insulating YSZ layer. In order to measure the intrinsic electrical conductivity of the coatings, a thickness of 200 µm scales was chosen as it minimizes any post deposition surface preparation for direct property measurement. It has been shown in past study the electrical property of thermal spray metals is not sensitive to the coating thickness [125]. A statistical design-of-experiment methodology was utilized to vary process conditions to achieve a range of thermal and kinetic energies exposure and the details of the processing parameters are shown in Table 3.1. Coatings A through C (Table 3.1) were prepared using F4MB-XL plasma torch (Sulzer Metco Inc., NY, USA) with a 8 mm nozzle diameter while varying gas ratios and torch current. Coating D was also produced using an F4MB-XL torch but with a 6 mm effluent nozzle to achieve higher particle velocities. Coating E was deposited using a Praxair TAFA SG100 plasma torch (Praxair surface technologies, Indianapolis, IN, USA) with a 4.5 mm nozzle and internal particle injection to produce coatings at high velocities with minimal thermal exposure. Helium was used as the secondary gas for this SG100 torch. All the coatings were prepared on preheated substrates with raster speed and stand-off distance of the plasma torch set to 500 mm s^{-1} and 100 mm, respectively. The conditions used here resulted in lower thermal energy input to particle along with higher particle velocities. In-flight particle temperature and velocity of each condition was monitored by particle diagnostic sensors DPV2000 and AccuraSpray-G3 (both from Tecnar Automation Lté., St. Bruno, QC, Canada). The particle temperature distributions of all of conditions obtained from the DPV2000 sensor show higher range than melting temperature of

LSM (1800 ^{o}C) and MCO (1650–1700 ^{o}C), indicating the a majority of the particles underwent melting during the spray process.

Substoichiometric TiO_{2-x} coatings were produced by the thermal spray process with varying torch hardware (F4MB-XL and SinplexPro^{TM}, both from Oerlikon Metco, Westbury, NY, and HV2000, Praxair Inc., Indianapolis, IN) and hydrogen gas ratio (none, low, med, and high for plasma spray process) in order to investigate process parametric effects on stoichiometry and electrical power generation performance. The coatings for Seebeck and electrical conductivity measurements were deposited on YSZ coated stainless steel substrate through bar-shaped masks (0.1094" W × 5.5" L and 0.196`` W × 1`` L, respectively) to confine coating geometry of the conductive deposit within insulating layer. Thermal conductivity samples were deposited at the same time on 1 cm dia. graphite rod. Coating thickness was ~250 µm for Seebeck and electrical conductivity measurements, with a range of 0.39-1.06 mm for thermal conductivity measurement. All the coatings were prepared on preheated substrates with raster speed and stand-of distance of the plasma torch set to 1000 mm s^{-1} and 100 mm (F4MB-XL and SinplexPro guns) and 1000 mm s^{-1} and 6 inches (HV2000), respectively. Splats of each condition were produced on polished stainless steel surface (1'' W × 2'' L) by passing one stroke with lowered powder feed rate to 4-6 g/min. Thermal and kinetic energies of feedstock particles were varied by controlling spray parameters that are shown in Table 3.2. In-flight particles' temperature and velocity were monitored by using particle diagnostic sensor AccuraSpray-G3 (Tecnar Automation Lte., St. Bruno, QC, Canada) and the results were plotted in 2-dimensional *T-v* space which is represented in first order process map.

3.2 Microstructure-SEM/EDX

As a first step, single impacted droplets (splats) were deposited on polished aluminum or stainless steel (SS) substrates to examine the characteristics of the individual building block of the microstructure. They were examined using scanning electron microscopy (SEM) (LEO 1550). Subsequently, coatings were deposited onto grit blasted SS substrates and the as-sprayed coatings on stainless steel were cross-sectioned, mounted in epoxy molds and then polished to examine microstructure and element ratio of coatings by scanning electron microscopy with energy dispersive X-ray spectroscopy (SEM/EDX) (LEO 1550-EDAX Detector). Also, image analysis was attempted with low magnification SEM images (x500) from 10 different locations of each coating by threshold binary images applying Otsu (only for MCO) or Triangle (only for TiO_{2-x}) formula in ImageJ 1.48v software (National Institutes of Health, USA) to calculate porosity of coatings.

3.3 Phase Structure and Stoichiometry Studies

The phase structure and stoichiometry of LSM feedstock powder and as-sprayed A through E coatings were investigated by powder x-ray diffractometer (XRD) (Phillips, 40 kV and 30 mA, Cu$K\alpha$ source) and inductive coupled plasma-optical emission spectroscopy (ICP-OES, Optima 7300DV, PerkinElmer, Inc. Waltham, MA, USA), respectively. Free-standing LSM coatings were first prepared by polishing off substrate and then finely pulverized in order to obtain a better resolution for XRD peaks and evenly dissolve into a concentrated aqua-regia acid solution for ICP-OES. Ambient XRD measurements of as-sprayed and annealed MCO coatings (at 700 °C for 2 h) were conducted using a Phillips x-ray diffractometer (Cu$K\alpha$ radiation, 40 kV and 30 mA). Temperature dependent phase composition of MCO coatings and ambient XRD measurement of TiO_{2-x} were investigated by D8 Discover powder diffractometer equipped with 1D detector (Bruker AXS, 40 kV and 30 mA, Co$K\alpha$ source) and heat chamber (MRI, Germany) with Platinum heating filament. Phase identification was attempted with X'Pert HighScorePlus software and Rietveld analysis in TOPAS 4.2; PDF-2 and ICSD databases were used.

3.4 TGA/DSC/Dilatometry

Thermogravimetric analysis (TGA) and differential scanning calorimetry (DSC) (STA 449C Jupiter, NETZSCH, LLC, Burlington, MA, USA) were used to measure thermal history of the coatings. Feedstock powder sample of 20 – 30 mg or free-standing as-sprayed coating in a Pt crucible set was heated up to 800 ^{o}C from room temperature in air with 10 ml min^{-1} Ar protective gas flow. Each specimen from two batches was measured 3 times each to obtain reliability of the test results. Dilatometry was also employed to get the temperature dependent coefficient of thermal expansion (CTE) of the coatings (DIL402C, NETZSCH, LLC, Burlington, MA, USA). Freestanding samples were carefully prepared for CTE measurement with size of sample length about 1`` and thickness about 1 mm. CTE has been measured with two thermal cycles from two different sample batches by applying 15 cN of push load, and the results are averaged and plotted.

3.5 Temperature Dependent Four-Point Probe Electrical Conductivity Measurement

Four-point probe electrical conductivity of the geometry confined as-sprayed coatings was measured from room temperature to 800 ^{o}C (for LSM and MCO) or 500 ^{o}C (for TiO_{2-x}). The bar-shaped coating was perpendicularly placed on one side of the alumina silicate bar (1.5"W x 9.5"L x 0.125"H) and four Pt wires (0.020`` diameter) were contacted with high performance Ag pastes (Ted Pella, Inc. Redding, CA, USA). Four probe contacts were carefully prepared to ensure ohmic contacts were established. (Measurements at multiple span lengths were used to ensure no contact resistance was present). The tip of k-type thermocouples was contacted on the coatings surface with silicon-based zinc oxide pastes to measure accurate sample temperatures. The schematic configuration of the prepared sample is shown in Figure 3.5. The prepared sample on the alumina silicate bar was inserted into the center of a tube furnace to control sample temperatures. The four-probe Pt wires and thermocouples were directly connected to 7700 module of Keithley 2700 digital multimeter. Samples were thermally cycled from room temperature to 800 ^{o}C then isothermally held for 24 hours and cooled down to room T while measuring electrical resistance.

3.6 Vibrating Sample Magnetometer (VSM)

Magnetic hysteresis loops of feedstock powders, as-sprayed and annealed coatings of LSM and MCO were obtained using vibrating sample magnetometer (VSM) (Model 880, Digital Measurement Systems, Microsense, LLC. Lowell, MA, USA). The as-sprayed coatings were annealed at 600 ^{o}C (LSM) or 700 ^{o}C (MCO) for 2 hours in the tube furnace in order to maximize the oxygen recovery process based on the results from the TGA/DSC measurements. Free-standing specimens for VSM were prepared by polishing and mounted on high purity quartz rods using Teflon tape. Saturated magnetization (M_s) values of each coating were calculated by an extrapolation method due to the lack of a saturation plateau.

3.7 Oxidation Tests

18% Cr-containing ferritic steel substrates (ATI 441HP^{TM}) with 50 – 70 μm thick LSM and MCO coatings or without coating were heat treated at 800 ^{o}C for 600 hours in tube furnace to compare oxide-scale growth rate. The annealed coatings and ferritic steel substrate were mounted in an epoxy mold and polished for cross-sections. The cross-sectional microstructure and elemental profile across the oxide scale of each coatings and ferritic steel substrate were investigated by SEM-EDX (LEO 1550-EDAX detector).

3.8 Seebeck Measurement

Electrical voltage was generated by creating a temperature gradient through the TiO_{2-x} coatings by heating one end on the back side with a hand torch and cooling the front side of the other end with a voltex cold air gun (itwvortec.com, Cincinnati, OH, USA). K-type thermocouples were directly attached on each end of the coating surfaces to measure hot and cold-sides temperature. Seebeck voltages of the geometry confined TiO_{2-x} coatings were measured using Keithley 2700 digital multimeter.

3.9 Thermal Conductivity Measurement

Temperature dependent thermal conductivity was performed for TiO2-x coatings at 300, 350, 450, 550, 650 and 750 K by laser flashing method (FLASHLINE^{TM} SYSTEM X-PLATFORM^{TM}, anter corporation, Pittsburgh, PA, USA).

4. Role of Process Conditions on the Microstructure, Stoichiometry and Functional Performance of Atmospheric Plasma Sprayed La(Sr)MnO$_3$ Coatings

Typically, SOFCs operate in the temperature range of 600 ^{o}C to 1000 ^{o}C depending on the material configurations. Cells operating at the higher end of the temperature spectrum typically use ceramic based electrical interconnects. A key benefit of intermediate temperature-solid oxide fuel cells (IT-SOFCs) that operate in the temperature range of 600 – 800 ^{o}C is the ability to replace ceramic interconnects with less expensive metallic alloys [126] that provide chemical/thermal stability, enhancing electrical/thermal conductivity of cells, and lowering manufacturing/operation costs. Typically, ferritic or stainless steels are used as the interconnect layer but these chromia containing systems can form oxide deposits at triple phase boundaries and degrade cell performance by impeding catalytic and transport activities [127-129]. The degradation mechanism of the air electrode is known as two steps;

$$Cr_2O_3\ (s) + (3/2)O_2\ (g) + 2H_2O\ (g) \rightarrow 2CrO_2(OH)_2\ (g) \quad \text{— (4.1)}$$

$$2CrO_2(OH)_2\ (g) + 6e^{-} \rightarrow Cr_2O_3\ (s) + 2H_2O\ (g) + 3O^{2-} \quad \text{— (4.2)}$$

Due to vaporization of the intermediate species, $CrO_2(OH)_2$, it is difficult to control the formation of chromium oxide scale at the cell operation temperature. Figure 4.1 shows the schematic illustration of cell degradation mechanism and SEM images that display before and after the Chromia poisoning at the interface of LSM cathode and YSZ interconnect.

Many research groups have developed special steel for intermediate temperature interconnect such as E-brite, Crofer 22 APU, ZMG232, and 430 in order to improve oxidation resistance [130-131]. The chemical composition and coefficient of thermal expansion of the alloys are displayed in Table 4.1. Also, by adding reactive elements such as La, Y, Ce, Hf, Zr, Ti etc. to the special ferritic steel, newly modified alloys show a highly oxidation resistance with greater creep strength [132]. Despite the developments and modifications of special alloys, protection layer for blocking chromia scales is still required for SOFC operation [133]. Gindorf *et al.* coated the alloy surface with doped-$LaCrO_3$ to avoid the volatile species producing reaction (4.1) [134]. Taniguchi *et al.* introduced a La_2O_3 containing second layer into the cathode to trap the $CrO_2(OH)_2$ vapor [135]. Matsuzaki *et al.* demonstrated the suppression of electrochemical reduction reaction (4.2) of the volatile Cr-species by changing chemical compositions of electrode and electrolyte with $La_{0.6}Sr_{0,4}Co_{0.2}Fe_{0.8}O_3$ and $Ce_{0.8}Sm_{0.2}O_{1.9}$, respectively [128]. Nie *et al.* deposited LSM and Ni directly on both Cr-containing metallic interconnects of cathode and anode sides, respectively, by plasma spray method to protect against Cr-poisoning [136]. Thus, protective oxide coatings that are simultaneously electrically conductive are sought to address this degradation issue with the most commonly used coating material being $La(Sr)MnO_3$ (LSM) perovskites [137-141].

Lanthanum manganite ($LaMnO_3$) perovskite ceramic has been widely utilized as a functional oxide material because of its high electronic conductivity at high temperature up to 200 S/cm at 800 °C, large positive thermoelectric power up to 300 °C (p-type semiconductor) and ferromagnetic behavior enabling their applications in sensors and solid oxide fuel cells (SOFCs) [142-144]. The electrical conductivity shows semiconducting behavior with increasing temperature up to 600 °C but it shows constant conductivity between 600 – 900 °C due to competing of oxygen vacancy generations and oxygen recoveries. Above 900 °C, the oxygen vacancy generation is more dominantly occurred that the electrical conductivity is slightly decreased. This high enough temperature of oxygen vacancy dominant regime makes $LaMnO_3$ perovskites more popular materials as cathode as well as protection layer in IT-SOFCs. Better electrical conductivity and catalytic activity can be accomplished by substitution of the trivalent La cation site with divalent alkali earth cations such as Sr^{2+} and Ca^{2+}. Particularly, Sr^{2+} is the most popular for larger ionic size (1.44 Å) compared to La^{3+} (1.36 Å) that provides better structural stability in z-axis by compensating smaller ionic size of Mn^{4+} than Mn^{3+} [145]. The crystallographic structure of 30 % La doped $LaMnO_3$ and the phase diagram of La-Sr-Mn-O system are shown in Figure 4.2. The maximum electrical conductivity is found when the Sr doping ratio increases up to 50 % [146-147]. Higher doping is also ascribed to not only enhancing the electrical conduction but also stronger ferromagnetism due to more unpaired elections in the d-shell of Mn cations via switching the corresponding number of Mn^{3+} to Mn^{4+} indicating generated more positive character for electrical transport [143]. Recently, Sr doped lanthanum manganite (LSM) became a popular cathode layer material in SOFCs as well as an interconnect protection layer for Cr containing metallic alloys.

4.1 First Order Process Map: Linking process parameters to LSM particle thermal and kinetic states

The advent of inflight particle diagnostics has enabled in situ characterization of the in-flight particle state in plasma sprays. Process parameters such as gas flow, current, and hardware (nozzle diameter and torch system) affect the thermal and kinetic energies of the particles which are captured through these inflight particles temperature and velocity measurements.

Figure 4.3 shows the effect of these parametric changes represented through a first order process map. Each point in the figure is an average of LSM particles in the plasma plume conducted at the nominal spray distance of 100 mm from the nozzle exit. The LSM particle temperatures range from 1700 to 2450 ^{o}C while the velocities range from 130 to 350 m s^{-1}. The particle states are roughly divided into three regions. In the regime I (F4 torch and 8 mm nozzle diameter), highest particle temperature and velocity condition B can be obtained by simultaneously applying high hydrogen gas flow and high power. By lowering Ar gas flow rate, lower velocity condition A is achieved. Decreasing the hydrogen flow rate and power, decreases the particle temperature state (condition C). Higher particle velocity regime II (condition D) is achieved by changing to a 6 mm diameter nozzle which increases the effluent gas velocity. Lowest temperature and highest velocity (shortest residential time in the hottest zone of the plasma) regime III (condition E) is achieved by using SG100 torch with internal injection nozzle system and helium as the working gas. Smallest diameter size of nozzle as well as highest Ar-He gas flow rate enhances the particle kinetic energy to the maximum with concomitant reduction in thermal exposure. The development of such maps provides a framework for controlled synthesis of different coating microstructures.

The particle diagnostic technique DPV 2000 also allows examining detailed distributions of the particle temperatures at each of the process map locations. Figure 4.4 displays these distributions for the various process conditions. The high enthalpy parameters represented by the conditions A and B show a single Gaussian type particle temperature distribution with an average of 2217 and 2391 ^{o}C, respectively. Here we note that almost all of the particles display temperatures greater than the LSM melting temperature which indicates fully molten state of the particles. However, spray parameters C and D resulting from lower power and hydrogen in addition to lower average temperature of 2057 and 2089 ^{o}C, showing bi-modal temperature distributions. The first peak is at a constant temperature indicative of the melting peak of the material [135]. Although the LSM powder feedstock has particle size distribution with range of 20 - 53 μm, it appears that the applied thermal energy of plasma may not be sufficient to melt the coarse LSM particles at the conditions C and D. A second contributing factor is the lower residence time of the particles in the condition D due to the higher velocity of the particles. Coating E was deposited at a different spray booth with sensor capable of measuring average in-flight particle temperatures. These differences in particle melting states and superheat have implications on stoichiometry, phase and microstructure of the LSM coatings.

4.2 Microstructure and Stoichiometry of As-Sprayed LSM Coatings

Single droplet characteristics and cross-sectional microstructures of the various LSM coatings are shown in Figure 4.5. As the process temperature and residence time of the particles are increased (conditions A and B), fully molten splats are observed. Such molten splats upon assembly result in dense microstructures of coatings, but these coatings also display discolorations at the interfacial regions suggesting presence of secondary phases. However, the lower temperature processed coatings C, D, and E exhibited significant presence of unmolten particles in the splat and coating microstructures, anticipated from the diagnostic results. These coatings also result in greater porosity associated with unmolten particle entrapment. Increasing the particle kinetic energy, will cause an increase in splat fragmentation (splashing), while the lower velocity processed splats have a tendency to form microcracks. The microstructure of coating B displays the highest density among the five different coatings.

The powder XRD patterns of differently-processed LSM coatings and feedstock powder are shown in Figure 4.6. The intensity of XRD signals are normalized with the highest (110) peak. The patterns for all of as-sprayed LSM coatings contain the peaks of the LSM feedstock powder that indicates the coatings also have the same perovskite structure. However, additional peaks are seen in the patterns of coatings A and B, which likely result from process-induced decomposed phases. The additional peaks are assigned by comparing with all possible elemental compositions in PCPDFWIN v. 2.1 library; signals, +, * and #, indicate $(La,Sr)_2MnO_4$, La_2O_3, and $La(OH)_3$, respectively. More severe phase decomposition is seen in the coating A, where $La(OH)_3$ is observed. The La_2O_3 phase formed through loss of Manganese, being readily hygroscopic reacts with moisture in air after spray process [138]. Moreover, perovskite peaks of coatings A and B are broadened and their intensity is lowered by a factor of 3. This could be evidence that small-sized grains or amorphous phases exist in the coatings A and B, resulting from faster quenching rate. The XRD patterns of coatings C, D and E are very similar to those of the feedstock powder since the coatings are produced at near or lower LSM melting temperature. However, among coatings C, D, and E, as the process dwell time is longer, peaks are broader and intensities are slightly lower as well, indicating finer grain size and potential lattice distortions. Thus, the phases produced at the lowest temperature and shortest dwell time (coating E) are best matched with that of the original powder.

In order to understand the signs of phase decomposition as a function of process parameter, SEM and XRD data were augmented with ICP-OES to quantify coating chemistry. These results are shown in Table 4.2. The elemental wt% of as-sprayed coatings A and B clearly show preferential loss of Mn, estimated to be about 44 and 23 wt%, respectively. Coating A loses more Mn than coating B due to longer dwell time in the flame. This stoichiometric change also results in formation of secondary phases, LSM decomposition products ascribed to the XRD patterns. The amount of Mn loss of the lower temperature processed coatings C and D is estimated to be less than 7 wt% and that of coating E shows only 0.7 wt% based on the composition of the feedstock powder (from Table 4.2).

4.3 Thermal Stability and Oxygen Recovery of As-Sprayed LSM Coatings

In order to understand the thermal history of differently processed LSM coatings, TGA/DSC analysis was employed subjecting free-standing coatings from room temperature to 800 ^oC. Figure 4.7(a) shows thermograms of the feedstock powder (solid line) and as-sprayed coatings. In the figure, no significant thermal degradation is found for LSM feedstock powder up to 800 ^oC, but, as expected, the weight % of all coatings A through E is increased at temperature ranges from 320 ^oC to 700 ^oC in the TGA traces (weight gain starts from 350 ^oC to 590 ^oC for coating A after thermal degradation), due to the oxygen recovery resultant from loss during the plasma spray process. However, the amount of loss is different depending on the spray process parameters. Examining samples exposed to similar process dwell time, higher temperatures processed coatings A and B show less weight gain compared to low temperature processed coatings C and D: due larger Mn loss in coatings A and B. The coating C displayed the highest weight gain among the low temperature processed coatings, as the dwell time also affects the oxygen loss with limited decomposition at the lower temperature range. Thus, the amount of oxygen recovery directly indicates how much manganese ions remain to be oxidized without phase decomposition.

Moreover, the TGA trace of high temperature and longest dwell time sample A exhibits weight loss in two steps; starting at 100 ^oC and 600 ^oC, respectively. These thermal degradations are attributed to thermal decomposition of $La(OH)_3$ second phase seen in the XRD patterns. The first step starts with slow release of water molecules at 100 ^oC and then accelerates at 300 ^oC indicative of $La(OH)_3$ phase decomposition to LaO(OH). In the second step of the thermal decomposition from LaO(OH) to La_2O_3 starts at 600 ^oC [148]. Furthermore, in the TGA, the trend of weight loss above 700 ^{o}C for all coatings can be ascribed to oxygen vacancies creation [142].

Differential scanning calorimetry (DSC) of the feedstock powder and plasma sprayed LSM coatings are shown in Figure 4.7(b). In the figure, DSC provides further elucidation of the weight gains seen during TGA of the coatings B and E. In the DSC, the exothermic peak of coating B, which is indicative of the oxygen recovery, occurs at 335 ^{o}C with low intensity whereas the sharp peak of the coating E appears at 350 ^{o}C. Thus, DSC further discriminates between the TGA observations pointing to differences between B and E coatings; DSC implies there is greater impure phase content in the coating B [149]. The shape of DSC curve of the coating B shows similar to that of the coating C. However, in the coating C, the peak position is not shifted and the amount of exothermic area is much higher, supporting significant oxygen loss without phase decomposition associated with longer dwell time in the plasma. On the other hand, the strong sharp peaks with less exothermic area of coatings D and E indicate rapid re-oxidation to the pure LSM phase with limited oxygen loss. The endothermic peak of the coating A at 330 ^{o}C is mainly caused by the thermal decomposition of water molecules from $La(OH)_3$. The broad exothermic peaks of the coating are followed by the further oxidation and then structural phase transformation.

4.4 Magnetic/Electric Properties

LSM is one of few oxides displaying ferromagnetic properties due to spin-alignment of manganese ions. In order to compare how much manganese ions are reduced or lost at different process conditions, saturation magnetization (M_s) of the as-sprayed and annealed coatings were obtained by extrapolation of the magnetic hysteresis curves. The values of the determined M_s are plotted in terms of product of the process temperature (T) and dwell time (τ), and displayed in Figure 4.8. In the figure, value M_s of the as-sprayed coatings are inversely proportional to the product of T and τ. This result clearly shows that higher process temperature and longer dwell time lower the oxidation state of manganese ions (via loss of oxygen) and phase decomposition in the LSM coatings. In addition, the M_s of hydrogen rich coatings A through D display almost similar values to that of 10 % of feed stock LSM powder. However, the M_s of the helium rich coating E shows 50 % of the feedstock powder. Thus, the M_s value of the coating E could indicate that using helium helps to retain oxygen and manganese in the coatings during plasma processing.

Magnetic hysteresis curves of annealed coatings were also measured after heat treatment at 600 ^{o}C for 2 hours to determine extent of change to manganese oxidation state. The ferromagnetic signals of annealed LSM coating pieces are improved except for coating A, as this coating is severely decomposed. However, the M_s of the annealed coating B shows higher magnetization signal than that of the annealed coating D despite phase decomposition. This opposite trend suggests that the coating density is also a contributing factor as the high-density coatings contain a larger number of spins in the same volume of LSM. Additionally, the annealing process can change the manganese ion oxidation state from Mn^{2+}/Mn^{3+} to Mn^{3+}/Mn^{4+} unless the coatings contain decomposed phases. Therefore, oxidation enhances the manganese ion oxidation state, and that strongly affects the ferromagnetism and electrical conduction in the plasma sprayed LSM coatings.

Room temperature electrical conductivities (σ) of as-sprayed and annealed A through E LSM coatings are displayed in the inset of Figure 4.9 with respect to the product of process temperature (T) and dwell time (τ) (empty and shaded blocks, respectively). The σ of as-sprayed coatings at room temperature tends to increase with increasing process velocity within a similar temperature range (A < B, C < D < E). In contrast, there is no significant difference in room temperature σ for coatings with a similar v process but different temperature (A~C < B~D). As shown in section 4.2, the coating at a higher velocity produces denser microstructures which could provide conduction paths with less resistance. Despite the lower density, coating E shows the highest electrical conductivity at room temperature associated with minimal process induced decomposition. In addition, the trend of room temperature conductivity of annealed coatings is changed after 2 hours heat treatment at 600 °C. Low temperature processed coatings C, D, and E show more enhanced electrical conductivity than high temperature processed coatings A and B. This is due to more effective oxygen recovery in these low temperature processed coatings (then corresponding to the amount of Mn^{4+} generated during the heat treatment), providing more holes and enhancing electrical conductivity. Therefore, stoichiometry of LSM, which is a function of process T and v, affects their electrical performance at room temperature.

Temperature-dependent electrical conductivity was measured for LSM coatings which were thermally cycled from room temperature to 200 °C, 400 °C and 600 °C in the tube furnace and tracked the activation energy change with temperature. Since the electrical conduction mechanism of LSM is based on small polaron hopping, it is governed by the Arrhenius equation [150] below

$$\sigma T = (\sigma T)^{\circ} \exp\left(-\frac{E_a}{kT}\right) \quad \text{— (4.3)}$$

, where $(\sigma T)^{o}$ and E_a are pre-exponential constant and activation energy, respectively. Figure 4.9 shows the Arrhenius plot, $\ln(\sigma T)$ vs. $1/T$, of coating E and there is no significant slope change at which temperature of the coating increases up to 200 ^{o}C and then decreases to room temperature. Thus, the calculated E_a of as-sprayed coatings is 0.194 eV for coating E. On the other hand, the slope change is detected by offset from the extrapolation line at 342 ^{o}C when temperature is increased to 400 ^{o}C. This significant slope change could show the oxidation starting temperature and the slope is lowered during quenching. This temperature is corresponds to the temperature where the weight gaining starts in TGA. A further slope change is detected at 470 ^{o}C during the third cycle, where the temperature was elevated up to 600 ^{o}C. In addition, the presence of a kink is observed at around 570 ^{o}C due to the phase transformation from the orthorhombic to rhombohedral structure, which is attributed to the further oxidation of Mn^{3+} to Mn^{4+} [145]. The temperature of the phase transformation of LSM is known to rely on the amount of oxidation, which could have an influence on the switching amount of Mn^{3+}/Mn^{4+}. In the quenching process, the E_a of coating E is lowered to 0.15 eV. Therefore, the total oxygen recovery could occur by the two steps in the thermal sprayed LSM coating; (1) divalent manganese ions are first oxidized to trivalent manganese ions at 342 ^{o}C. (2) The trivalent ions are oxidized to the quadrivalent manganese cations at 470 ^{o}C. Hence, the further second oxidation may lead to the structural phase transition at 570 ^{o}C. The activation energy values of as-sprayed, after the cycle from 600 ^{o}C as well as after further heat treatment for 24 hours at 800 ^{o}C of coatings A through E are shown in Table 4.3.

Figure 4.10 shows temperature dependent conductivity during furnace cooling from 800 ^{o}C to room T after 24 hours hold at 800 ^{o}C. The results display semiconductor-like electrical behavior. When held at 800 ^{o}C for 24 hours, the oxygen content recovers in the LSM coating and enhances electrical conductivity, but the enhancement of σ is differently for different processed coatings; the high temperature processed coatings A and B show slow enhancement due to the limit of oxygen recovery, however, the lower temperature processed coatings C, D and E show faster enhancement rate due to limited stoichiometry change induced by processing. Moreover, the porosity and unmolten particles in the microstructures of coating appear to undergo rearrangement during long term heat treatment. Coating E, despite presence of unmelted particles (low thermal energy of process), shows the highest σ among coatings C, D and E, all with similar stoichiometry. After 24 hours exposure at 800 °C, σ of coating E enhanced up to 55 S cm^{-1} and its activation energy is also lowered to 0.112 eV. This value although significantly lower than fully dense LSM at 200 S cm^{-1} is still respectable from an application point of view [142-143,145-146]. There is an anomaly in the σ-T curve at 60 °C, indicative of the Curie point for ferromagnetic-paramagnetic transition of LSM coatings [147]. Thus, maintaining phase stoichiometry during processing is a critical factor for enhancing σ via oxygen recovery of the plasma sprayed LSM coatings.

4.5 Oxide Scale Growth

Oxide scale growth studies were performed through isothermal exposure at 800 °C for 600 hours in air on all the coatings. A 50 μm thick coating was applied to 18 wt% Cr-containing ferritic steel (ATI441HP™, FS) substrate, a benchmark interconnect alloy used in SOFC application. An uncoated alloy was used to benchmark the oxide scale. Figure 4.11 cross-sectional SEM images and corresponding EDX line profile at the interface for the various exposed coating substrate systems. The results are displayed within the framework of the *T*-*v* map to illustrate processing influence. The results show coatings B through E show similar oxide scale thickness of less than 3 μm without further cracking and delamination of coatings. The

EDX profiles show primarily Cr and O elements at the coating/ferritic steel interface indicative of Cr_2O_3 phase formation. For reference, oxide scale thickness of uncoated ferritic steel exposed to identical conditions was about 10 μm (not shown). However, the coating A shows abnormally thick 30 μm oxide scale which resulted in LSM coating delamination. EDX profile suggests there are three sub-scales in this coating; chromium oxide (Cr_2O_3) near the FS substrate, iron oxide (α-Fe_2O_3) closer to the LSM layer and mixed chromium-iron-spinel phases ($FeCr_2O_4$, $[Fe^{3+}_{2-x}Cr^{3+}_xFe^{2+}]O^{2-}_4$, and Fe_3O_4) between these two layers [151-152]. Since values of their coefficient of thermal expansion (CTE) at 800 ℃ are known approximately 9.6, 14, 7, 11-12, and 28 x 10^{-6} K^{-1} for Cr_2O_3, α-Fe_2O_3, chromium spinels, ferrite spinels, and Fe_3O_4, respectively [153-155], the thick layers of chromia, chromium spinel and ferrite in the LSM coating A may cause the coating delamination which could leading to failure of the interconnect protection layer. However, this is a unique observation only seen in one of the parametric conditions.

These atypical observations suggest that oxidation behavior of parameter A applied coating on steel follows a different oxidation mechanism. As shown earlier, coating A contains La_2O_3 second phase which is known to be hygroscopic. Based on the equation (1) and (2), the chromia layer first reacts with oxygen and water from the injected air at the interconnect surface to grow toward the LSM layer. If the coating contains hygroscopic La_2O_3, water molecules can be easily absorbed and then diffuse into the interfaces between interconnect and LSM. Hence, the growth rate may be enhanced. However, in most coatings absent the La_2O_3 phase, oxygen diffuses only 4.0 x 10^{-15} cm^2 s^{-1} in the 20 % Sr doped-lanthanum manganite layer [145] and the diffusion rate of water vapor would be governed by the concentration gradient of water molecule. Although it could not completely block the chromia diffusion into the LSM layer the growth rate is expected to be sluggish. Thus, selecting process conditions that avoids free La_2O_3 generation during plasma spraying is an important control element for the SOFC application.

4.6 Conclusions

In this study, 20% Sr-doped lanthanum manganite coatings were produced via plasma spray. Coatings were produced using different process excursions by varying plasma torch hardware, torch current and plasma gas ratios. The resultant effluent spray stream was quantitatively characterized for their thermal and kinetic states using in situ diagnostics and subsequently displayed using a process map strategy. It was found that phase and stoichiometry of the coatings were affected by the type and extent of thermal exposure. Particles exposed to high temperatures experience full melting and thus high density, but also suffer from significant manganese and oxygen loss and phase decomposition. Coatings produced from lower thermal energy particles, contain more porosity and unmelted particles resulting in lower density but also minimal decomposition. Oxygen is recovered during subsequent thermal exposure but the extent of recovery depends on initial coating chemistry. The temperature dependent transport properties indicates semiconducting behavior of the coatings, with lower temperature processed coatings displaying 10 times higher electrical conductivity values up to 55 S cm^{-1} than that of high temperature processed coatings. Most coatings are effective against chromia poisoning in SOFC application. However, when the particles undergo severe decomposition, free La_2O_3 can form which can have deleterious effects on protective mechanisms. The results from this paper suggest that plasma spray is an effective method for producing functional multi-component oxide coatings, but also point to need for fundamental understanding complex relationships among process, microstructure, stoichiometry and properties.

5. Plasma Sprayed Manganese-Cobalt Spinel Coatings: Process Sensitivity on Phase, Electrical and Protective Performance

For more than a decade now, $Mn_xCo_{3-x}O_4$ (MCO) spinels have been considered as rare-earth alternative conductive oxides to impart protection to metallic interconnects [44,48-52,56]. They offer excellent electrical conductivity at typical cell operation temperature, ~60 S cm^{-1} at 800 ^{o}C [155-157], good electrochemical performance [156], reasonable thermal expansion compatibility with ferrous alloys (CTE: 11-13 × 10^{-6} K^{-1}) [157], and chemical stability with other cell components. Following the initial discovery of interesting structural and magnetic properties of MCO in 1958 by Wickham and Croft [158], significant scientific research [159-165] has been conducted as well as applications [166-167] of the material have been contemplated. In order to elucidate their electrical conduction mechanism, several researchers have tried to investigate their cation distribution in terms of Mn/Co ratio using X-ray fluorescence spectra [168], neutron diffraction [169], and electronic structure calculation [170]. Structural studies found Mn ions preferentially occupy B site (octahedral site) and cubic spinel phase structure starts to distort above 55% occupancy of Mn^{3+} [159]. The phase diagram of Mn_3O_4-Co_3O_4 system is provided in Figure 5.1. Electrical conduction takes place by electrons hopping between adjacent different oxidation state cations in the octahedral site, Mn^{3+}/Mn^{4+} or Co^{2+}/Co^{III}, because their atomic distances are the shortest [160,169]. (see Figure 5.2) The electrical conductivity of bulk $MnCo_2O_4$ is reported to be 60 S cm^{-1} at 800 °C while that of bulk $CoMn_2O_4$ has only shown 6.4 S cm^{-1}; almost 10 times difference of electrical conductivity [155] is due to the availability of additional Co in the unit cell that has shorter electron hopping distance in the octahedral sites than Mn-Mn.

5.1 First Order Process Map of MCO coatings

The diagnostic results of particle temperature and velocity (*T-v*) were represented in a first order process map as shown in Figure 5.3 [171]. A F4 MB-XL gun with a 8mm nozzle was used for coatings A-C located on the low velocity regime with varying temperature. By switching nozzle size from 8 mm to 6 mm for condition D, particle velocity was increased with concomitant reduction in particle temperature due to reduced dwell time of particles in the plume. A Praxair TAFA SG100 plasma torch with a 4.5 mm nozzle and internal particle injection was used to produce particles at high velocities with minimal thermal exposure. This is designated as the condition E in the particle *T-v* map. The particle temperature distributions of all of conditions obtained from the DPV2000 sensor show higher range than the melting temperature of MCO (1650–1700 ^{o}C), indicating that the majority of the particles underwent melting during the spray process (Figure 5.4).

5.2 Microstructural Characteristics of MCO Coatings

Microstructure and EDX spectra of the MCO feedstock powder and cross-sectioned as-sprayed coatings C and E are shown in Figure 5.5. Feedstock particles show agglomerated and sintered structure with narrow size distribution but they contain unevenly brighter surface regimes (See the box in Figure 5.5(a)). In order to examine chemical composition of the bright regime, the electron beam is focused on the circled area in Figure 5.5(b) and the EDX detector indicates Co dominant metallic phase in the bright regime. The bright regime is also seen in cross-sectioned coating microstructures. Figure 5.5(d) and (g) are 10k magnified images of coating C and E. Their chemical compositions of the coating matrices and bright regimes are compared. Figure 5.5(e) and (h) represent chemical composition of matrix regimes of coatings C and E, respectively, which indicate that both coatings contain Mn-Co-O composition. However, EDX spectra of bright regimes (Figure 5.5(f) and (i)) show similar patterns to that of feedstock powder (Figure 5.5(c)) with less noticeable oxygen peak. Thus, the brighter regime in the coatings is the reduced cobalt dominant metallic phase originating from the feedstock powder. Cross-sectional microstructures at 3k magnification of coatings A-E are represented in corresponding locations to their respective particle thermal and kinetic energies identified in the *T*-*v* map as shown in Figure 5.6. Also, the average porosity of coatings calculated by image analysis is displayed. Coatings deposited at high particle temperatures and medium velocity plasma condition (such as coating B) show the highest density compared to those sprayed at lower temperature such as coatings C and D, which exhibit relatively porous microstructures. In addition, microstructural microcracking was apparent in the coatings that were sprayed at lower particle velocity conditions. This microcracking is attributed to the large quenching stresses associated with the rapid solidification of the depositing particles. Because particles are exposed to the high thermal energy (with longer in-flight thermal exposure) the resultant splats are subjected to larger tensile quenching stresses and thus greater propensity for cracking [172]. Coating E, on the other hand, had high porosity (~10 %), preferentially showing void structure, originating from the unmolten character of the particles at this high velocity plasma condition. Even with sufficiently high particle temperature, the high velocity did not allow adequate residential time for the particle in the plasma plume, which resulted in limited melting of depositing particles.

5.3 TGA/DSC

In order to establish the proper post-annealing temperature, thermo-gravimetric analysis (TGA)/differential scanning calorimetry (DSC) were used. Figure 5.7 shows typical TGA/DSC curves of D coating. In the TGA curve, weight gaining starts at 352 ^{o}C, corresponding to temperature sharp exothermic peak is emerged in the DSC curve which indicates oxygen recovery. Subsequently, TGA suggests further oxidation as observed by the increasing weight while broad exothermic peak is observed in the DSC (after the peak corresponding to oxygen recovery) which corresponds to the metastable amorphous phase relaxation at relatively low *T* of phase transition starting point ~ 620 ^{o}C (confirmed by temperature dependent XRD, discussed in detail in the later sections) [173]. After the phase transition, DSC shows a sign change from exothermic to endothermic as well as the slope of weight gain is also decreased in TGA at 700 ^{o}C where oxygen vacancy generation and oxygen recovery processes start competing. Based on the TGA/DSC analysis, post-annealing process was carried out at 700 ^{o}C to maximize oxidation state of MCO coatings.

5.4 Phase structures of MCO Coatings

XRD of as-sprayed and annealed coatings A-E with feedstock powder are shown in Figure 5.8(a) and (b), respectively. The patterns of MCO feedstock powder displayed a combination of cubic $MnCo_2O_4$ (space group *Fd-3m*) and tetragonal Mn_2CoO_4 (space group *I41/amdS*) spinel phases with 2:1 weight ratio as refined by quantitative Rietveld method. The broad diffraction profiles mirror the small crystallite sizes, i.e. coherently scattered domains which belong to the lower tens of nanometers size range. The coexistence of cubic and tetragonal phases, with stoichiometry range of x = 1.3 to 1.9 in $Co_{3-x}Mn_xO_4$, and their broad diffraction profiles are in accordance with literature findings [174], confirming the appropriate phase content in the feedstock. XRD patterns of as-sprayed coatings A-E deviate from that of the feedstock. The intensities of spinel reflections are reduced and broadened, and additional reflections corresponding to CoO rock salt phase (space group *Fm-3m*) are apparent. MnO phase, although a rock salt phase similar to CoO, is not observed in any of the sprayed coatings. This can be attributed to the significant larger lattice parameter of MnO compared to that of CoO. More discussion on the preferential phase evolution of CoO is carried out in the next section. The reflections of rock salt phase are most intense for coating A and the least for coating E. This is mirrored in the results of quantitative Rietveld refinement presented in Figure 5.9(a) where the rock salt phase forms about 80 wt% of coating A and coating B being closer to A, while its presence in coating E is less than 60 wt% with coating D being closer to E. Hence, conditions that processed with the shorter dwell times (high v condition) and that used helium generates less amount of rock salt phase, on the other hand, high T and low v conditions lead to higher content of rock salt.

Room temperature XRD is re-examined with post annealed MCO coatings at 700 ^{o}C for 2 hours. Indeed, the annealed coatings exhibit more pronounced spinel reflections (as seen e.g. in XRD pattern of annealed coating A), but the CoO phase still remains trapped, especially in high T and low v conditions (high thermal energy exposure of coatings A and B). This phase recovery indicates metastable rock salt phase located in between liquid and spinel phases in the Mn-Co-O phase diagram [159-160] is trapped in the as-sprayed coating by rapid quenching spray process of ~10^6 K s^{-1} rate [175]. Aiming at detecting differences between the annealed coatings, Rietveld refinement was performed with the same structural information as for as-sprayed coatings and the results of the phase quantitative presence in the irradiated volumes are summarized in Figure

5.9(b). Ensuring that the lattice parameters had not deviated from the viable range, their refined values were checked and are presented in Table 5.1. All the refined lattice parameters are within the range seen in ICSD database except for those of CoO that are larger in comparison to the a = 4.230 to 4.273 Å range; for comparison MnO phase has lattice parameters ranging from 4.408 to 4.538 Å. As shown for the rock salt phase in Table 5.1, the difference between as-sprayed and annealed state is virtually nonexistent. Larger dimensions of CoO lattice indicate that a form of substitution occurs and/or interstitials are present. In fact, the substitution of Co ions by Mn ions leads in general to unit cell expansion [176-177] and the rock salt is most probably disordered (Co, Mn)O. Unfortunately, the poor peak-to-background ratio and broadened reflections do not facilitate refinement of the site occupancy factor (SOF) for this phase. Moreover, the annealed coatings can be grouped into two batches according to values in Table 5.1; the coatings A-C having larger CoO and $CoMn_2O_4$ lattices on one side and coatings D-E produced at high velocities with smaller CoO and $CoMn_2O_4$ lattices on the other. As for the quantitative presence of rock salt in the annealed coatings, it follows the trend seen in the as-sprayed coatings with coatings A and B having the largest amount of rock salt phase in comparison with coatings D and E with less than 20 wt%. The transformation from rock salt phase follows the common wisdom [178] that the CoO converts to spinel structure if heated to 600-700 ºC.

In order to gain more information about the phase recovery process from the metastable rock salt phase to the stable spinel phase, as-sprayed coatings (A-E) were crushed into powder and temperature dependent XRD was carried out. The powder XRD patterns were taken at the following temperatures: 25, 500, 530, etc with a 30 ºC increment in temperature up to 800ºC with a dwell time of 10 minutes at each temperature, and upon slow cooling, patterns were also taken at 500 ºC and at 25 ºC. The transition temperature from rock salt phase to spinel with tetragonal structure is about 620 °C as seen specifically for coating A in Figure 5.10. Nevertheless the transition took place at virtually the same temperature level for all A-E coatings. Rietveld refinements of the XRD patterns taken at 800 °C showed that the spinel formed over 80 wt.% of the irradiated volumes (we excluded the regions corresponding to diffraction of PtRh heating filament during evaluation) for all coatings and the amount of spinel barely changed after cooling to room temperature.

5.5 Magnetic Properties

Magnetic hysteresis of the feedstock powder and the as-sprayed and annealed coatings are measured from –1 Tesla to +1 Tesla using a VSM instrument in order to understand electrical conduction mechanism of plasma sprayed MCO coatings. Saturation magnetization (M_s) values are decided by extrapolation from the top and bottom plateaus to y-axis (See Figure 5.11(a)) and are then averaged. The extrapolated M_s values of as-sprayed and annealed MCO coatings are plotted (Figure 5.11(b)) with respect to the product of average particle temperature (T) and dwell time (τ), which numerically represents the exposure to thermal energy during the process. Comparing the M_s values of MCO coatings deposited under different processing conditions is an indication of the oxidation state of Mn and Co in the coatings. Firstly, the powder contains a mixture of $MnCo_2O_4$ and Mn_2CoO_4 with a 2:1 ratio which is confirmed by XRD Rietveld analysis. It is known that manganese preferentially occupies the octahedral site, thus Co^{2+} occupies tetrahedral sites and the rest of Mn^{3+}/Co^{III} and two of Mn^{3+} occupy octahedral sites for $MnCo_2O_4$ and Mn_2CoO_4, respectively. Since the coatings electrically conduct via the hopping of adjacent cations in octahedral sites, their formula can be written as $Co^{2+}[Co^{2+}_xCo^{III}_{1-x}Mn^{3+}_{1-x}Mn^{4+}_x]O_4$ and $Co^{2+}[Mn^{3+}_{2-y}Mn^{4+}_y]O_4$ [162-163]. The Co^{2+}($d7$) in tetrahedral sites has a high spin state with higher t_{2g} orbital energy than that of e_g orbital, and hence comprises of 3 unpaired electrons in each tetrahedral site. However, *d*-orbitals in octahedral sites split in opposite ways to tetrahedral due to the difference of bonding position with oxygen atoms, thus e_g shows a higher energy level. Trivalent Mn^{3+}(*d4*) with high spin has 4 unpaired electrons while Co^{III}(*d6*) with low spin has none. Thus, $Co^{2+}Mn^{3+}Co^{III}O_4$ has 7 unpaired electrons and $Co^{2+}Mn^{3+}Mn^{3+}O_4$ has 11 unpaired electrons, respectively. Hence, there is an average of 8.3 unpaired electrons per molecule in the feedstock powder and the extrapolated M_s value of feedstock powder shows 0.615 emu g^{-1}. However, M_s of as-sprayed coatings A-C shows lower magnetization than that of feedstock powder, while those of coatings D and E show higher magnetization. This categorized magnetic signal appears to be closely related to the lattice parameters of (Co, Mn)O and $CoMn_2O_4$. During the deposition of coatings A-C the particles were exposed to high thermal energy and consequentially large thermal gradients within the plasma plume. Moreover the increased hydrogen flow rates and the reduced particle dwell time arising from the nature of the processing condition resulted in coatings undergoing oxygen loss in-flight. The ensuing rapid quenching of the particles resulted in the formation of metastable (Co, Mn)O phases with larger lattice parameter which indicates the disordered rock salt phase. Since coatings A-C mostly contains antiferromagnetic rock salt phases (Co, Mn)O and minimal amounts of non-stoichiometric MCO (due to process induced oxygen losses) the total number of unpaired electrons in these coatings is reduced.

However, the actual number of unpaired electrons per molecule is increased to 11.7 if we assume that non-stoichiometric MCO has only the lowest oxidation state of Mn^{2+} and Co^{2+} with broken *d*-orbitals degeneracy which can be attributed to lower orbital splitting energies due to the loss of oxygen. Coatings D and E that were processed with high velocity (less thermal exposure) plasma process using helium instead of hydrogen (only condition E) show increased magnetism even though they also contain antiferromagnetic (Co, Mn)O phases. However, none of the annealed coatings shows magnetic hysteresis even though their spinel phase is recovered from metastable (Co, Mn)O phases (see Figure 5.8(b), 5.9(b)). It still remains unclear as to why their magnetic property changed. It is likely that ferrimagnetic ordering might have taken place during the heat treatment associated with antiferromagnetic exchange between tetrahedral Co^{2+} and octahedral Mn^{4+} cations [163].

5.6 Electrical Conductivities of MCO Coatings

Temperature dependent electrical conductivities (σ) of MCO coatings were measured from room temperature to 800 °C and the results are plotted using $\ln(\sigma T)$ vs. T^{-1} form. The electrical conduction mechanism is known to be small polaron hopping between the adjacent metals occupied in octahedral sites which is governed by the Arhenius equation (Figure 5.12) [169]. From room T up to ~ 130 °C (0.0033 – 0.0025 range of T^{-1} (K^{-1})), electrical conductivity gradually increases but the conductivities of coatings A-D show discontinuities in the temperature range from 130 °C to 160 °C (0.0025 – 0.0023 range of T^{-1} (K^{-1})) as indicated by arrow in Figure 5.12. This unusual conductivity discontinuity is also seen in coating E but at a different T range of 93-101 °C (~ 0.0027 in T^{-1} (K^{-1})). Above 160 °C (101 °C for coating E coating), conductivity continues to increase with raising temperature. However, the slope is slightly higher than that which was observed between room temperature to 130 °C which is indicative of the change in activation energy (E_a) of coatings post the unusual fluctuation. This large fluctuation (~ 10 times) in electrical conductivity might be attributed to cubic-tetragonal phase transition at this temperature range. In order to prove the hypothesis that the fluctuation is associated from phase transition, temperature dependent XRD has been re-employed and measured from 130 to 200 °C with 10 degree intervals and analyzed for each phases' quantity via Rietveld analysis. Initially, the quantity of more conductive cubic $MnCo_2O_4$ phase decreases while the content of less conductive tetragonal Mn_2CoO_4 phase increases with increasing temperature from 130 to 170 °C. Then, the amount of cubic spinel phase increases while tetragonal spinel phase decreases from 170 to 200 °C. The results of phases' quantity analysis are shown in Table 5.2. During further increasing T (350-450 ^{o}C), the conductivity curves show some kinks at the temperature that TGA indicated the initiation of oxygen recovery. Furthermore, rapid rises of conductivity at around 600 ^{o}C are observed where the phase transition from metastable rock salt phases to spinels occurs. Beyond this up to a temperature of 800 ^{o}C, electrical conductivities continue to increase with different slopes (E_a). Electrical conductivity has also been measured during isothermal exposure at 800 ^{o}C for 24 hours (time dependent conductivity curves are not shown). During the isothermal exposure, conductivity further increased through the recovery of spinel phases as shown in the inset of Figure 5.12 after 24 hours exposure. Coatings A and B show lower electrical conductivity despite their dense microstructures, which is attributed to the presence of more metastable rock salt phases resulting from higher plasma energy exposure and H_2 content at these conditions (XRD results in Figure 5.9(b)). Coatings sprayed at parameters incorporating lower hydrogen content (C and D) as well as those deposited using He containing plasma (E) show higher electrical conductivity (up to 40 S cm^{-1} for E coating) due to more appropriate phase retention with smaller lattice parameters of conductive phases, $MnCo_2O_4$ and Mn_2CoO_4, which provide shorter electron hopping distances. This value is about 67 % of bulk MCO. Continued measurements of conductivity during the cooling cycle show a linear behavior (only shown for coating E). Activation energies (E_a) of coatings A-E are calculated from the cooling curves using Arrhenius equation with data summarized in Table 5.3. The lowest E_a is 0.40 eV corresponding to that of coating E while coating B shows the highest E_a of 0.64 eV. The result points to the importance of stoichiometry and phase retention over coating density on electrical performance.

5.7 Oxide Scale Protection Performance of MCO Coatings

Oxide scales of these MCO coatings (A-E) on ferritic steel were grown by subjecting them to a thermal excursion of 800 ^{o}C for 20 and 600 hours in a tube furnace. Subsequently oxide scale growth and their cross-sectional images are investigated by SEM along with chemical analysis via EDX (Figure 5.13). Since the atomic profile of EDX only shows one specific location of the sample, averaged values from multiple location measurements along with their standard deviation following exposures of 20 hours and 600 hours are also presented in Figure 5.13(d) and (h), respectively. While the microstructures of coatings B, D and E heat treated for 600 hours appear similar, possibly due to the effects of sintering, coatings A and C showed signs of significant crack formation. Denser coatings obtained from higher process temperature and velocity show sluggish oxide scale growth. Oxide scales of coatings B and E after heat treatment for 600 hours are only about 1 μm. However, low velocity processed coatings A and C show about 50 μm thick grown oxide scales with large variability. This could possibly be due to the easy pathway available for the diffusion of volatile Cr species through the microcracks present in these coatings. The growth of oxide scales was found to vary between coatings A and E. The oxide scale in coating A exhibited a growth rate of 0.8 μm h^{-1} for the initial 20 hours and then slowed down to 0.06 μm h^{-1} for the next 580 hours, which was still about 45 times faster than the growth rate observed in coating E. This thick grown oxide scale between FS substrate and MCO coating causes crack propagation within the MCO coating in either the vertical or perpendicular directions as shown in Figures 5.13(e) and (f). This leads to the catastrophic failure of the protective layer as result of delamination of the coating. These results point to the need for adequate density in sprayed MCO coatings to impart resistance to failure arising from the growth of oxide scales.

5.8 Coefficient of Thermal Expansion of MCO Coatings

Finally, coefficient of thermal expansion (CTE) of coatings was measured to assess mechanical stability with the other cell components (dL L_o^{-1} and CTE curves of coating D are displayed in Figure 5.14). The percent change in length, dL L_o^{-1} curve shows linear thermal elongation up to 800 ^oC but a constant CTE of 11.0×10^{-6} K^{-1} was observed only up to 700 ^oC and a sudden drop in CTE was observed above 700 ^oC. This is likely related to the metastable rock salt phases transition to stable spinels. These findings suggest that the coatings investigated in the current study could be reliably utilized at temperatures below 700 ^oC.

5.9 Conclusion

In this investigation, MCO coatings were deposited by APS to examine the effect of process induced thermal excursions on the phase, microstructure and electrical properties. The process dependence on the efficacy of the coating to provide requisite protection to SOFC metallic interconnect from chromia scale is also investigated. MCO coatings were subjected to deliberate thermal excursions within the plasma spray process through modifications to process parameters including hydrogen content in the plasma gas, arc current, and total gas flow. Torch hardware configurations were also varied to provide a wide window of particle thermal and kinetic energies. The resultant process map was used to benchmark coating attributes such as density and phase contents. Particles exposed to high thermal energy and high kinetic energies result in coatings with dense microstructures while those produced at low temperatures and velocities produce coatings with significant porosity. In almost all cases, the as-deposited coatings contain two different stoichiometric spinel phases, Mn_2CoO_4 and $MnCo_2O_4$, with a trapped metastable rock salt phases with (Co, Mn)O chemical formula. This result is not surprising and is attributed to the rapid quenching ($\sim 10^6$ K s^{-1}) occurring during the plasma spray process. Post deposition annealing allowed recovery of spinel phases from the metastable rock salt structure as confirmed via *T*-dependent XRD measurement with a transition *T* of 620 ^oC. However, substantial differences in initial and post-anneal phase contents resulted from different process conditions. Coatings that retained a higher fraction of the desirable spinel phases (e.g. coating E produced at high kinetic energies, less thermal exposures) showed excellent electrical conductivity of up to 40 S cm^{-1} at 800 ^oC. Correspondingly, coatings with high density achieved through a combination of high thermal and kinetic energies (e.g. coating B) show excellent oxidation protection of the underlying metallic interconnect. The results point to both efficacy of plasma sprayed functional oxides in SOFC applications as well as the need for fundamental understanding of the interplay among process conditions, phase evolution, microstructure and properties to ensure requisite performance.

6. Tunability of Thermoelectric Properties of in situ Thermal Spray Synthesized Substoichiometric TiO_{2-x}

6.1 Manipulating thermal exposure by dwell time and temperature

TiO_{2-x} coatings are produced by the thermal spray process with starting feedstock stoichiometry of $TiO_{1.9}$. Two different coating techniques with varying spray parameters and hardware are applied in order to manipulate the thermal excursion of particles. Average temperature (*T*) and velocity (*v*) of the particles in the plasma/flame are monitored in situ during the spray process and presented on a 1st order process map in order to visualize the thermal and kinetic energies of the conditions (Figure 6.1). *T* and *v* of plasma-sprayed coatings are located at high *T* (2500-3800 K range) and low *v* (180-250 m s^{-1} range) regime while HVOF processed coating is scattered at low *T* (~2300 K) and high *v* (~900 m s^{-1} range) regime on the map. With increasing hydrogen ratio in the plasma, the average particle *T* is increased but the average particle *v* remains almost constant. Two different types of plasma guns have been employed: F4MB-XL and SinplexPro™. Compared to when the F4MB-XL gun is used, when the SinplexPro™ is used conditions are displayed in the higher *T* and *v* range because the plasma gun is known that has better plasma plume stability, based on its cascaded arc technology, whereas the conventional F4MB-XL gun generates the plasma with continuous on-and-off of electric arcs at high frequency. In this chapter, F4MB-XL and SinplexProTM plasma torches refer to Conv and Cas, respectively. Coatings prepared with 7 different conditions are represented as (type of gun used-amount of hydrogen used), i. e. Conv-0, 4, 12, Cas-0, 3, 9 and HVOF.

6.2 Phase and Stoichiometry via XRD

XRD patterns of as-sprayed coatings and feedstock powder are shown in Figure 6.2. The patterns of feedstock powder showed a mixture of Rutile and Magnéli phases (Ti_nO_{2n-1}) with n = 5 – 9 with sharp reflections that indicate the phases have large crystallite sizes, i.e. too large to be determined by profile analysis of XRD patterns. XRD patterns of as-sprayed coatings deviate from that of the feedstock, which indicates that particles experienced phase decomposition during the spray process. For the as-sprayed coatings' surfaces, the reflections' intensities are reduced and broadened, mainly due to the decrease in the coherently diffracting domain sizes. Moreover, the coatings can be categorized into three distinct groups according to the similarity of XRD patterns; (1) HVOF, (2) non-hydrogen used plasma (Conv-0 and Cas-0) and (3) hydrogen used plasma (Conv-4, 12 and Cas-3, 9). The pattern of coating HVOF most closely resembles the feedstock phase contents with a majority of Magnéli (n=8 and 9) phases and Rutile because of minimal thermal exposure during the process. However, the profiles are broad due to significantly lower crystallite sizes on the as-sprayed surface compared to the feedstock. Non-hydrogen processed coatings Conv-0 and Cas-0 shows similar XRD patterns with more pronounced Rutile peaks except for the zirconia impurity reflections (2 theta ~30, 50, and 60 deg) in coating Conv-0. Since the hydrogen-free plasma provides oxidizing environment to the particles, the generation of the more oxidized phase, i.e. Rutile is favored. Thus, the XRD patterns show strong Rutile reflections with profile analysis indicating crystallite sizes of ~45 μm compared to the even broader reflections from the remaining Magnéli (n=5 and 6) phases which have crystallites smaller than 10 μm. Meanwhile, the patterns of hydrogen-containing plasma coatings, Conv-4 and 12 and Cas-3 and 9, are similar to those of hydrogen-free plasma coatings with a lower intensity of Rutile reflections. One notable difference is the emergence of new reflections at 2 theta ~21, 26, 32, 53, and 55 degrees which implies the presence of a new reduced phase of Ti_4O_7. These reflections are more noticeable if the hydrogen content in the plasma is increased and, hence, supplies more thermal energy which can preferentially evaporate oxygen atoms.

In order to quantitatively analyze the phase contents in the feedstock and coatings, Rietveld refinements were attempted. The results are mapped on the process-dependent space (phase contents as a function of thermal exposure ($T\ x\ \tau$)) in order to visualize the process effect on phase changes in the coatings compared to the phases of the original feedstock powder, where $T \times \tau = 0$ (see Figure 6.3). The quantitative Rietveld analysis of feedstock showed a dominance of Magnéli phases (Ti_nO_{2n-1}) with n= 5 – 9 (the most abundant phase is Ti_9O_{17} with 38 wt%); there is also ~17 wt% of Rutile, ~4 wt% of beta-TiO_2 and less than 1 wt% of Anatase. Based on the refined quantities, the computed feedstock stoichiometry is $TiO_{1.896}$ which matches well the data provided by the powder manufacturer. The coating processed with minimal thermal exposure (HVOF) shows the most similar phase contents to the original; it is the only coating that contains Magnéli phases with n = 7 – 9 (see Figure 6.3(b)) while the phases are decomposed during the other plasma sprayed processes. Hydrogen-free plasma sprayed coatings Conv-0 and Cas-0 show increased Rutile content up to 44.8 % due to their oxidizing environment, but the rest of original Magnéli phases (n = 5 – 9) transform to the reduced forms (n = 5 and 6) (Figure 6.3(a) and (c)). Although the coatings contain more Rutile phase (TiO_2) compared to that of feedstock, the average stoichiometry is reduced to $TiO_{1.879}$ and $TiO_{1.890}$ for coatings Conv-0 and Cas-0, respectively, due to the presence of reduced Magnéli phases (Ti_5O_9 and Ti_6O_{11}). Hydrogen-containing-plasma sprayed coatings Conv-4, 12 and Cas-3 and 9 show more reduced Magnéli phases (Ti_4O_7, Ti_5O_9 and Ti_6O_{11}) than the higher oxygen content Magnéli phases

(Ti_9O_{17}, Ti_8O_{15} and Ti_7O_{13}) while the amount of Rutile is practically constant, due to the reducing environment of the plasma (Figure 6.3(a) and (c)). With increase of thermal exposure ($T \times \tau$), the Ti_4O_7 phase is apparent while the Ti_6O_{11} phase is decreased (Figure 6.3(a) and (c)). This reducing transition pattern (generating lower number of Magnéli phases from the existing higher number of Magnéli phases, and not generating existing Magnéli phases from Rutile) suggests that phase transition within the Magnéli phases is more energetically favorable than transformation from Rutile to Magnéli phases, which implies that adding oxygen vacancies by generating stacking fault planes is easier than changing the crystallographic structure from tetragonal (Rutile) to triclinic (Magnéli phases, n = 4 – 9). Thus, the average stoichiometry of the coatings is lowered to $TiO_{1.836}$.

6.3 Microstructure Analysis

Microstructures of the differently-processed splats (the basic building block) and coatings are investigated using SEM/EDX and their selective images are displayed in Figure 6.4(a) - (e). As a result of image analysis, average porosities are obtained in the range of 2.3 – 4.6 %, which indicates that dense-microstructured coatings are obtained by thermal spray processes despite the existence of voids, globular and interlamellar pores, and microcracks. The porosity of the coatings as a function of thermal exposure is shown in Figure 6.4(f). With increasing process temperature (T) and velocity (v), coating density is increased. Coating produced with a conventional plasma torch containing no hydrogen (Conv-0) contains the highest porosity due to existing “unmelts” (see Figure 6.4(a) splat), although the shape of the splats is a pancake-like structure without any splashing. However, with increasing hydrogen ratio in the plasma, the degree of the porosity in the coatings decreases due to better melting. Coatings produced with a cascaded plasma torch (Cas-0, 3, 9) show dense microstructure due to a sufficiently high process T to homogeneously melt the particles and the higher velocity to impact the pre-deposited splats (see Figure 6.4(b) and (c)). It is more common to see splashed fingers in the splats with bright contrast edges with increasing H_2 ratio. Due to the rapid quenching, there many exists amorphous or nano-sized crystallites at the edge and splashed fingers of splats with a higher electron density which makes brighter contrast than in the center regime which contains void spaces such as microcracks and nanoporous foams [179]. Especially, coating Cas-0 contains bright nano-scale dots within the splat matrix (mostly periphery), as clearly shown in the enlarged micrograph (Figure 6.4(e)). These bright dots might be the conducting Magnéli phases (n=5 and 6) with small crystallite sizes that are detected by XRD (see the Section 6.2). The images of splat and coating cross section processed via HVOF are also presented in Figure 6.4(d). The residential time in the flame is not enough to generate a molten state of the particles due to the low thermal and high kinetic energies. Unmolten splashed splats are generated once the particles reached the substrate with high impact energy. Although this condition produced "unmelts", dense microstructure is accomplished in the coating by high impact energy that enhances the adhesion strength of the coating.

6.4 Thermoelectric Transport Properties (Seebeck Coefficient and Electrical Conductivities)

Seebeck coefficients (S) of substoichiometric TiO_{2-x} coatings are calculated by measuring thermoelectric voltages with varying thermal gradients along the coatings. S values at the hot side temperature (T_{HOT}) of 750 K are displayed in Figure 6.5(a) (dashed bars) in the order of high to low *S*. The coatings produced without using hydrogen in the plasma and HVOF show large *S*, 225 – 250 μV K^{-1}, due to containing more Rutile phase. For coatings produced with hydrogen-containing plasma, as the thermal exposure increases, the Seebeck coeffincient is decreased from 150 μV K^{-1} to 80 μV K^{-1}, due to increasing the more electrically-conductive reduced Magnéli phase (Ti_4O_7) content while the Rutile content is constant. Thus, the values of the Seebeck coefficient are significantly affected by the amount of Rutile content and then affected by reduced phase contents in the coatings if the Rutile is constant. The correlation between phase contents and *S* is apparent by comparing process-dependent phase contents and *S* plots shown in Figure 6.3 and 6.6(a).

Temperature dependent electrical conductivity of the substoichiometric TiO_{2-x} coatings is measured from room *T* to 750 K. All coatings show semiconducting behavior from room *T* to ~650 K but a semiconductor to metal-like transition occurs at between 650 – 750 K (580 K for Conv-0) due to the crystallographic distortion of Magnéli phases attributed to a change of the lattice parameters [117,180-181]. The electrical conductivities of the resultant coatings show more than a factor of 20 differences at 750 K which indicates that the electrical transport is strongly affected by the thermal spray process and the consequent phase changes. Figure 6.5(a) (dotted bars) shows the electrical conductivities of the coatings at 750 K which increase with increasing hydrogen content in the plasma, with a corresponding reduction of Seebeck coefficient. This interrelated *S* and σ behavior is well correlated with the behavior of conventional 3D TE materials. However, the *S* and σ values of coatings Cas-0 and HVOF behave somewhat independently, showing higher electrical conductivity without further reduction of *S.* Meanwhile, the σ of coating Conv-0, which has similar phase contents and Seebeck coefficient to that of coating Cas-0, shows the lowest value. In addition, the hydrogen-processed coatings Conv-4 and 12 and Cas-3 and 9 contain more reduced Magnéli phases (Ti_4O_7-(not for coating Cas-3), Ti_5O_9 and Ti_6O_{11}), which results in a higher concentration of transport carriers (oxygen deficiency) and exhibit even lower electrical conductivities. Figure 6.6(b) shows the temperature dependent electrical conductivities as a function of thermal exposure, which may indicate an unusually high σ for coatings Cas-0 and HVOF despite their phase contents, as well as their higher porosity compared to coatings Cas-3 and 9. The only remarkable difference between the coatings Cas-0 and HVOF and the others is the microstructures of splats and coatings (see Figure 6.2). Splats of coatings Conv-0, 4, 12 contain "unmelts" on the core area of the splats due to the inhomogeneous melting by the unstable arc that causes voids and imperfections in the successive impingements in the coating microstructure. Also, some splats of coatings Conv-4 and 12 shows splashed fingers generated by the molten surface of the particles and voids produced at the periphery of the splats. These imperfections raise electron scattering that interrupts the transport of carriers. The splats of the coatings Cas-3 and 9 show a fully molten state with high density. However, void spaces at the center as well as the edges of splats are detected due to the high impact which causes too much splashing. Also, the splashed particles cause the globular and interlamellar pores by making the next deposit bend. The bend interfaces are easily seen in the cross-section of these coatings. These factors together impede electron transport, although the coatings consisted of electrically-conductive reduced Magnéli phases. In contrast, the microstructure of splats Cas-0 shows a fully-molten pancake-like structure without any voids in the center. Moreover, the brighter nano-scale dots at the periphery regime of splats might provide an electrical transport channel, similar to that of a brick-layer model, to enhance the electrical conductivity [109] despite the small reduced

Magnéli phases' contents. For the coating HVOF, dense microstructure with higher adhesion might provide better electron transfer paths.

6.5 Thermal Conductivity

Figure 6.5(b) shows the temperature dependent thermal conductivity (k_{tot}) of the substoichiometric TiO_{2-x} coatings from room T to 750 K. All coatings show lower values of thermal conductivity, ~1.27 – 2.31 W m^{-1} K^{-1}, compared to the values for Rutile single crystals, ~ 6 – 8 W m^{-1} K^{-1} [182], due to the microstructure of the thermal sprayed coatings containing imperfections such as pores and microcracks. Figure 6.6(c) shows the temperature dependent thermal conductivity as a function of thermal exposure, which shows that the phase contents, both microstructure (porosity) and electrical conductivity of coatings affect the thermal conductivity. Particularly, coatings HVOF and Cas-0 shows the lowest thermal transport values even if they have shown high electrical conductivity over the temperature range, which is contrary to the Wiedemann–Franz law. Since coating HVOF contains unmolten building blocks, the microstructure conserves the grain boundaries from the powder state which would scatter phonons. However, the reason is still unclear why coating Cas-0 shows low thermal conductivity despite its high electrical conductivity, as well as good microstructure with fully-molten splats that could provide better thermal energy transport. Thus, this unusual phenomenon supports the possibility of the existence of low dimensional Magnéli phases at the peripheries of splats which could be produced by rapid quenching from the bottom surface of splats in this particular spray condition. Meanwhile, electrical and thermal transports obey the Wiedemann–Franz law for the coatings Conv-0, 4, and 12 and Cas-3 and 9 with porosity compensation.

Contribution of the lattice thermal conductivity (k_l) is calculated using $k_l = k_{tot} - L\sigma T$. The Lorenz number ($L$) used for obtaining k_l is 2.6 x 10^{-8} V^2 K^{-2} which is the reported value of $TiO_{1.4}$ [77]. Figure 6.5(c) shows the lattice contribution over the total thermal conductivity (k_l / k_{tot}) which indicates that 94% of the thermal energies are transported via phonons in these coating systems. It is discovered that thermal conductivities above 650 K are increased for the most of coatings (except coating Cas-9), even though the electrical conductivity stays constant or decreases above 650 K. This implies that the absolute values of k_l are increased at 750 K due to more sintered Rutile phase which might be generated by the oxygen recovery process from 723 K [110], which reduces the phonon scattering.

6.6 Power Factor and Figure of Merit

The power factors, *PF*, as a function of the thermal exposure of the coatings are shown in Figure 6.7(a). The highest value of 2.83 μW cm^{-1} K^{-2} is obtained at 750 K from the coating Cas-0 due to its high σ without a reduction in *S*. Interestingly, the *PF* of Conv-0 and Cas-0 conditions shows a difference of about a factor of 20 at 750 K due to its lowest electrical conductivity, which indicates that the TE properties of TiO_{2-x} coatings are very sensitive to the process conditions. Finally, values of the figure of merit, *ZT*, for thermally sprayed substoichiometric TiO_{2-x} coatings are given in Figure 6.7(b). The highest *ZT*, 0.13, is obtained at 750 K from the coating Cas-0 by breaking the interrelationship of *S*, σ, *and* k_{tot}. The value of *ZT* obtained is in the similar range with that reported for hot pressed substoichiometric TiO_{2-x} samples [119] despite their lower *PF*, which indicates that the thermal spray process is a competitive method to produce low thermal conductivity material. The coating HVOF also shows a promising result, with a *ZT* value of 0.077 at 750 K due to its low thermal conductivity, accomplished by a large phonon scattering brought about by the unmolten microstructure. The coating Conv-0 shows slightly higher *ZT* values compared to those of hydrogen-containing-plasma coatings because of its high *S*. For the hydrogen-containing-plasma coatings, *ZT* values increase with increasing thermal exposure. These coatings are likely to be governed more by the electrical conductivity rather than the Seebeck coefficient.

6.7 Process Effects on Microstructure-Phase-Thermoelectric Properties of $TiO_{1.7}$ Coatings

Substoichiometric TiO_{2-x} coatings were synthesized by the same thermal spray processes with feedstock starting stoichiometry of $TiO_{1.7}$. Since the particle sizes of the $TiO_{1.7}$ powder are bigger (coarse) than that of the previously used $TiO_{1.9}$ powder, the process conditions are shifted to a lower *v* regime on the *T*-*v* map compared to those used for $TiO_{1.9}$, while the *T* remained same. Thus, the particles experienced more thermal exposure due to the longer residential time in the plasma/flame during the excursions. Phase content of the feedstock and the as-sprayed coatings were investigated by XRD with Rietveld analysis. The patterns of $TiO_{1.7}$ feedstock and coatings are presented in Figure 6.8 and 6.9. The original feedstock consisted of Magnéli phases (n = 3 – 6, a majority of Ti_3O_5 and Ti_4O_7) and the calculated stoichiometry is $TiO_{1.703}$, which also matches well with the data provided by the powder manufacturer. The phases of all coatings prepared with $TiO_{1.7}$ are completely converted to Rutile and Ti_8O_{15} phases by oxidation during the process. The amount of oxidized phases is sensitively affected by the thermal exposure and hydrogen content of the plasma. The coatings HVOF and Conv-0 retain the most reduced Ti_3O_5 phase due to the minimal thermal exposure. With further thermal exposure, the Ti_3O_5 phase is completely transformed to the higher number Magnéli (n = 4 and 8) and Rutile phases. However, with an increase of the content hydrogen of the plasma, the reducing environment limits the further oxidation and provides more Ti_4O_7 phase in the coatings Conv-12 and Cas-9. Hence, the stoichiometry of the coatings was calculated and increased from $TiO_{1.805}$ to $TiO_{1.932}$, which implies the oxidation of the original feedstock. Microstructures of splats and coatings were investigated and porosity of the coatings was also calculated, as in the above section. A similar trend of porosity versus thermal and kinetic energies of particles is obtained, with a range of 2.8 – 10.9 %, due to the inhomogeneous melting brought about by the coarse sizes of the particles (see Figure 6.10). However, splat HVOF shows a better molten state compared to that of $TiO_{1.9}$ used because of the longer thermal exposure (see Figure 6.10(d)) and coatings made with hydrogen show much higher density (see Figure 6.10(f)) than the coatings made without using hydrogen. Thus, providing higher thermal energy by including a H_2 gas content plays important role in developing desirable microstructure for these coarse-sized particles. The values of Seebeck coefficient and electrical conductivities of the $TiO_{1.7}$-used coatings vary in ranges of 90 – 210 $\mu V\ K^{-1}$ and 900 – 15400 $S\ m^{-1}$ at T_{HOT} = 750 K, respectively, which are a lower range of S and a higher range of σ than those of the $TiO_{1.9}$-used coatings due to their phase contents (see Figure 6.11(a)). However, the S and σ of $TiO_{1.7}$-used coatings are interrelated each other, thus the highest power factor, PF, of 1.62 $\mu W\ cm^{-1}\ K^{-2}$ at 650 K is obtained from the coating Conv.-0 (see Figure 6.7(c)). Temperature dependent thermal conductivities of these coatings were also measured and a lower range of k_{tot}, 0.88 – 2.33 $W\ m^{-1}\ K^{-1}$, was obtained due to their higher porosity (see Figure 6.11(b)). Because of the higher electrical conductivity of these coatings, more electrical contribution, up to 18 %, is involved in the thermal transport (see Figure 6.11(c)). Thus, the trend of thermal conductivities of the coatings is well described by the Wiedemann–

Franz law. Indeed, the substoichiometric TiO_{2-x} coatings that were processed with the coarse $TiO_{1.7}$ powder show interrelated behaviors of thermoelectric variables, which indicate that conventional 3D TiO_{2-x} coatings are produced. The highest figure of merit, *ZT*, value among the $TiO_{1.7}$-used coatings is 0.10 at 650 K from the coating Conv-0 by optimization of the carrier concentration through the spray process (see Figure 6.7(d)). In addition, the coating HVOF shows a promising result of *ZT* values 0.085 at 650 K.

6.8 Conclusions

The thermoelectric properties of substoichiometric TiO_{2-x} coatings produced by the thermal spray process were investigated from room temperature to 750 K. Various stoichiometries of TiO_{2-x} coatings ($0.068 \leq x \leq 0.195$) with high density are obtained by changing the thermal and kinetic energies of plasma/flame during the process. The particles experience reduction/oxidation during the excursion, thus, phase decomposition occurs and produces a mixture of Magnéli (Ti_nO_{2n-1}, n = 3 – 9) and Rutile phases in the coatings. Significant enhancement of the electrical conductivity from 2.30×10^2 S m^{-1} to 1.74×10^4 S m^{-1} at 650 K, as well as a corresponding reduction in the Seebeck coefficient from 270 μV K^{-1} to 73 μV K^{-1} were observed depending on the spray parameters. Surprisingly, one coating produced by the cascaded plasma torch without hydrogen, shows a high Seebeck coefficient without reducing the electrical conductivity, due to a relatively higher Rutile content with a superior microstructure, which yields a power factor of 2.85 μW cm^{-1} K^{-2} at 750 K. In addition, lower thermal conductivity, 1.36 W m^{-1} K^{-1} at 650 K, is attained for this coating, which indicates that the thermoelectric terms of this coating behave independently. Thus, the largest *ZT* of 0.13 is obtained from the coating at 750 K.

7. Synthesis

LSM, MCO and TiO_{2-x} coatings were deposited with different spray parametric conditions by deliberately changing hydrogen ratio, mass flow rate, arc power, and hardware in order to vary the thermal excursion of the particles. The particle temperature and velocity were monitored in situ and their physical (phase, stoichiometry, and microstructure) and functional (electrical/thermal conductivities, oxide scale protections, Seebeck coefficient) properties were analyzed based upon how much the thermal exposure is experienced by the particles, $T \times v$, during each process.

As the first test bath for investigating applicability of thermal spray process for the functional oxide coatings, LSM and MCO coatings were prepared by air plasma spray process in order to provide cathode protection from the oxide scales generated from metallic interconnect. The prerequisites of the protection layer are providing protection performance from oxide scale growth toward the triple phase boundary with a reasonably high electrical conductance. The coatings generated with high T and low v on the 1st order process map indicating more thermal exposure with longer residential time in the plume showed more preferential elemental losses such as oxygen and manganese in LSM and MCO coatings which brought secondary phases or trapped distorted lattices. In contrast, the low T and high v used conditions such as condition E retained more original phase and stoichiometry within the coatings. However, coating E contains unmolten particles that cause porosity in the microstructure. Also, low v conditions A and C showed a tendency to generate microcracks in their microstructure due to the larger tensile quenching stresses. Meanwhile, the high T and v used condition B produced the highest density in LSM and MCO coatings. Despite the high porosity in the microstructure of condition E, the electrical conductivities of LSM and MCO coatings were obtained the highest, 55 and 40 S cm^{-1} at 800 °C, respectively, compared to the other four *T* and *v* used coatings due to the better phase retention. Protection against the oxide scale growth also was assessed by heat treatment at 800 °C for 600 h. The cross-sectional EDX atomic profiles displayed that the LSM coatings except for coating A showed 70 % better protection performance compared to the bare ferritic steel interconnect. However, coating A showed enhanced oxide scale growth rate due to the secondary phase, La_2O_3, which is known as hygroscopic material by pulling the oxides with retaining moisture in the LSM layer. For the MCO coatings, oxide scale were barely grown, ~1 μm, after the heat treatment but the cross-sectional atomic profiles of coatings A and C showed a large deviation of oxide scale because the oxide scales were grown through the microcracks in the coatings. Thus, the LSM coatings B-E and MCO coatings B, D, and E were shown superb protection performance compared to the interconnect without any protection even though they contain a certain amount of porosity. Overall, condition E, high v with He gas exhibited the best functional performance for the both LSM and MCO coatings by satisfying the all prerequisites for the functional requirements which imply the thermal spray process could successfully produce the cathode protection layer in SOFCs by optimizing the spray parametric variables.

As the second test bath, TiO_{2-x} coatings were produced to demonstrate the capability of thermal spray process for fabricating thermoelectric generator. Magnéli titania (Ti_nO_{2n-1}) was selected as our starting materials for aiming at n-type semiconductor due to their high electrical conductivity, thermal/chemical stability up to 500 °C, cost effective, earth-abundance, non-toxicity, good flowability and commercial availability. The seven different thermal excursion applied coatings were produced by consciously control hydrogen ratio, hardware, and thermal spray techniques. All coatings produced with starting stoichiometry of $TiO_{1.7}$ experienced process induced phase oxidation and showed conventional 3D thermoelectric properties, i.e. high S with increasing oxidized contents in the coating with reduction of σ and k_{tot}. Thus, the highest ZT value of 0.10 at 650 K is obtained by the optimization of the thermoelectric variables from condition Conv-0. However, the coatings prepared from the stoichiometry of $TiO_{1.9}$ displayed all reduced phases during the spray process except for the non-hydrogen used conditions. The non-hydrogen used conditions contained twice more Rutile phase in the coating but the total stoichiometry of coating still showed similar to the starting stoichiometry due to generation of reduced phases of Magnéli. All coatings also followed conventional 3D thermoelectric trend by showing interdependence of variables, but coating produced by cascaded plasma gun with non-hydrogen (condition Cas-0) exhibited independent behaviors with high S without reduction of σ as well as low k_{tot}. Containing low dimensionality such as nano-scale crystallites within the coating might be attributed to the peculiar behavior, hence, the value of ZT is obtained 0.13 at 750 °C which is the same value that has been reported from previous research produced by hot press. This result makes thermal spray process as a competitive method for thermoelectric generator fabrication.

8. Suggestions for future work

8.1 Possible p-type, n-type semiconducting materials for thermoelectric modules

In Chapter 6, we demonstrated the capability to use thermal spray processes to fabricate thermoelectric devices using n-type TiO_{2-x} materials. In order to build a complete thermoelectric generator (TEG), finding a good p-type material, which could be sprayable, is crucial to accomplish the goal of this project. Since we had available stocks of $LiNi_{0.8}Co_{0.15}Al_{0.05}O_2$ [183], Li-doped (various %) CoO [184] and NiCrCoAlY-Al_2O_3 [185] nanocomposites, which are known as p-type semiconductors, they were sprayed through the mask that had been used for TiO_{2-x} coatings in order to preliminary demonstrate the applicability. Due to the limited powder quantity, only one spray condition was chosen, with parameters close to those that show the best thermoelectric performance of the TiO_{2-x} coating and the conditions for the p-type materials are presented in Table 8.1. As shown in Chapter 6, the thermoelectric properties are affected by stoichiometry and coatings mictrostructure, employing the use of XRD and SEM.

Figure 8.1(a) shows the XRD patterns of $LiNi_{0.8}Co_{0.15}Al_{0.05}O_2$ (LNCAO) feedstock and as-sprayed coating. Additional reflections are noted at 2 theta ~ 30, 32, 34, 43, 57, 63 and 76 deg in the XRD patterns of coating that indicate the possibility of phase decomposition or metastable phase entrapment during the spray process. Thus, post annealing processes were attempted at 300, 500 and 700 °C, respectively, for 2 hours in air in order to recover the original phase. As a result of the post-annealing process, the phase composition of the coating was recovered after 700 °C annealing. However, the microstructure of the annealed coating contains perpendicular cracks that could possibly cause delamination of the top part of the coating (see Figure 8.1 (b)). These catastrophic perpendicular cracks are propagated from the low density region (Figure 8.1(c)) in the as-sprayed coating during the annealing process, and is attributed to the broad range of the particle size distribution (see Figure 8.1(d)). In order to improve the quality of the microstructure of the $LiNi_{0.8}Co_{0.15}Al_{0.05}O_2$ coatings, the size distribution of the particle must be narrower.

The Seebeck voltage of the annealed $LiNi_{0.8}Co_{0.15}Al_{0.05}O_2$ coating was measured by a generating thermal gradient along the coated line with successive thermal cycling from room T up to 400 – 900 K at 100 K intervals in order to see the repeatability and thermal stability. With the same measurement set-up of TiO_{2-x} coating, an opposite sign of voltage is generated which indicates different type of carriers in this coating (p-type). The Seebeck coefficient is -170 μV at 750 K, and the temperature dependent S is shown in Figure 8.2. Thermal hysteresis is shown between heating and cooling due to the inaccurate temperature measurement while the heat source (hand torch) is directly touching the hot side of substrate. However, after removing the heat source (cooling down), the Seebeck curves of the successive thermal cyclings followed same line. Thus, the $LiNi_{0.8}Co_{0.15}Al_{0.05}O_2$ is a promising candidate as the p-type pair with n-type TiO_{2-x}.

Likewise, Li-doped Co_3O_4, a mixture of NiCoCrAlY/Al_2O_3 (80:20 wt%), and 95 wt.% In_2O_3 and 5 wt.% SnO_2 (ITO) were deposited through the line-shaped mask in order to test the thermoelectric property of thermally sprayed coatings. Due to the limited quantity of Li-doped Co_3O_4 (0.05, 0.5, 2, and 5 %) powders, a mixture of the various doping ratio Li-Co_3O_4 was deposited by the plasma spray process. XRD of feedstock and as-sprayed coating was measured, and like the MCO coatings in Chapter 5, Co_3O_4 spinel phase was decomposed to the rock salt CoO phase due to the rapid solidification of the plasma spray process (see Figure 8.3). Thus, post-annealing process was tried at 700 °C for 2 h, since we know that the recovery starting temperature is 620 °C via the temperature dependent XRD study of MCO coatings. The XRD patterns of annealed Li-doped Co_3O_4 show the same patterns to those of feedstocks. The Seebeck voltage of annealed Li-doped Co_3O_4 coating was measured and the highest opposite-sign Seebeck coefficient of -608 μV/K at 750 K was obtained. However, the Seebeck coefficient from the NiCoCrAlY/Al_2O_3 coating was not shown any reasonable values due to the poor microstructure of the mixture. The microstructure of the coating and composite is compared in Figure 8.4. In order to produce composite structure, the author recommends retrying the plasma spray process using fine-sized powders with fully melting and slow quenching to grow composite structure. Lastly, ITO was also successfully deposited using the plasma spray process without any phase decomposition (see Figure 8.5). In addition, an excellent thermally-stable value of the Seebeck coefficient, 65 μV/K, was obtained (see Figure 8.2). Since it shows the same sign as the S of TiO_{2-x}, ITO is a possible alternative n-type candidate for high T application above the TiO_{2-x} phase transition temperature (~ 500 °C).

A TEG is a multi-layer-structured device operating one side of the module continuously exposed to the high temperature. Thus, minimal mismatch of coefficients of thermal expansion (CTE) as well as a small range of CTE with respect to temperature are required for the robust performance. Thus, Li-doped Co_3O_4 is the most promising p-type candidate, pairing with n-type TiO_{2-x}, in terms of good CTE matches and high Seebeck coefficient. The CTE of the possible candidate materials are presented in Table 8.2 [155,183,186-188].

8.2 Off-diagonal thermoelectricity

As we have seen in the above, optimization of the carrier concentration in TE materials is the only way to obtain the highest thermoelectric performance for the conventional 3D materials due to the interdependence of the thermoelectric variables. As a part of the efforts to be free from these constraints, unconventional approaches such as introducing low dimensional systems have been tried. Recently, a new concept of transverse or off-diagonal TE effect was developed to enhance the TE performance via applying a thermal gradient through-thickness (*z* direction) while generating electricity in-plane (*x* direction) from tilted layered materials (see Figure 8.6).

With the above TE configuration, the thermoelectric voltage obtained by the Seebeck effect is given by

$$E = S_{xz} \times \nabla T \text{ when } 0° < \alpha < 90° \qquad (8.1)$$

$$\boldsymbol{S} = \begin{bmatrix} S_{xx} & S_{xy} & S_{xz} \\ S_{yx} & S_{yy} & S_{yz} \\ S_{zx} & S_{zy} & S_{zz} \end{bmatrix} = \begin{bmatrix} S_{ab}\cos^2\alpha & 0 & \frac{\sin 2\alpha}{2}(S_{ab} - S_c) \\ 0 & S_{ab} & 0 \\ \frac{\sin 2\alpha}{2}(S_{ab} - S_c) & 0 & S_{ab}\sin^2\alpha + S_c\cos^2\alpha \end{bmatrix} \qquad (8.2)$$

where $\boldsymbol{S}$ is the Seebeck tensor and ∇T is the temperature gradient. The Seebeck tensor depends on the tilt angle (α) and the values of crystallographic anisotropy, S_c and S_{ab} (thermopower of *c*-axis direction and *ab*-plane, respectively), with respect to the coordinates in Figure 8.6. Also, the generated thermoelectric voltage is affected by the size (*l*) of the heat irradiated zone, and the thickness of the tilted sample (*d*). Thus, the off-diagonal voltage output is given by

$$E = \frac{\sin 2\alpha}{2}(S_{ab} - S_c)\nabla T \frac{l}{d} \qquad (8.3)$$

where the S_{ab} and S_c depend on the electrical and thermal conductivities of the tilted materials A and B, and thickness of A and B, $S_{ab} = \frac{\sigma_A S_A + \rho\sigma_B S_B}{\sigma_A + \rho\sigma_B}$ and $S_c = \frac{S_A k_B + \rho S_B k_A}{\rho k_A + k_B}$, and $\rho = d_A/d_B$ [189-190]. Possible application areas of transverse thermoelectric generators range from power plants and aerospace for power generation, as well as fuel consumption sensors, to automated home heating/AC systems by mounting through the wall of windows.

In order to maximize the thermoelectric performance, finding two materials which provide a reasonably high anisotropic Seebeck coefficient difference is important. The transverse thermoelectric voltage output is calculated with respect to the tilted angle and thickness ratio with $\nabla T = 30°\mathrm{C}$ using the equations above for the two different material combinations; (1) A = metal, B = semiconductor ($S_A = 10^{-3}S_B$, $\sigma_A = 10^4\sigma_B$, $k_A = k_B$) and (2) A = p-type semiconductor, B = n-type semiconductor ($S_A = -S_B$, $\sigma_A = \sigma_B$, $k_A = k_B$). Figure 8.7(a) and (b) show the calculated voltage outputs obtained by inputting arbitrary numbers that follow the above relations of the two types of material combinations, respectively. As a result of the calculation, the choice of two different types of semiconductors vanish the anisotropic Seebeck coefficient difference. Thus, the combination of high Seebeck (low conductive semiconductors) and close to zero Seebeck (metals) materials would be ideal for this application. For example, Al-n-type Si combination generates maximum voltage output of 450 μV at α = 45 deg and ρ = 20 for absorbed power P = 1W [191]. Also, Takahashi *et al.* reported 250 mV generations with by inputting a temperature gradient of 90 °C through thickness of tilted $Bi_{0.5}Sb_{1.5}Te_3$/Ni tube with α = 35 deg and ρ = 1 [192].

Although the previous research has proved the benefits of the transverse thermoelectric power generation, it is challenging to fabricate the tilted multilayers for the commercial applications. The tilted multilayers were prepared by stacking foils of A and B with desired thickness and sintering with pressure and then cutting the sintered stack obliquely to the stack axis. The CTSR has demonstrated fabricating a tilted structure by thermal spray process with premixing feedstocks A and B of desired ratio and spraying by tilting the plasma torch (see Figure 8.8) [193-194]. As preliminary work, splats various impact angles of 90, 60, and 45 deg were produced via HVOF with a mixture of LSM (Metco 6800) and TiO_2 powders (Metco 102) process, and their morphologies are examined by a zygo interferometer (see Figure 8.9). In the figure, the most impacted center shows a dip due to the splashing and the location of the dip is moved from the center of splat to the hill of the wedge by changing the torch angle from 90 to 45 degrees. These obserbed cross-sectional morphology profiles are well matched with the proposed illustration presented in Figure 8.8.

Coatings of the mixture of LSM (Metco 6800) and TiO_2 were produced with various torch angles (90, 60 and 45 degrees) and ratios of mixture (75:25, 50:50, and 25:75 v/v), and the electron micrographs of 45 deg of 50:50 mixture are shown in Figure 8.10. As seen in the cross-sectional electron micrographs, we successfully produced tilted multilayers by the thermal spray technique. In order to confirm the capability of the coating as a transverse thermoelectric generator, the thermoelectric voltage was measured by generating a thermal gradient through thickness. The design of the measurement set up is presented in Figure 8.11. Two heaters were employed to see the sign changes while changing the direction of the thermal gradient, as a proof of evidence for transverse voltage generation. Also, copper plates were placed between the two heaters to avoid generating in-plane thermal gradient. Then alumina plates were placed directly on the sample top and bottom sides to avoid electrical shorts. The transverse thermoelectric voltages of angled TiO_2, TiO_2-LSM mixture, and LSM lines were measured, and the results are displayed in Figure 8.12. As seen in the results, an in-plane voltage is generated via a thermal gradient through thickness and the sign is changed with changing the direction of thermal gradient. Since the LSM as the material has an almost zero Seebeck coefficient, the value of the generated voltage of the mixture is similar to that of TiO_2 which is well correlated to the results of the calculation. Thus, we have successfully fabricated a tilted multilayer structure via the thermal spray process for generating transverse thermoelectric voltage.

Even though the transverse Seebeck voltage generation is confirmed by the preliminary work, there are many things to be improved for the temperature measurement technique to accurately calculate the Seebeck coefficient of the tilted materials, as well as the material selection to improve the performance. Since the thermally sprayed coatings are an additive method to generate coatings, there are several deposit layers (insulating layer such as YSZ and TE material layer) on the substrate which makes it unable to measure the bottom temperature of the TE material directly. Thus, employing an imbedded thermocouple underneath of the insulating layer would solve the problem.

For generating high power output, reasonably high voltage and current are required. Thus, a high-Seebeck material, such as TiO_2, is in charge of generating voltage while the low Seebeck material is in charge of transporting carriers. Thus, finding a low Seebeck material with high electrical conductivity is crucial for this project. The author presents some suggested candidates in Table 8.3.

8.3 Magnetic measurement as a signature to study metallic particle oxidation in thermal spray

8.3.1 Introduction

Thermal sprayed (TS) nickel and nickel-based alloy coatings have been widely utilized in protective coatings and bond coats for ceramic topcoats due to their high wear and corrosion resistance, thermal efficiency, as well as superior adhesion. There has been aggressively investigated as one of the major applications of thermal spray process, thus, numerous studies were attempted based on searching for a relationship of thermal spray process-microstructure-functional properties of Ni based alloy coatings in order to optimize the process conditions that give the desired properties. Also, the process effect on functional properties in process map space provided systematic insights of the parametric effect on coating properties. One of the main reasons for the necessity of the optimization process is to control the oxide contents within the thermally sprayed coatings, which could affect the wear/corrosion resistance or thermal barrier system performance of the coatings. Thus, detecting oxide phase contents in the coatings with providing quantitative values is crucial to finding the optimized condition. In this part of dissertation, the author introduces electrical/magnetic measurements as a signature of metallic particle oxidation during the thermal spray process.

8.3.2 Experimental Methods

Ni, Ni-5wt%Al, and Ni-20wt%Cr were prepared using atmospheric plasma spray (APS) and high velocity oxy-fuel (HVOF). Stainless steel substrates (316 SS, 9`` L x 1`` W x 0.125`` H) were grit blasted under the pressure of 80 psi and carefully cleaned with alcohol to remove residual grits on the surface. A 300 micron of alumina was firstly applied on the 316 SS substrate as an electrical insulation layer prior to deposition of Ni and Ni-alloys for electrical conductivity measurement. The coating is then applied 100 µm thickness through a mask that has three different widths and lengths (0.050, 0.075 and 0.100 inches W x 0.50, 1.00 and 2.00 inches L) to confine the coating geometry.

The feedstock materials used in all coatings were alumina (#183, -45+15 µm, Microgrit), Ni (for APS, Metco 56C-NS, -75+45 µm, Oerlikon Metco, Westbury, NY, USA, for HVOF, NI-914-3, -45+16 µm, Praxair Surface Technologies, Inc., Indianapolis, IN, USA), Ni-5%Al (Metco 480NS, -90+45 µm for APS, Diamalloy 4008NS -45+11 µm for HVOF, Oerlikon Metco, Westbury, NY, USA), and Ni-20%Cr (Metco 43C-NS, -106+45 µm, Oerlikon Metco, Westbury, NY, USA). A design-of-experiment methodology was utilized to vary process conditions to achieve a range of thermal and kinetic energies and exposure. Coatings A through D (Table 8.4) were prepared using F4MB-XL plasma torch (Oerlikon Metco Inc., NY, USA) with an 8 mm diameter nozzle while varying with gas ratios and torch current. Coating E and F was also produced through an F4MB-XL torch but with a 6 mm effluent nozzle to achieve higher particle velocity. Coating G was deposited using a SG100 plasma torch (Praxair surface technologies, Indianapolis, IN, USA) with internal powder injection mode and with helium as the secondary gas. All A through G plasma sprayed coatings are prepared 100 mm plasma torch to substrate spray distance with 1000 mm/s raster speed. Coating H was prepared using both Woka Jet 4 (Oerlikon Metco Inc., NY, USA) and JP-5000 HP/HVOF system (Praxair surface technologies, Indianapolis, IN, USA) with 16’’ spray distance and 500 mm/s raster speed. Particle diagnostic sensors DPV2000 and Accuraspray (both from Tecnar Automation Lte., St. Bruno, QC, Canada) were used for F4MB-XL torch and JP-5000 HVOF system, respectively, and Spraywatch (Oseir Ltd., Tampere, Finland) were utilized for SG100 torch to obtain in-flight particle temperature, *T*, and velocity, *v,* in the thermal spray stream. The output of the diagnostics results were represented in a *T-v* map referred to as a first order process map as shown in Figure 8.6.

Cross-sectional microstructure of Ni, Ni-5%Al and Ni-20%Cr coatings was examined through scanning electron microscopy (SEM) (TM3000 Tabletop Microscope, Hitachi, Japan). Coatings were sectioned and fixed in epoxy mold and carefully polished. The phase structure of each feedstock powder and as-sprayed A through H coatings were investigated by powder x-ray diffractometer (XRD) (Phillips, 40 kV and 30 mA, Cu Kα source). Four-point probe electrical conductivity of the geometry confined coatings was measured at room temperature. Four Au wires (0.1 mm diameter, 99.95%, Alfa Aesar, Ward Hill, MA01835, USA) were contacted with Ag paste (Ted Pella, Inc. Redding, CA, USA). The four-probe wires were directly connected to 7700 module of Keithley 2700 digital multimeter. Magnetic hysteresis loops of feedstocks, as-sprayed coatings were obtained using vibrating sample magnetometer (VSM) (Model 880, Digital Measurement Systems, Microsense, LLC. Lowell, MA, USA). Free-standing Ni and Ni-alloy specimens for VSM were prepared by polishing off the substrate layer and mounted on high purity quartz rod using Teflon tape. Saturated magnetization (M_s) values of each coating were calculated by an extrapolation method due to the lack of saturation plateau.

8.3.3 Results and Discussion

Coatings of Ni, Ni-5%Al and Ni-20%Cr were prepared by using both air plasma and high-velocity oxy fuel sprays (APS and HVOF) techniques with controlling spray parameters in terms of gas contents, mass flow rate, power, size of particles and hardware. (see Table 8.4) The several parametric variables are mapped on 2-dimensional particle temperature (*T)* and velocity (*v)* axis (called 1st order process map) by in situ diagnosing particle T and v during the process. Examination of process-properties relationship using the process map for this type of coating materials is important because thermal spray processes are non-equilibrium process that evolves pores, cracks, interfaces, and trapped phases. Figure 8.13(a) – (c) show the 1st order process map of Ni, Ni-5%Al, and Ni-20%Cr coatings, respectively, and the range of temperature and velocity shows similar to each material within the same technique and hardware. However, temperature range of alloys shows higher range than that of pure Ni because of exotherm via preferential oxidation of Al or Cr. Also, the small variation of *T* and *v* is shown due to the difference of the size of particles; coarse Ni-20%Cr particles are located on lower *T* and lower *v* range compare to the fine particle size of Ni and Ni-5%Al. In addition, particle thermal energy increases with increasing hydrogen gas flow and applying higher current within the same hardware configuration. (see Figure 8.13 and Table 8.4) However, the particle thermal energy decreases with increasing kinetic energy when nozzle diameter is decreased in APS or switch the spray technique from APS to HVOF.

Cross-sectional microstructure of Ni, Ni-5%Al, and Ni-20%Cr coatings was investigated through SEM and their images are displayed at the corresponding location on the particle *T-v* map and shown in Figure 8.14, 8.15, and 8.16, respectively. Since A through D processed particles (APS F4 8mm nozzle) have no significant difference in the particle *v*, but show variations in particle temperature in the plasma, only thermal energy could be affected on their microstructure. The lowest temperature coating A contains both globular and interlamellar pores because of the unmolten particles. Particle temperature distribution via DPV-2000 diagnostic system shows some particles are located below the material’s melting point for this coating condition A. As increasing thermal energy of plasma from coatings B to D, interlamellar pores dominate with higher density. However, coating D shows dark phases around the interlamellar pores because of decomposition due to the high thermal energy. Within the similar temperature range, porosity and unmolten particles are increased as decreasing nozzle size (from 8 mm nozzle to 6 mm and SG100 gun's internal injection nozzle) due to short residential time in the plasma. Although HVOF process is lower *T* and shortest residential time process in the flame, the coating microstructure shows the highest density.

In-plane electrical conductivity of 100 µm thick Ni, Ni-5%Al, and Ni-20%Cr coatings was examined through four point probes method and their average values are plotted in Figure 8.17. The conductivity of Ni coatings looks closely related to the microstructure. As increasing coating density with increasing process *T* of coatings A through C, conductivity is also increased. As increased porosity of microstructure in short residential time APS coatings, conductivity is decreased but the highest density HVOF processed coating shows the highest electrical conductivity and the value is about 70 % of bulk Ni. However, alloy system shows different trend of electrical conductivity with pure Ni coating system. As increasing the process temperature of coatings A through D, electrical conductivity is increased. Particularly, coating D shows the higher conductivity than that of HVOF coating H despite higher porosity. This peculiar result could be attributed to selective oxidation of Al or Cr. Once Al or Cr is oxidized, there are more free Ni phases in the coating that enhances electrical conductivity. For the higher velocity 6mm nozzle APS and SG100, microstructure effect more dominates than phase due to less oxidation time. Thus, electrical conductivity of alloy system affects both microstructure and phase of coating. With rapid thermal quench, oxygen can form a metastable solid solution in Ni, Ni-5%Al, and maybe in NiCr. The oxygen impurity causes scattering of electron and high resistivity. It precipitates out as oxide in elusions at 400 ^{o}C and the resistivity decreases.

Magnetic hysteresis up and down to ± 1 T of Ni and Ni alloys coatings were measured by VSM and their saturated magnetic field (M_s) and % of coercivity are shown in figure 8.18 and 8.19, respectively. M_s of the pure Ni coatings shows almost same value to the original powder, but slightly lower M_s as increasing the process temperature with in the similar process velocity due to the formation of nickel oxide. However, coatings of Ni-5%Al and Ni-20%Cr alloys shows different trend with the pure Ni coatings and looks relying on the process. M_s value of feedstock powder of alloys is suppressed as increasing % of doping ratio of Al or Cr to Ni that is already expected from the magneto-phase diagram. After spraying process, alloy coatings show higher M_s than that of the feedstock powder due to the selective oxidation of Al or Cr which produces more pure Ni phase in the coatings. The amount of generated pure Ni increases with increasing process temperature because of more selective decomposition. However, coating D of NiCr shows lower M_s value than coating C because too much high process temperature causes not only selective Cr oxidation but also Ni oxidation that attributes to the lower magnetization.

Percent of coercivity (H_c) of Ni, Ni-5%Al and Ni-20%Cr coatings are calculated via the hysteresis curve of each coating versus the value of feedstock powder and the plots are shown in figure 8.19 with respect to the product of process temperature and dwell time to monitor the process effect on magnetic property. The % of coercivity of pure Ni coating shows no correlation to the process temperature and dwell time with scattering ranging from 25 % to 90%. Less decomposed coatings such as B, G and H are shown higher % of coercivity because of less NiO production. Also, the particle size of feedstock powder affects to the coercivity of coatings. Since the particle size of Ni and Ni-5%Al for HVOF is smaller than that for APS, so it shows highest coercivity.

8.3.4 Conclusions

We have examined the relationship among spray parameters, microstructure and electrical/magnetic properties of APS and HVOF sprayed Ni, Ni-5%Al and Ni-20%Cr coatings to relatively quantify oxide contents generation during the spray process. Since the thermal spray process generates imperfections in the coating microstructure and oxide second phase depending on the process parameters; as increasing process temperature and flight distance as well as decreasing particle velocity and size, Ni and Ni alloys particles are easily oxidized. In the case of Ni-5%Al and Ni-20%Cr, Al and Cr are preferentially oxidized that generates aluminum/chromium oxide second phases and free Ni phase. The free Ni phase increases their electrical conductivity and magnetic properties. However, too much high power condition (condition D) can also decompose nickel to nickel oxide that can lower saturated magnetic field and coercive field. The pure Ni coatings and alloys with too high processing energy generate nickel oxide phase that can lower the coating's electrical conductivity and magnetic field signals.

9. References

[1] Z. R. Dai, Z. W. Pan and Z. L. Wang, *Adv. Funct. Mater.* **13** (2003) 9-24.

[2] D. W. Bruce (Editor), D. O'Hare (Co-Editor), R. I. Walton (Co-Editor), Functional Oxides, John Wiley & Sons, Aug 9, 2010.

[3] S. Iwata and A. Ishizaka, *J. Appl. Phys.***79** (1996) 6653.

[4] A. I. Kingon, J.-P. Maria and S. K. Streiffer, *Nature* **406** (2000) 1032-1038.

[5] G. D. Wilk, R. M. Wallace and J. M. Anthony, *J. Appl. Phys.* **89** (2001) 5243.

[6] Y.-S. Lin, R. Puthenkovilakam and J. P. Chang, *J. Appl. Phys.* **81** (2002) 2041.

[7] G. D. Wilk, R. M. Wallace and J. M. Anthony, *J. Appl. Phys.* **87** (2000) 484.

[8] J. Robertson, The European Physical Journal Applied Physics. 28 (2004) 265-291.

[9] K. Nomura, H. Ohta, A. Takagi, T. Kamiya, M. Hirano and H. Hosono, *Nature* **432** (2004) 488-492.

[10] H. Kim, J. S. Horwitz, G. P. Kushto, Z. H. Kafafi and D. B. Chrisey, *Appl. Phys. Lett.* **79** (2001) 284.

[11] V. Dusastre and J.A. Kilner, *Solid State Ionics* **126** (1999) 163–174.

[12] J. M. Vohs and R. J. Gorte, *Adv. Mater.* **21** (2009) 943–956.

[13] J. F. Baumard andE. Tani, *physica status solidi (a)* **39** (1977) 373–382.

[14] S. Nishiuraa, S. Tanabea, K. Fujiokab and Y. Fujimoto, *Optical Materials* **33** (2011) 688–691.

[15] K-L. Choy, J. P. Feist, A. L. Heyes and B. Su, *J. Mater. Res.* **14** (1999) 3111–3114.

[16] X. Chen, Z. Mutasim, J. Price, J. P. Feist, A. L. Heyes and S. Seefeldt (2005). *Int. J. Appl. Cer. Techn.* **2** (2005) 414–421.

[17] J. G. Bednorz and K. A. Mueller, *Zeitschrift für Physik B*, **64** (1986) 189.

[18] T. Giamarchi, and S. Bhattacharya, *Lecture Notes in Physics*, **595** (2002) 314.

[19] C. Barry Carter, M. Grant Norton, (2007). Ceramic Materials: Science and Engineering. pp. 212–15, Springer.

[20] R. E. Hummel, (2005). Electronic Properties of Materials, Fourth Edition. Chapter 15, pp. 347-371, Springer New York.

[21] N. A. Spaldin, (2003) Magnetic Materials: Fundamentals and Applications, Second Ed. Chapter 9, pp. 113-129, Cambridge University Press.

[22] R. Naslain and F. Langlais, (1986) Tailoring Multiphase and Composite Ceramics (Ed. R. E. Tressler, G. L. Messing, C. G. Pantano, R. E. Newnham), pp. 145-164, Springer US.

[23] A. C. Tickle, Thin-Film Transistors - A New Approach to Microelec-tronics, Wiley, New York, 1969.

[24] E. Fortunato, P. Barquinha and R. Martins, *Adv. Mater.* **24** (2012) 2945-2986.

[25] J.R. Davis, editor, Introduction to Thermal Spray Processing, as published in Handbook of Thermal Spray Technology, p 3-13, ASM International and the Thermal Spray Society, 2004.

[26] H. Herman, S. Sampath and R. McCune, *MRS Bull.* **25** (2000) 17-25.

[27] S. Sampath, *J. Therm. Spray Techn.* **19** (2010) 921-949.

[28] S. Sampath, U. Schulz, M. O. Jarligo and S. Kuroda, *MRS Bull.* **37** (2012) 903-910.

[29] Y. P. Wan, S. Sampath, V. Prasad, R. Williamson and J. R. Fincke, *J. Mater. Process. Tech.* **137** (2003) 110-116.

[30] S. Sampath, *Int. J. Materials and Product Technology* **35** (2009) 425-448.

[31] J. R. Colmenares-Angulo, V. Cannillo, L. Lusvarghi, A. Sola and S. Sampath, *J. Mater. Sci.* **44** (2009) 2276-2287.

[32] K. Shinoda, S. Liang, S. Sampath and R. J. Gambino, *Mater. Sci. Eng. B* **176** (2011) 22-31.

[33] Q. Y. Yan, R. J. Gambino, S. Sampath and Q. Huang, *J. Appl. Phys.* **97** (2005) 033902.

[34] Q. Yan, R.J. Gambino, S. Sampath, L.H. Lewis, L. Li, E. Baumberger, A. Vaidya and H. Xiong, *Acta Mater.* **52** (2004) 3347-3353.

[35] Q.Y. Yan, R.J. Gambino and S. Sampath, *IEEE Trans. Magnetics* **40** (2004) 3346-3351.

[36] Q.Y. Yan, R.J. Gambino, E. Baumberger, L.H. Lewis and S. Sampath, *IEEE Trans. Magnetics* **40** (2004) 2787-2789.

[37] Q.Y. Yan, R.J. Gambino and S. Sampath, *IEEE Trans. Magnetics* **39** (2003) 3106-3108.

[38] Q.Y. Yan, R.J. Gambino and S. Sampath, *J. Appl. Phys.* **97** (2005) 10G102.

[39] N. Q. Minh, *J. Am. Ceram. Soc.* **76** (1993) 563–588.

[40] http://www.csa.com/discoveryguides/fuecel/overview.php

[41] P. Holtappels, U. Vogt and T. Graule , *Adv. Eng. Mater.* **7** (2005) 292-302.

[42] S. Hui, D. Yang, Z. Wang, S. Yick, C. Deces-Petit and W. Qu, *J. Power Sources* **167** (2007) 336.

[43] N. P. Brandon, A. Blake, D. Corcoran, D. Cumming, A. Duckett and K. El-Koury, *J. Fuel Cell Science and Technology* **1** (2004) 61.

[44] A. Das Sharma, J. Mukhopadhyay and R. N. Basu, *ECS Transactions* **35** (2011) 2509–2517.

[45] M. C. Tucker, G. Y. Lau, C. P. Jacobson, L. C. DeJonghe and S. J. Visco, *J. Power Sources* **171** (2007) 477.

[46] M. C. Tucker, G. Y. Lau, C. P. Jacobson, L. C. DeJonghe and S. J. Visco, *J. Power Sources* **175** (2008) 447.

[47] Y. B. Matus, L. C. De Jonghe, C. P. Jacobson and S. J. Visco, *Solid State Ionics* **176** (2005) 443.

[48] Z. Yang, G. Xia and J. W. Stevenson, *Electrochem. Solid St.* **8** (2005) A168–A170.

[49] J. P. Choi, K. S. Weil, Y. M. Chou, J. W. Stevenson and Z. G. Yang, *Int. J. Hydrogen Energ.* **36** (2011) 4549–4556.

[50] A. Kruk, M. Stygar and T. Brylewski, *J. Solid State Electr.* **17** (2013) 993–1003.

[51] X. Chen, P. Y. Hou, C. P. Jacobson, S. J. Visco and L. C. De Jonghe, *Solid State Ionics* **176** (2005) 425–433.

[52] M. R. Bateni, P. Wei, X. Deng and A. Petric, *Surf. Coat. Tech.* **201** (2007) 4677–4684.

[53] M. Lang, T. Franco, G. Schiller and N. Wagner, *J. Appl. Electrochem.* **32** (2002) 871.

[54] M. Lang, P. Szabo, Z. Ilhan, S. Cinque, T. Franco and G. Schiller, *J. Fuel Cell Science and Technology* **4** (2007) 384.

[55] G. Schiller, A. Ansar, M. Lang and O. Patz, *J. Appl. Electrochem.* **39** (2009) 293.

[56] M. J. Garcia-Vargas, M. Zahid, F. Tietz and A. Aslanides, *ECS Transactions* **7** (2007) 2399–2405.

[57] R. Vassen, D. Hathiramani, J. Mertens, V. A. C. Haanappel and I. C. Vinke, *Surf. Coat. Technol.* **202** (2007) 499.

[58] R. Vassen, H. Kassner, A. Stuke, F. Hauler, D. Hathiramani and D. Stoever, *Surf. Coat. Technol.* **202** (2008) 4432.

[59] H. Tannenberger and R. Schmitt, Swiss Patent No. 491 510, 31.

[60] H. Gruner and H. Tannenberger, US Patent 5, 328,779.

[61] H.R. Gruner and H. Tannenberger, SOFC Elements by Vacuum-Plasma-Spraying (VPS), Proceedings of 1st European Solid Oxide Fuel Cell Conference, Lucerne, Switzerland, Vol. 2, 1994, p 611-616 .

[62] M. Lang, R. Henne, S. Schaper and G. Schiller, *J. Therm. Spray Technol.* **10** (2001) 618-625.

[63] X. Q. Ma, S. Hui, H, Zhang, J. Dai, J. Roth, T. D. Xiao, D. E. Reisner, in: C. Moreau, B. Marple (Eds.), Thermal Spray: Advancing the Science & Applying the Technology, ASM International, Materials Park, Ohio, 2003, pp.163-168.

[64] X.Q. Ma, H. Zhang, J. Dai, J. Roth, R. Hui, T.D. Xiao and D.E. Reisner, *J. Therm. Spray Techn.* **14** (2005) 61-66.

[65] C. Hwang, C.-H. Tsai, C.-H. Lo and C.-H. Sun, *J. Power Sources* **180** (2008) 132–142.

[66] L. Jia, C. Dossou-Yovo, C. Gahlehrt, and F. Gitzhofer, Induction Plasma Spraying of Samarium Doped Ceria as Electrolyte for Solid Oxide Fuel Cells, Thermal Spray 2004: Advances in Technology and Application, ASM International (Osaka, Japan), May 10-12, 2004, p 85-89.

[67] W. Gao, H.-L. Liao and C. Coddet, *J. Power sources* **179** (2008) 739–744.

[68] A.A. Syed, Z. Ilhan, J. Arnold, G. Schiller and H. Weckmann, *J. Therm. Spray Techn.* **15** (2006) 617-622.

[69] C. Zhang, H.-L. Liao, W.-Y. Li, G. Zhang, C. Coddet, C.-J. Li, C.-X. Li and X.-J. Ning, *J. Therm. Spray Techn.* **15** (2006) 598-603.

[70] R. Rampon, F.-L. Toma, G. Bertrand and C. Coddet, *J. Therm. Spray Techn.* **15** (2006) 682-688.

[71] W. Qu, S. Yick, Z. Wang, R. Maric and D. Ghosh, *J. Therm. Spray Techn.* **17** (2008) 700-708.

[72] Y. Wang, J.-G. Legoux, R. Neagu, S. Hui and B.R. Marple, *J. Therm. Spray Techn.* **21** (2012) 7-15.

[73] M. Marr, J. Kuhn, C. Metcalfe, J. Harris and O. Kesler, *J. Power Sources* **245** (2014) 398-405.

[74] C.-J. Li, C.-X. Li and M. Wang, *Surf. Coat. Techn.* **198** (2005) 278-282.

[75] K. Barthel, S. Rambert and St. Siegmann, *J. Therm. Spray Techn.* **9** (2000) 343-347.

[76] B.D. White, O. Kesler and L. Rose, *J. Power Sources* **178** (2008) 334-343.

[77] G. S. Kumar, G. Prasad and R. O. Pohl, *J. Mater. Sci.* **28** (1993) 4261-4272.

[78] S. Walia, S. Balendhran, H. Nili, S. Zhuiykov, G. Rosengarten, Q. H. Wang, M. Bhaskaran, S. Sriram, M. S. Strano and K. Kalantar-zadeh, *Prog. Mater. Sci.* **58** (2013) 1443-1489.

[79] D. A. Wright, *Nature* **181** (1958) 834.

[80] C. Wood, *Rep. Prog. Phys.* **51** (1988) 459-539.

[81] J. L. Feldman, D. J. Singh, Mazin, II, D. Mandrus and B. C. Sales, *Phys. Rev. B.* **61** (2000) R9209-R9212.

[82] B. C. Sales, D. Mandrus and R. K. Williams, *Science* **272** (1996) 1625-1328.

[83] K. Koumoto, I. Terasaki and R. Funahashi, *MRS Bull.* **31** (2006) 206-210.

[84] I. Terasaki, Y. Sasago and K. Uchinokura, *Phys. Rev. B* **56** (1997) R12685-R12687.

[85] W. Shin and N. Murayama, *J. Mater. Res.* **15** (2000) 382- 386.

[86] R. Venkatasubramanian, E. Siivola, T. Colpitts and B. O'Quinn, *Nature* **413** (2011) 597-602.

[87] M. S. Gudiksen, L. J. Lauhon, J. Wang, D. C. Smith and C. M. Lieber, *Nature* **415** (2002) 617-620.

[88] M. S. Dresselhaus, G. Chen, M. Y. Tang, R. Yang, H. Yang, D. Wang, Z. Ren, J.-P. Fleurial and P. Gogna, *Adv. Mater.* **19** (2007) 1043-1053.

[89] G. J. Snyder and E. S. Toberer, *Nat. Mater.* **7** (2008) 105-114.

[90] G. Pernot, M. Stoffel, I. Savic, F. Pezzoli and P. Chen, *Nat. Mater.* **9** (2010) 491-495.

[91] L.-D. Zhao, S.-H. Lo, Y. Zhang, H. Sun, G. Tan, C. Uher, C. Wolverton, V. P. Dravid and M. G. Kanatzidis, *Nature* **508** (2014) 373-377.

[92] S. N. Girard, J. He, C. Li, S. Moses, G. Wang, C. Uher, V. P. Dravid and M. G. Kanatzidis, *Nano Lett.* **10** (2010) 2825-2831.

[93] S. N. Girard, J. He, X. Zhou, D. Shoemaker, C. M. Jaworski, C. Uher, V. P. Dravid, J. P. Heremans and M. G. Kanatzidis, *J. Am. Chem. Soc.* **133** (2011) 16588-16597.

[94] D. M. Rowe, V. S. Shukla, and N. Savvides, *Nature* **290** (1981) 765-766.

[95] C. B. Vining, W. Laskow, J. O. Hanson, R. R. Van der Beck and P. D. Gorsuch, *J. Appl. Phys.* **69** (1991) 4333-4340.

[96] Q. Li, Z. Lin and J. Zhou, *J. Electron. Mater.* **38** (2009) 1268-1272.

[97] H. Zhao, M. Pokharel, G. Zhu, S. Chen, K. Lukas, Q. Jie, C. Opeil, G. Chen and Z. Ren, *Appl. Phys. Lett.* **99** (2011) 163101.

[98] R. J. Mehta and G. Ramanath, *Am. Ceram. Soc. Bull.* **91** (2012) 28-33 (2012).

[99] U. Birkholz, E. Grob, U. Stohrer and K. Voss, Conversion of waste exhaust heat in automobile using $FeSi_2$ thermoelements. In Proceedings of the 7th International Conference on Thermoelectric Energy Conversion. K. R. Rao, ed, Arlington, USA. 1988. 124-128.

[100] H. Herman, S. Sampath and R. McCune, *MRS Bull.* **25** (2000) 17-25.

[101] S. Sampath, *J. Therm. Spray Techn.* **19** (2010) 921-949.

[102] J. P. Longtin, E. Mari, Y. Tan and S. Sampath, *J. Therm. Spray Techn.* **20** (2011) 958-966.

[103] J. P. Longtin, S. Sampath, R. J. Gambino, R. J. Greenlaw and J. Brogan, *Digital Fabrication* **2** (2006) 116-119.

[104] S. J. Han, Y. Chen and S. Sampath, J. *Power Sources* **259** (2014) 245-254.

[105] J. P. Longtin, L. Zuo, D. Hwang, G. Fu, M. Tewolde, Y. Chen and S. Sampath, *J. Therm. Spray Techn.* **22** (2013) 577-587.

[106] S. Sampath, U. Schulz, M. O. Jarligo and S. Kuroda, *MRS Bull.* **37** (2012) 903-910.

[107] G. Fu, L. Zuo, J. Longtin, C. Nie, Y. Chen, M. Tewolde and S. Sampath, *J. Electron. Mater.* **43** (2014) 2723-2730.

[108] G. Fu, L. Zuo, J. Longtin, C. Nie and R. Gambino, *J. Appl. Phys.* **114** (2013) 114905.

[109] S. Muthiah, J. Pulikkotil, A. K. Srivastava, A. Kumar, B. D. Pathak, A. Dhar and R. C. Budhani, *Appl. Phys. Lett.* **103** (2013) 053901.

[110] A. Sharma, A. Gouldstone, S. Sampath and R. J. Gambino, *J. Appl. Phys.* **100** (2006) 114906.

[111] L. Li, B. Kharas, H. Zhang and S. Sampath, *Mat. Sci. Eng. A* **456** (2007) 35-42.

[112] R. Funahashi, I. Matsubara, H. Ikuta, T. Takeuchi, U. Mizutani and S. Sodeoka, *Jpn. J. Appl. Phys.* **39** (2000) L1127-L1129.

[113] I. Matsubara, R. Funahashi, T. Takeuchi, S. Sodeoka, T. Shimizu and K. Ueno, *Appl. Phys. Lett.* **78** (2001) 3627-3629.

[114] W. Wunderlich, *Adv. Ceram. Sci. Eng.* **2** (2013) 9-15.

[115] F.-D. Börner, M. Schreier, B. Feng, W. Lippmann, H.-P. Martin, A. Michaelis and A. Hurtado, *J. Mater. Res.* **29** (2014) 1771-1780.

[116] W. R. Thurber and A. J. H. Mante, *Phys. Rev.* **139** (1965) A1655-A1665.

[117] R. F. Bartholomew and D. R. Frankl, *Phys. Rev.* **187** (1969) 828-233.

[118] J. F. Baumard and E. Tani, *Phys. Stat. Sol. (a)* **39** (1977) 373-382.

[119] V. Cristea and V. Babes, *Phys. Stat. Sol. (a)* **45** (1978) 617-624.

[120] A. D. Inglis, Y. Le Page, P. Strobel and C. M. Hurd, *J. Phys. C: Solid State Phys.* **16** (1983) 317-333.

[121] N. Okinaka and T. Akiyama, *Jap. J. Appl. Phys.* **45** (2006) 7009-7010 (2006).

[122] Y. Lu, M. Hirohashi and K. Sato, *Mater. Trans.* **47** (2006) 1449-1452 (2006).

[123] S. Harada, K. Tanaka and H. Inui, *J. Appl. Phys.* **108** (2010) 083703.

[124] C. Liu, L. Miao, D. Hu, R. Huang, C. A. J. Fisher, S. Tanemura and H. Gu, *Phys. Rev. B* **88** (2013) 205201.

[125] A. Sharma, R. J. Gambino and S. Sampath, *Mater. Res. Soc. Symp. Proc.* **890** (2006) 0890-Y09-11.1-11.6.

[126] M. Palcut, L. Mikkelsen, K. Neufeld, M. Chen and R. Knibbe, *Int. J. Hydrogen Energ.* **37** (2012) 8087–8094.

[127] K.Hilpert, D. Das, M. Miller, D. H. Peck and R. Wei, *J. Electrochem. Soc.* **143** (1996) 3642–3647.

[128] Y. Matsuzaki and I. Yasuda, *J. Electrochem. Soc.* **148** (2001) A126–A131.

[129] C. Collins, J. Lucas, T. L. Buchanan, M. Kopczyk, A. Kayani, P. E. Gannon, M. C. Deibert, R. J. Smith, D.-S. Choi and V. I. Gorokhovsky, *Surf. Coat. Tech.* **201** (2006) 4467–4470.

[130] S. Geng and J. Zhu, *J. Power Sources* **160** (2006) 1009-1016.

[131] A. Toji and T. Uehara, *ECS Transactions* **7** (2007) 2117-2124.

[132] J. Froitzheim, G. H. Meier, L. Niewolak, P. J. Ennis, H. Hattendorf, L. Singheiser and W. J. Quadakkers, *J. Power Sources* **178** (2008) 163-173.

[133] N. Shaigan, W. Qu, D. G. Ivey and W. Chen, *J. Power Sources* **195** (2010) 1529-1542.

[134] C. Gindorf, L. Singheiser, K. Hilpert, M. Schroeder, M. Martin, H. Greiner and F. Richter, *Electrochem. Soc. Proc.* **99-19** (1999) 774-782.

[135] S. Rambert, M. Kadowaki, H. Kawamura, T. Yasuo, Y. Akiyama, Y. Miyake and T. Saitoh, *J. Power Source* **55** (1995) 73-79.

[136] H. W. Nie, T.-L. Wen and H. Y. Tu, *Mater. Res. Bull.* **38** (2003) 1531-1536.

[137] Z. Yang, G.-G. Xia, G. D. Maupin and J. W. Stevenson, *Surf. Coat. Tech.* **201** (2006) 4476–4483.

[138] J.-H. Kim, R.-H. Song and S.-H. Hyun, *Solid State Ionics* **174** (2004) 185–191.

[139] C.-L. Chu, J. Lee, T.-H. Lee and Y.-N. Cheng, *Int. J. Hydrogen Energ.* **34** (2009) 422–434.

[140] M. Palcut, L. Mikkelsen, K. Neufeld, M. Chen and R. Knibbe, *Int. J. Hydrogen Energ.* **37** (2012) 8087–8094.

[141] S. J. Han, Y. Chen and S. Sampath, *J. Power Sources* **259** (2014) 245–254.

[142] E. O. Ahlgren and F. W. Poulsen, *Solid State Ionics* **86-88** (1996) 1173-1178.

[143] J. H. Kuo, H. U. Anderson and D. M. Sparlin, *J. Solid State Chem.* **87** (1990) 55-63.

[144] C. Zener, *Phys. Rev.* **81** (1951) 403-405.

[145] S. P. Jiang, *J. Mater. Sci.* **43** (2008) 6799-6833.

[146] J. Mizusaki, Y. Yonemura, H. Kamata, K. Ohyama, N. Mori, H. Takai, H. Tagawa, M. Dokiya, K. Naraya, T. Sasamoto, H. Inaba and T. Hashimoto, *Solid State Ionics* **132** (2000) 167-180.

[147] A. Hammouche, E. J. L. Schouler and M. Henault, *Solid State Ionics* **28-30** (1988) 1205-1207.

[148] M. Zhou, J. Yuan, W. Yuan, Y. Yin and X. Hong, *Nanotechnology* **18** (2007) 405704.

[149] C. Plato and A. R. Glasgow Jr., *Anal. Chem.* **41** (1969) 330-336.

[150] H. Kamata, Y. Yonemura, J. Mizusaki, H. Tagawa, K. Naraya and T. Sasamoto, *J. Phys. Chem. Solids* **56** (1995) 943-950.

[151] O. Kubaschewski and B. E. Hopkins, Oxidation of metals and alloys, 2 Ed, London Butterworths, (1967) 135-142, 236-237.

[152] L. Mikkelsen and S. Linderoth, *Mater. Sci. Eng. A* **361** (2003) 198-212.

[153] W. Qu, L. Jian, J. M. Hill and D. G. Ivey, *J. Power Sources* **153** (2006) 114-124.

[154] Y. S. Touloukian, R. K. Kirby, R. E. Taylor, and T. Y. R. Lee, Thermophysical Properties of Matter, IFI/Plenum, New York-Washington. Vol 13 (1970).

[155] A. Petric and H. Ling, *J. Am. Ceram. Soc.* **90** (2007) 1515-1520.

[156] H. Liu, X. Zhu, M. Cheng, Y. Cong, and W. Yang, *Int. J. Hydrogen Energ.* **38** (2013) 1052–1057.

[157] Y. Liu, J. W. Fergus and C. D. Cruz, *J. Am. Ceram. Soc.* **96** (2013) 1841–1846.

[158] D. G. Wickham and W. J. Croft, *J. Phys. Chem. Solids* **7** (1958) 351–360.

[159] I. Aoki, *J. Phys. Soc. Jpn.* **17** (1962) 53–61.

[160] H. Bordeneuve, S. Guillemet-Fritsch, A. Rousset, S.Schuurman and V. Poulain, J. *Solid State Chem.* **182** (2009) 396–401.

[161] J. Philip and T. R. N. Kutty, *Mater. Lett.* **39** (1999) 311–317.

[162] P.A. Joy and S.K. Date, *J. Magn. Magn. Mater.* **210** (2000) 31–34.

[163] G.V. Bazuev and A.V. Korolyov, *J. Magn. Magn. Mater.* **320** (2008) 2262–2268.

[164] K. Uusi-Esko, E.-L. Rautama, M. Laitinen, T. Sajavaara and M. Karppinen, *Chem. Mater.* **22** (2010) 6297–6300.

[165] J. Valencia, N.P. Arias, O. Giraldo and A. Rosales-Rivera, *Physica B* **407** (2012) 3155–3157.

[166] A. Restovic, E. Ríos, S. Barbato, J. Ortiz and J.L. Gautier, *J. Electroanal. Chem.* **522** (2002) 141–151.

[167] Y. Liang, H. Wang, J. Zhou, Y. Li, J. Wang, T. Regier and H. Dai, *J. Am. Chem. Soc.* **134** (2012) 3517–3523.

[168] H. Eba and K. Sakurai, *J Solid State Chem.* **178** (2005) 370–375.

[169] H. Bordeneuve, C. Tenailleau, S. Guillemet-Fritsch, R. Smith, E. Suard and A. Rousset, *Solid State Sci.* **12** (2010) 379–386.

[170] J. Chen, X. Wu and A. Selloni, *Phys. Rev. B* **83** (2011) 245204.

[171] A. Vaidya, V. Srinivasan, T. Streibl, M. Friis, W. Chi and S. Sampath, *Mat. Sci. Eng. A* **497** (2008) 239–253.

[172] F. J. Hermanek, D. Filippis, G. M. Herterick, H. Herman, C. C Berndt, S. Safai and E. R. Marantz, Coating Characteristics, In: M. L. Thorpe (Charman) Thermal Spraying-Practice, Theory, and Application, American Welding Society, Inc., Miami, 1985, pp. 29–48.

[173] S. Alleg, S. Souilah and J. J. Suñol, Thermal stability of the nanostructured powder mixtures prepared by mechanical alloying, In: A. A. Elkordy(Ed.), Applications of calorimetry in a wide context-differential scanning calorimetry, isothermal titration calorimetry and microcalorimetry, InTech Publisher, Vienna, 2013, pp. 21–48.

[174] S. Naka, M. Inagaki and T. Tanaka, *J. Mater. Sci.* **7** (1972) 441–444.

[175] S. Liang, B. G. Ravi, S. Sampath and R. Gambino, Material Research Society Symposium Procedings Vol. 900E 2006 0900-O06-41.1.

[176] R. Stoyanova, E. Zhecheva and L. Zarkova, *Solid State Ionics* **73** (1994) 233-240.

[177] S. Mirhashemihaghighi, B. León, C. Pérez Vicente, J. L. Tirado, R. Stoyanova, M. Yoncheva, E. Zhecheva, R. Saez Puche, E. M. Arroyo and J. Romero de Paz, *Inorg. Chem.* **51** (2012) 5554-5560.

[178] N. N. Greenwood and A. Earnshaw, Chemistry of the elements, Elsevier, 1998, p. 1118.

[179] M. Qu, Y. Wu, V. Srinivasan and A. Gouldstone, *Appl. Phys. Lett.* **90** (2007) 254101.

[180] M. Marezio, P. D. Dernier, D. B. McWhan and J. P. Remeika, *Mater. Res. Bull.* **5** (1970) 1015-1023.

[181] M. Marezio and P. D. Dernier, *J. Solid State Chem.* **3** (1971) 340-348.

[182] Thermophysical Properties of Matter, vol. 2 (eds Touloukian, Y. S. *et al.*) (IFI/Plenum, New York, 1970).

[183] W. Shin, N. Murayama, K. Ikeda, and S. Sago, *J. Power Sources* **103** (2001) 80-85.

[184] K. Koumoto and H. Yanagida, *Commun. Am. Ceram. Soc.* (1981) C-156–C-157.

[185] O. J. Gregory, E. Busch, G. C. Fralick and X. Chen, *Thin Soliöd Films* **518** (2010) 6093–6098.

[186] W. Z. Zhu and S. C. *Mater. Sci. Eng.* **A348** (2003) 227-243.

[187] Y.-G. Kim, J.-W. Ryu, J.-H. Song, K.-W. Lee, Y.-Y. Kim, D. Kim and B.-H. Cha, *J. Kor. Phys. Soc.* **49** (2006) 393-400.

[188] J. J. Liang, H. Wei, Y. L. Zhu, X. F. Sun, Z. Q. Hu, M. S. Dargusch and X. D. Yao, *J. Mater. Sci. Technol.* **27** (2011) 408-414.

[189] H. Lengfellner, S. Zeuner, W. Prettl and K. F. Renk, *Europhys. Lett.* **25** (1994) 375-378.

[190] T. Zahner, R. Förg and H. Lengfellner, *Appl. Phys. Lett.* **73** (1998) 1364-1366.

[191] *Appl. Phys. Lett.* **85** (2004) 5613-5615.

[192] K. Takahashi, T. Kanno, A. Sakai, H. Tamaki, H. Kusada and Y. Yamada, *Nat. Sci. Rep.* **3**:1501 (2013).

[193] G. Montavon, S. Sampath, C. C. Berndt, H. Herman and C. Coddet, *Surf. Coat. Techn.* **91** (1997) 107-115.

[194] G. Montavon, C. C. Berndt, C. Coddet, S. Sampath and H. Herman, *J. Therm. Spray. Techn.* **6** (1997) 153-166.

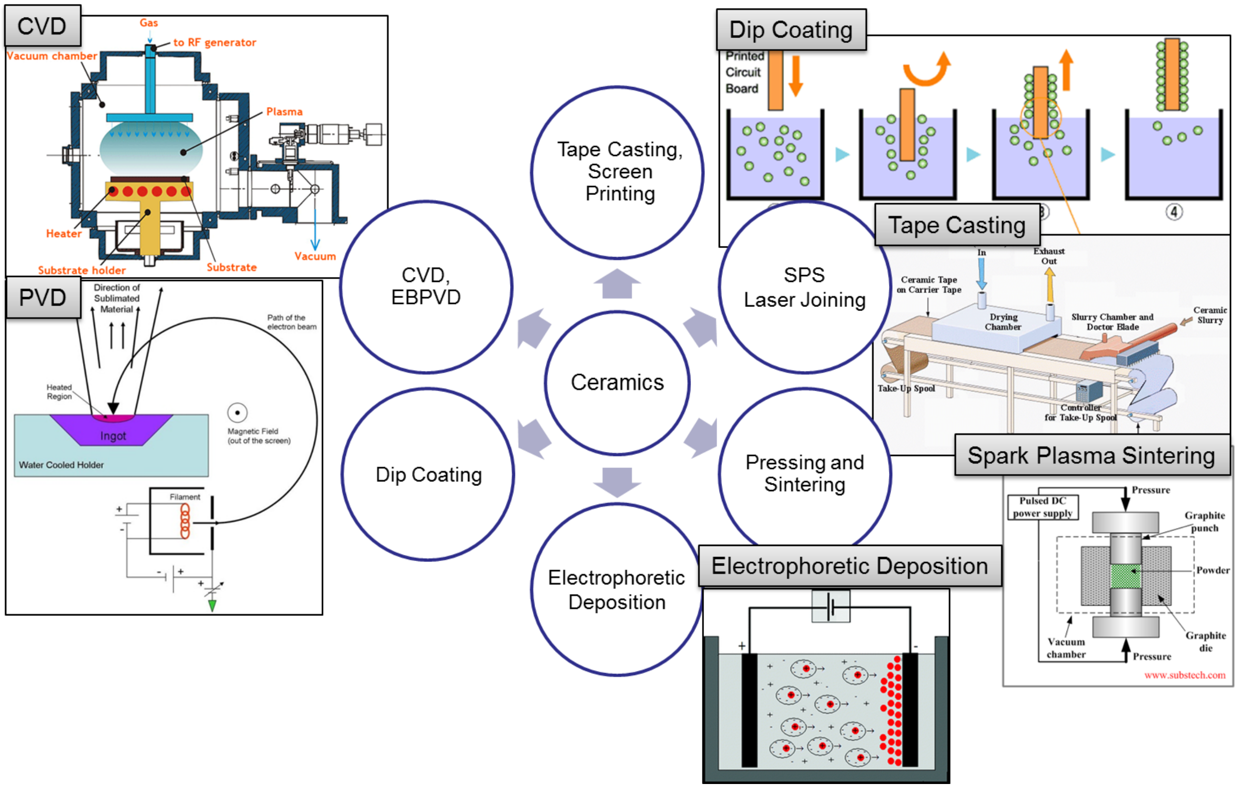

Scheme 1.1 Various processing methods for functional oxide materials.

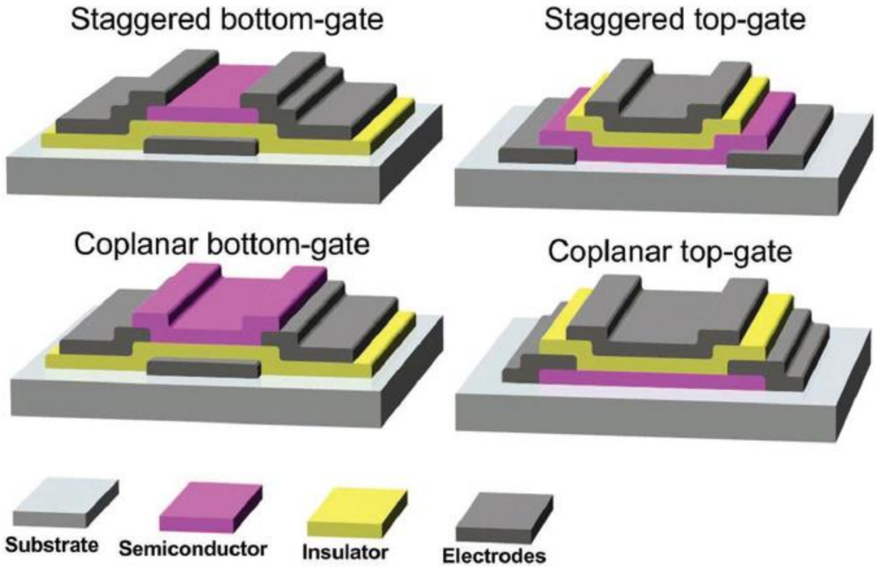

Scheme 1.2 Schematics showing some of the most conventional TFT structures, according to the position of the gate electrode and to the distribution of the electrodes relatively to the semiconductor.

(Courtesy of E. Fortunato, P. Barquinha and R. Martins, Adv. Mater. 24 (2012) 2945-2986.)

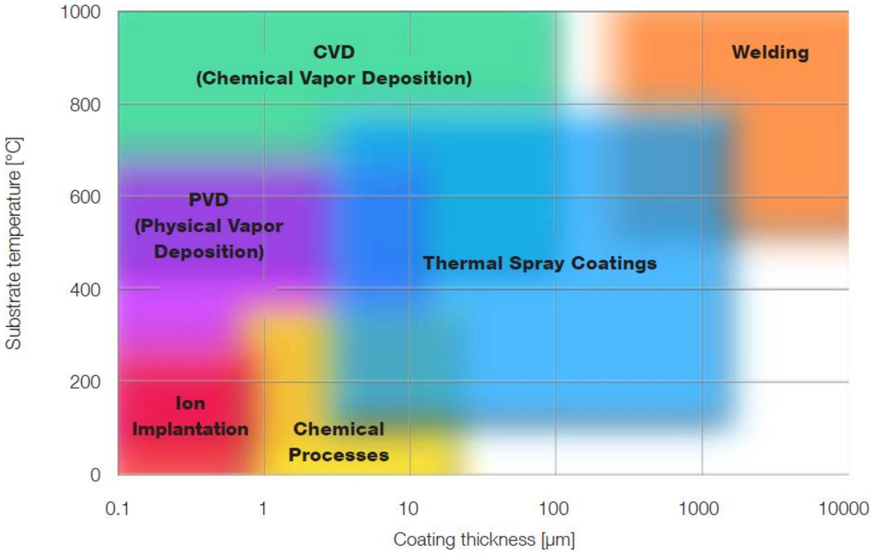

Scheme 1.3 Comparison of substrate temperature and coating thickness of coating deposition techniques. (Courtesy of Oerlikon Metco)

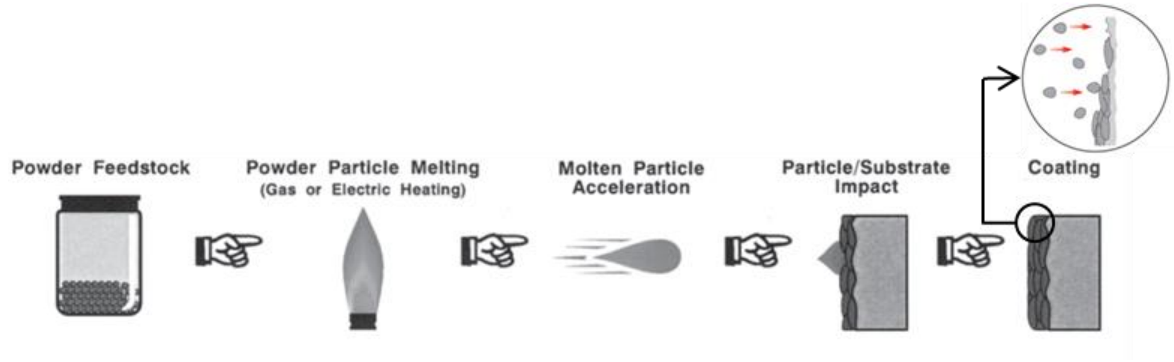

Scheme 1.4 Schematic illustration of thermal spray coating process. (Graphic courtesy of Westaim Ambeom)

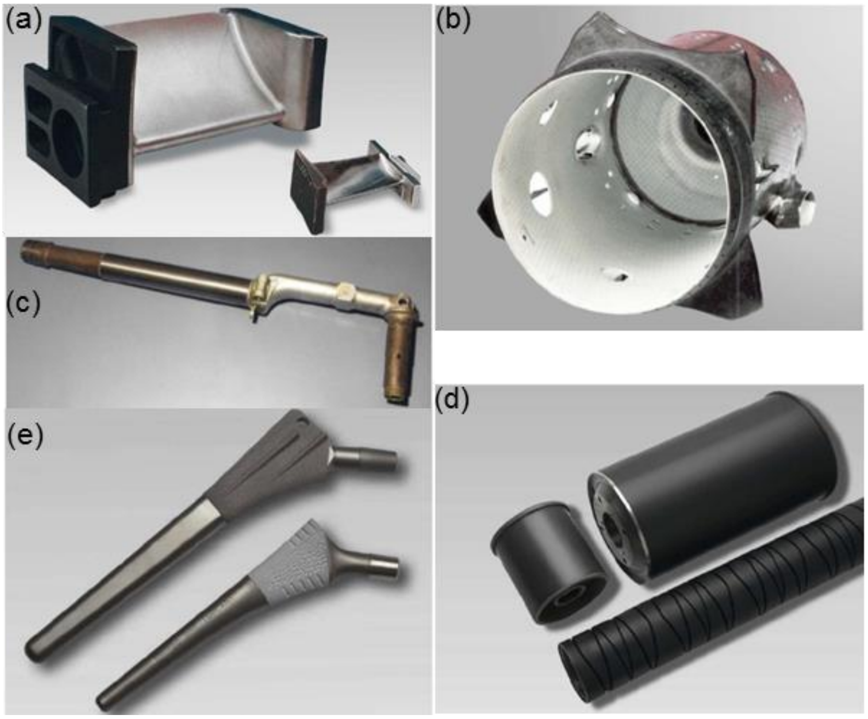

Scheme 1.5 Schematic illustration of opportunities of thermal spray coatings.
(a) Coated gas turbine vanes, (b) Combustion chamber, (c) Nose gear of a Tiger with a WC/CoCr coating (d) Various textile machinery components (e) Biocompatible Titanium coating on a hip implant. (Graphic courtesy of Oerlikon Metco)

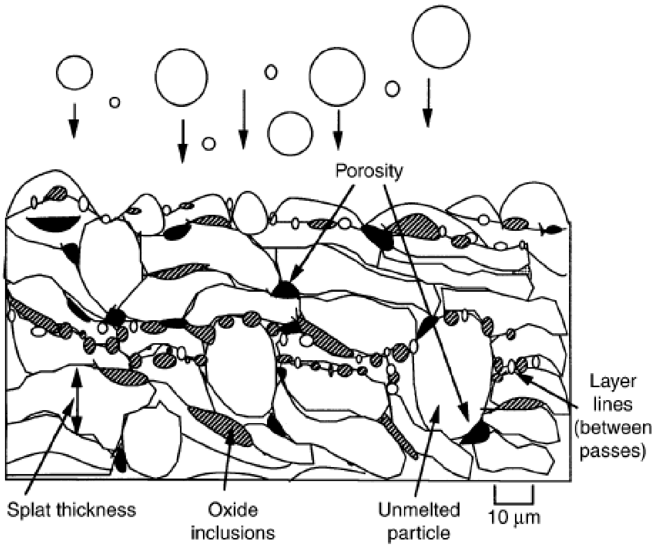

Scheme 1.6 Schematic illustration of architectural defects in microstructure of thermal spray coatings.
(Courtesy of Coating Structures, Properties, and Materials, as published in Handbook of Thermal Spray Technology J.R. Davis, editor, p 47-53. ASM International and the Thermal Spray Society, 2004)

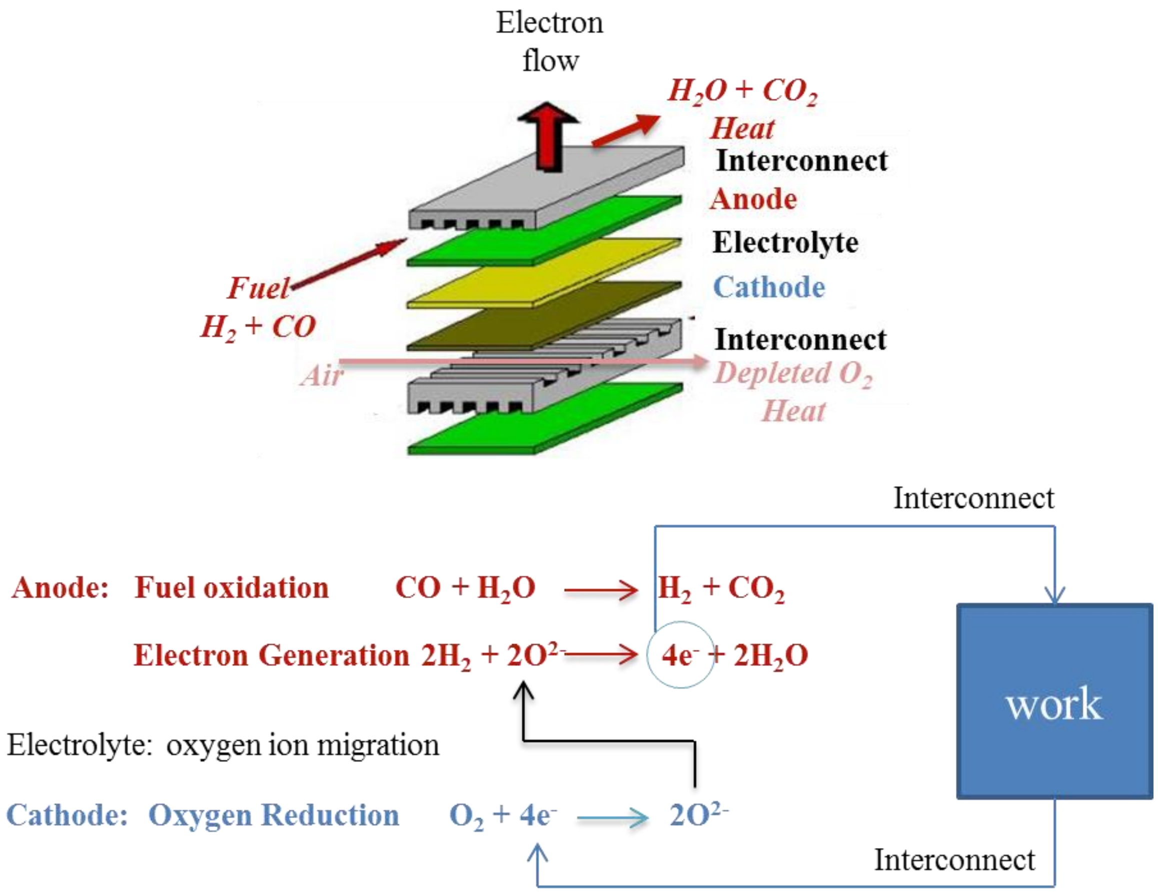

Scheme 1.7 Schematic illustration of planar type SOFC structure and their chemical reaction formulae at the each stage of layers.
(courtesy of http://www.csa.com/discoveryguides/fuecel/overview.php)

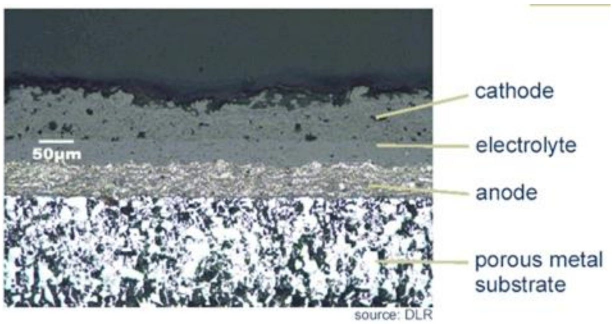

Scheme 1.8 Optical micrograph of plasma sprayed planar-type solid oxide fuel cell. (Courtesy of DLR)

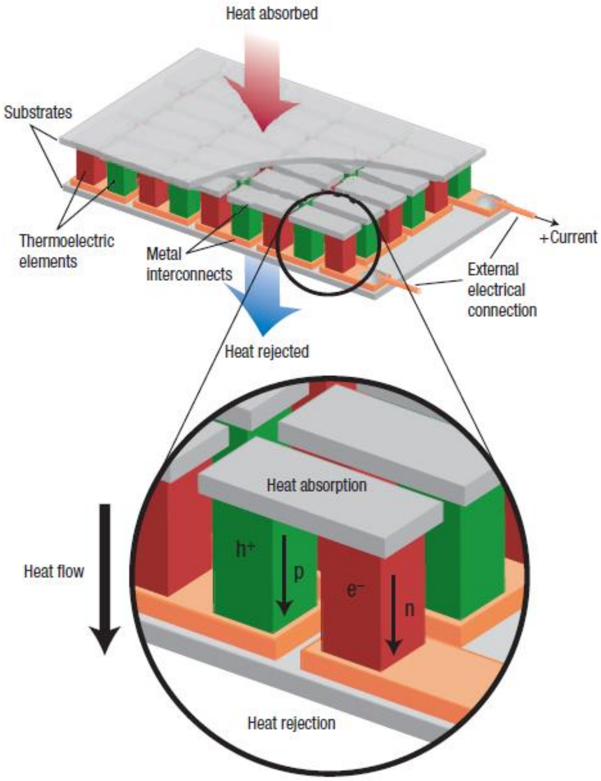

Scheme 1.9 Thermoelectric module showing the direction of charge flow on both cooling and power generation.
(Courtesy of G. Jeffrey Snyder and E. S. Toberer. Nature Materials vol 7 (2008) 105-114.)

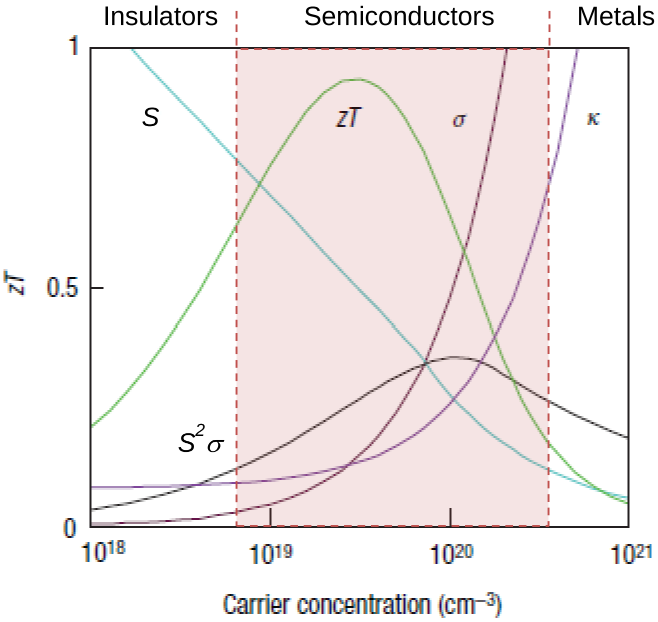

Scheme 1.10 Optimizing *ZT* through carrier concentration tuning. Maximizing the efficiency (*ZT*) of a thermoelectric involves a compromise of thermal conductivity (*k*: plotted on the y axis from 0 to a top value of 10 W/mK) and Seebeck coeffficient (*S*); 0 to 500 μV/K) with electrical conductivity (σ; 0 to 5000 S/cm). The thermoelectric power factor $S^2\sigma$ maximizes at higher carrier concentration than *ZT*. The difference between the peak in $S^2\sigma$ and *ZT* is greater for the newer lower-k_l materials.

(Courtesy of Rowe, D. M. & Min. G. Alpha-plot as a thermoelectric material performance indicator. *J. Mater. Sci. Lett.* **14** (1995) 617-619).

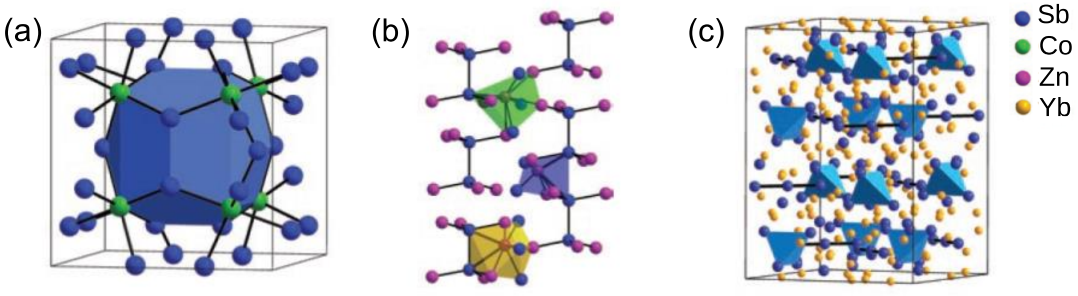

Scheme 1.11 Complex crystal structures that yield low lattice thermal conductivity. (a) The skutterudite structure is composed of tilted octahedra of $CoSb_3$ creating large void spaces shown in blue. (b) The room-temperature structure of Zn_4Sb_3 has a crystalline Sb sublattice (blue) and highly disordered Zn sublattice containing a variety of interstitial sites (in polyhedra) along with the primary sites (purple). (c) The complexity of the $Yb_{14}MnSb_{11}$ unit cell is illustrated, with $[Sb_3]^{7-}$ trimers, $[MnSb_4]^{9-}$ tetrahedra, and isolated Sb anions. The Zintl formalism describes these units as covalently bound with electrons donated from the ionic Yb^{2+} sublattice (yellow). (Courtesy of G. Jeffrey Snyder and E. S. Toberer. Nature Materials vol 7 (2008) 105-114.)

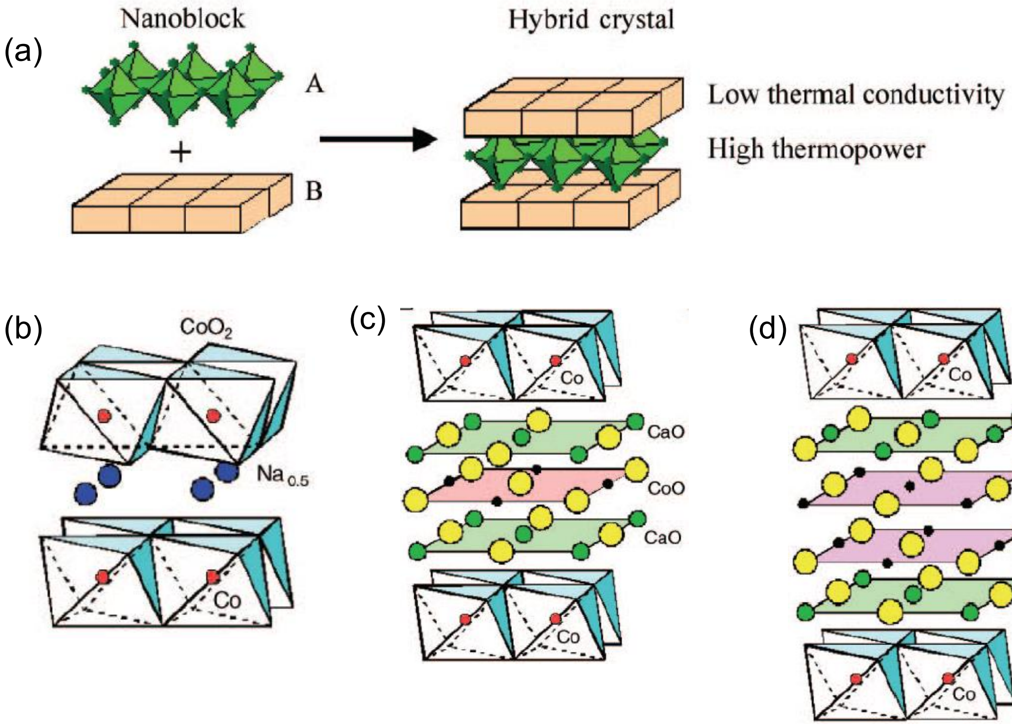

Scheme 1.12 (a) Design of new functional oxides according to the concept of nanoblock integration. Schematic illustration of the crystal structure of CoO_2-based TE oxides: (b) Na_xCoO_2, (c) a Ca-based Co oxide known as $Ca_3Co_4O_9$, and (d) the Bi-based Co oxide $Bi_2Sr_2Co_2O_y$.

(Courtesy of K. Koumoto, I. Terasaki, and R. Funahashi. MRS Bulletin, vol 31 (2006) 206-210.)

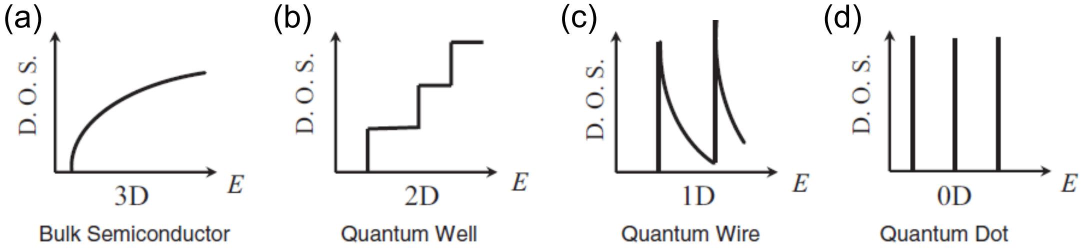

Scheme 1.13 Electronic density of states for (a) a bulk 3D crystalline semiconductor, (b) a 2D quantum well, (c) a 1D nanowire or nanotube, and (d) a 0D quantum dot.
(Courtesy of Dresselhaus, M. S., Chen, G., Tang, M. Y., Yang, R., Lee, H., Wang, D., Ren, Z., Fleurial, J.-P. & Gogna, P. New directions for low-dimensional thermoelectric materials. *Adv. Mater.* **19**, 1043-1053 (2007).

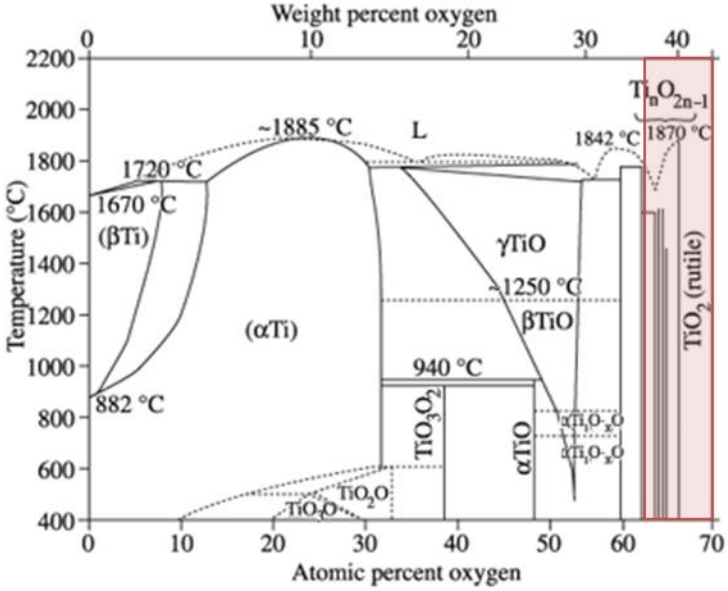

Scheme 1.14 Phase diagram of Ti-O system. The red box indicates the location where the phases containing in the coatings in this work.

(Courtesy of J. L. Murray and H. A. Wriedt, Ti-O phase diagram, In: R. Boyer, G. Welsch and E. W. Collings, Materials properties handbook: titanium alloys. Ohio, Estados Unidos: ASM International; 1994. p. 130).

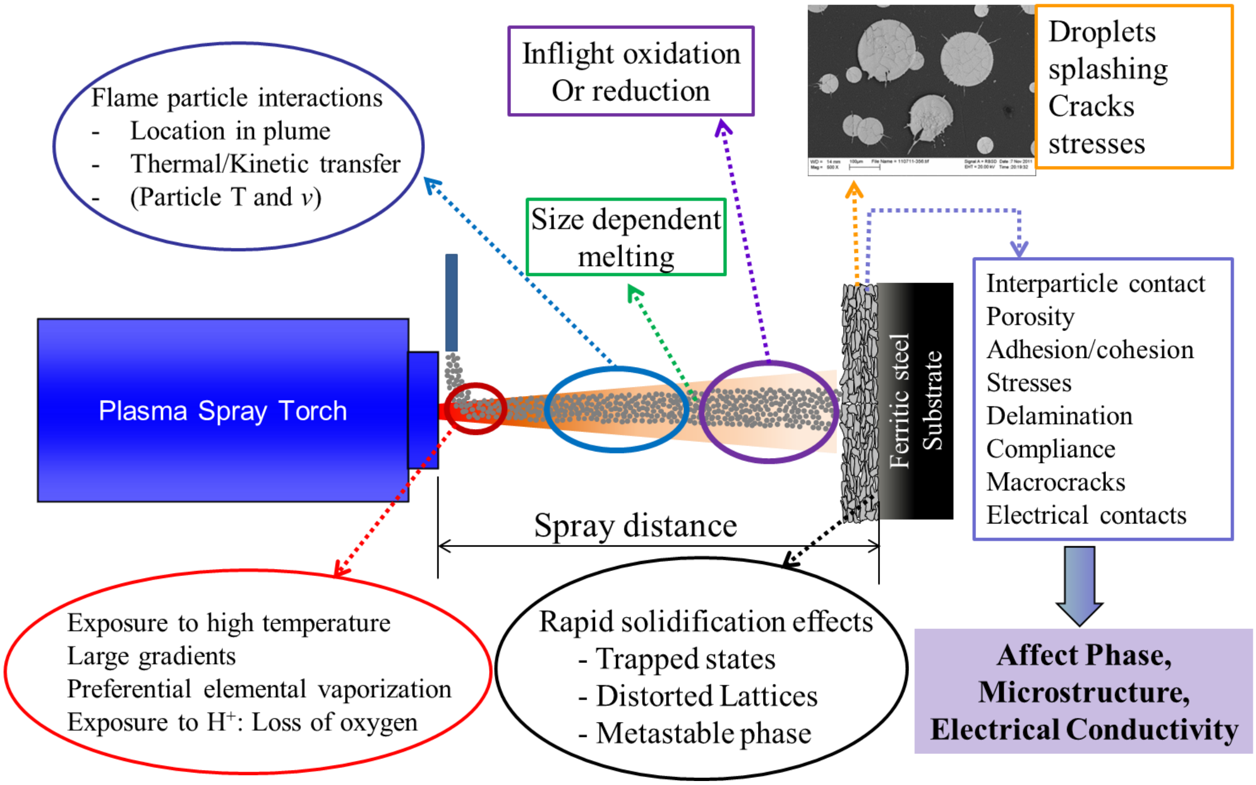

Scheme 2.1 Schematic illustration of process-microstructure-property relationship.

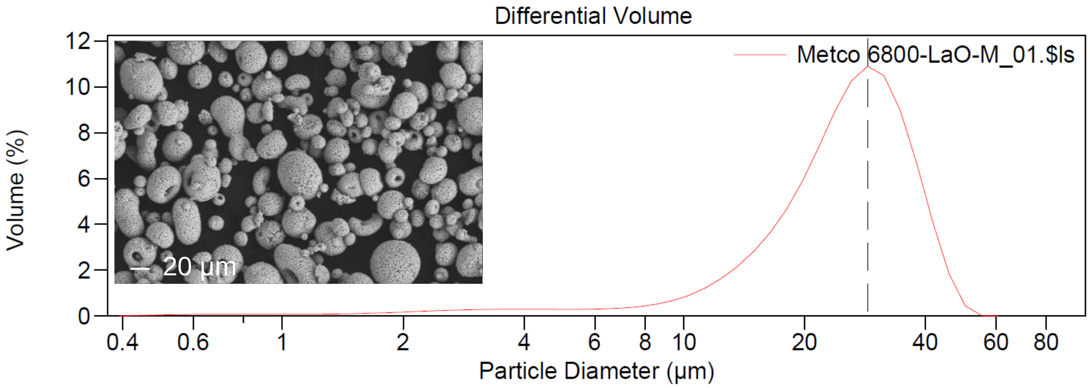

```
Calculations from 0.375 µm to 2000 µm

Volume:          100%
Mean:            25.36 µm      S.D.:          9.868 µm
Median:          25.84 µm      C.V.:          38.9%
D(3,2):          15.11 µm      Skewness:   -0.247 Left skewed
Mode:            28.70 µm      Kurtosis:   -0.120 Platykurtic
d10:             12.46 µm
d50:             25.84 µm
d90:             37.89 µm

% <      10       25       50       75       90
µm       12.46    19.16    25.84    32.19    37.89
```

Figure 3.1 Particle size distribution and electron micrograph of $La_{0.8}Sr_{0.2}MnO_3$ (LSM) feedstock powder (Metco6800).

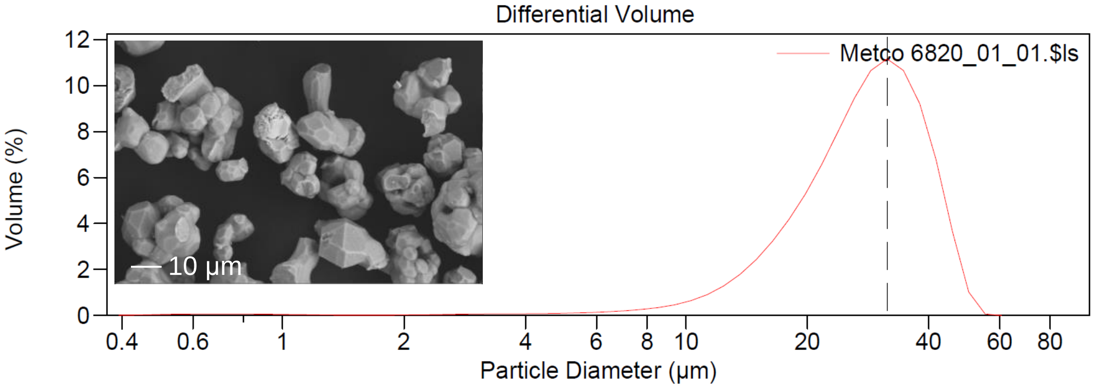

```
Calculations from 0.375 µm to 2000 µm

Volume:                   100%
Mean:                     28.02 µm        S.D.:              9.639 µm
Median:                   28.19 µm        C.V.:              34.4%
D(3,2):                   19.40 µm        Skewness:      -0.148 Left skewed
Mode:                     31.50 µm        Kurtosis:      -0.221 Platykurtic
d10:                      15.59 µm
d50:                      28.19 µm
d90:                      40.66 µm

% <         10          25          50          75          90
µm          15.59       21.38       28.19       34.94       40.66
```

Figure 3.2 Particle size distribution and electron micrograph of $Mn_{1.5}Co_{1.5}O_4$ (MCO) feedstock powder (Metco6820).

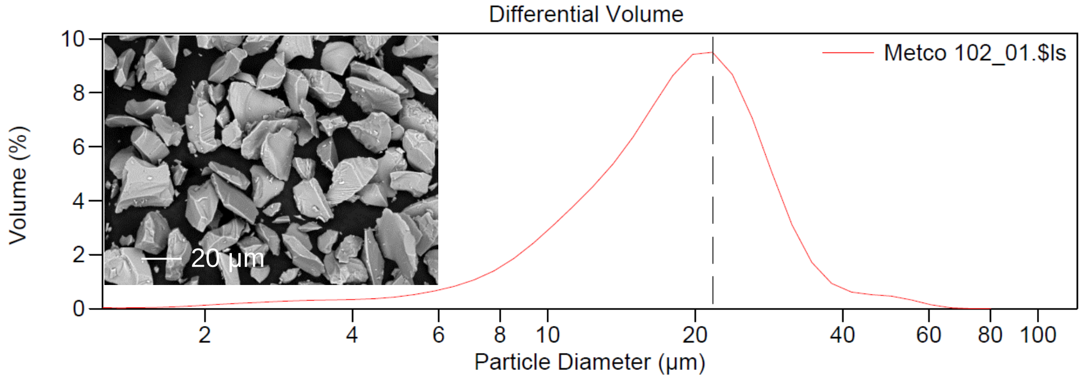

```
Calculations from 0.375 µm to 2000 µm

Volume:          100%
Mean:            18.81 µm      S.D.:             8.643 µm
Median:          18.39 µm      C.V.:             46.0%
D(3,2):          11.46 µm      Skewness:   0.824 Right skewed
Mode:            21.69 µm      Kurtosis:   2.255 Leptokurtic
d10:             8.654 µm
d50:             18.39 µm
d90:             28.92 µm

% <      10       25       50       75       90
µm       8.654    13.09    18.39    23.66    28.92
```

Figure 3.3 Particle size distribution and electron micrograph of $TiO_{1.9}$ feedstock powder (Metco102).

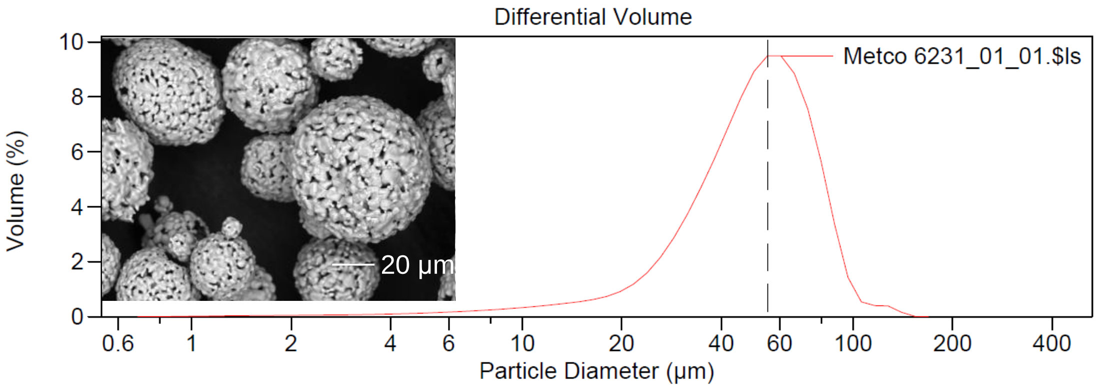

Calculations from 0.375 µm to 2000 µm

Volume:	100%		
Mean:	51.81 µm	S.D.:	21.53 µm
Median:	51.24 µm	C.V.:	41.6%
D(3,2):	35.01 µm	Skewness:	0.315 Right skewed
Mode:	55.13 µm	Kurtosis:	0.594 Leptokurtic
d_{10}:	25.18 µm		
d_{50}:	51.24 µm		
d_{90}:	79.00 µm		

% <	10	25	50	75	90
µm	25.18	37.35	51.24	65.77	79.00

Figure 3.4 Particle size distribution and electron micrograph of $TiO_{1.7}$ feedstock powder (Metco6231A).

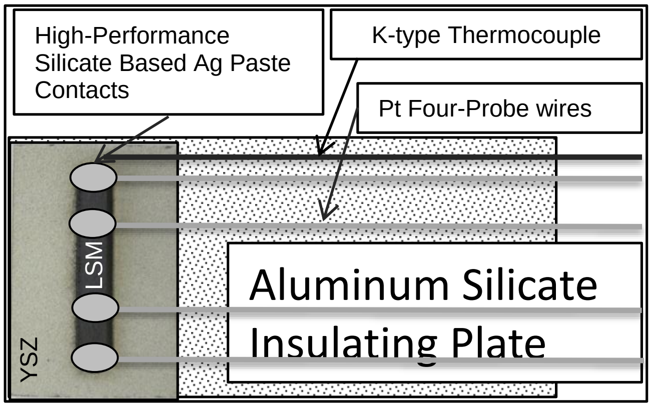

Figure 3.5 Geometry confined LSM coating on YSZ coated SS and self-developed electrical conductivity measurement configuration.

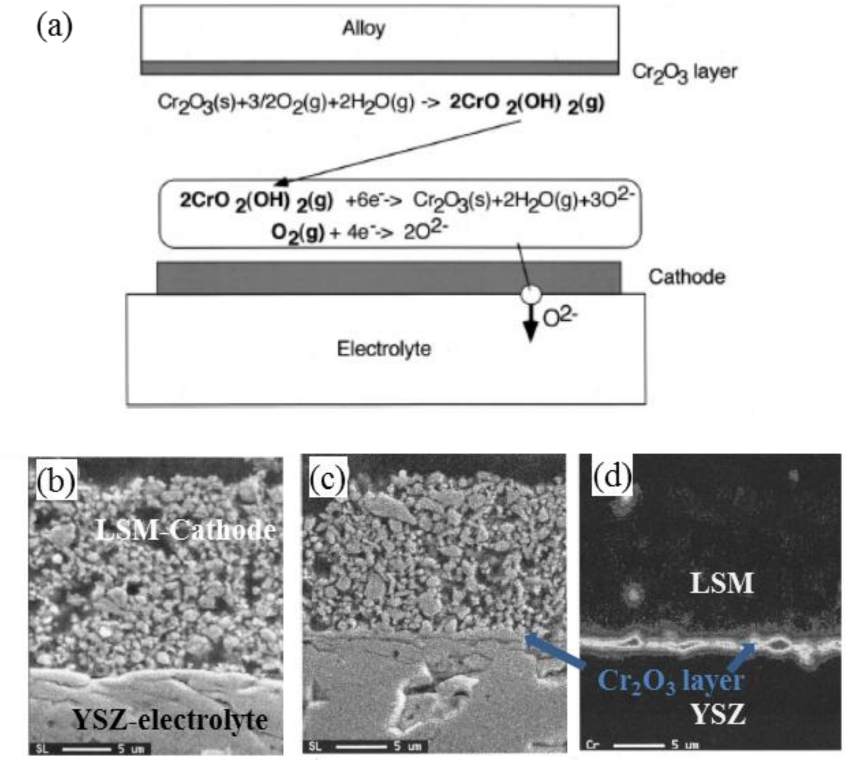

Figure 4.1 (a) Schematic illustration of the chromia deposition process at the LSM/YSZ interface when the chromium-containing alloy is used as an interconnector. (b) A cross-sectional SEM photograph of the LSM/8YSZ interface before the Cr poisoning. (c) cross-sectional SEM photograph and (d) distribution of Cr element obtained by EPMA of LSM/8YSZ interface after a polarization for 100 h with a current density of 0.3 A cm^{-2} with the alloy current collector at 1073.
(Courtesy of K. Y. Matsuzaki, I. Yasuda, J. Electrochem. Soc. 148 (2001) A126-A131.)

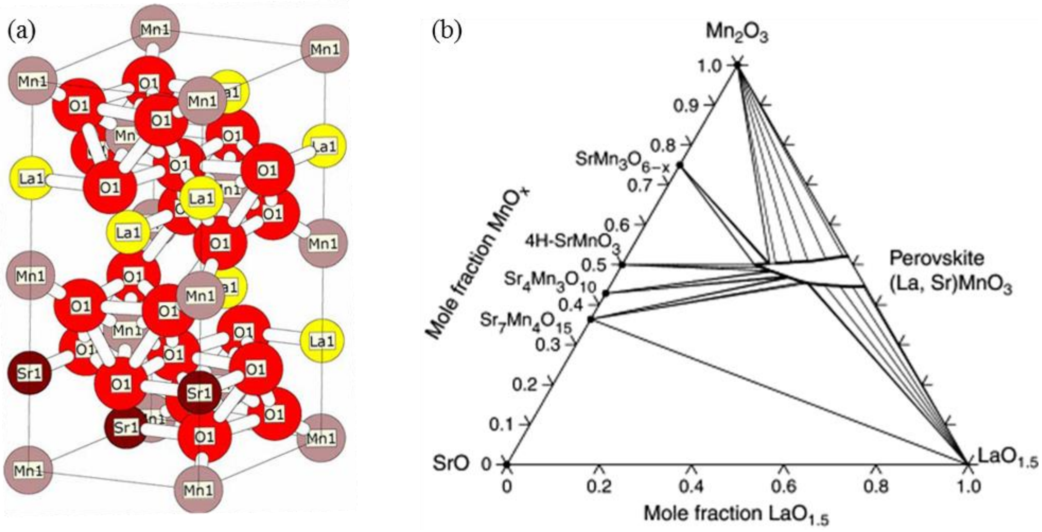

Figure 4.2 Crystal structure of $La_{0.7}Sr_{0.3}MnO_3$ (a) and phase diagram of $LaO_{1.5}$–SrO–MnO_x system in air at 1073 K (b).

(Courtesy of S. P. Jiang. *Journal of Materials Science*, **43** 6799 (2008) and A. Nicholas Grundy *et. al. Computer Coupling of Phase Diagrams and Thermochemistry*, **28** 191 (2004))

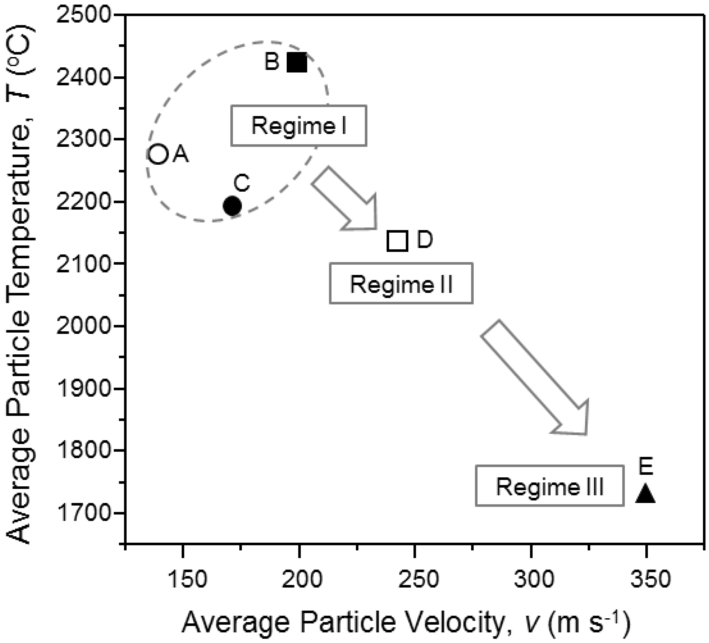

Figure 4.3 First-order *T*-*v* process map of LSM coatings.

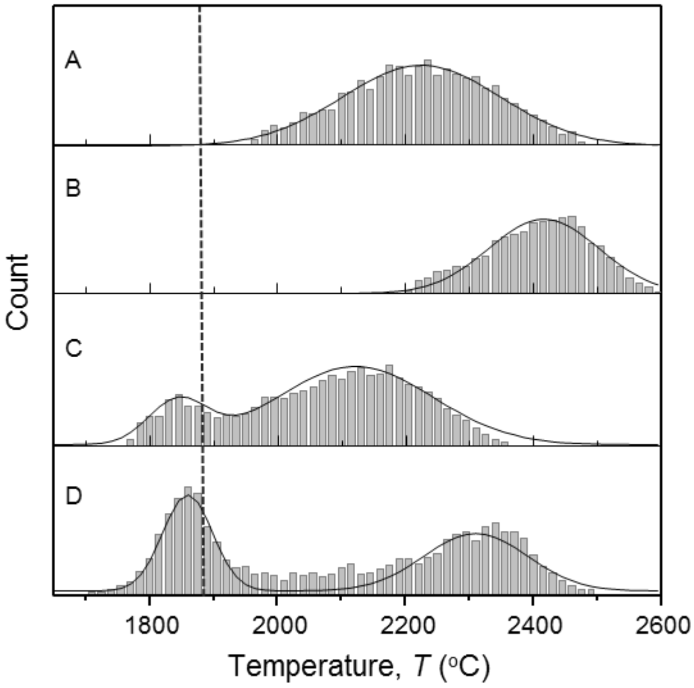

Figure 4.4 Results of 5000 LSM particle temperature diagnostic of A through D conditions. Dashed line presents melting temperature of LSM particles.

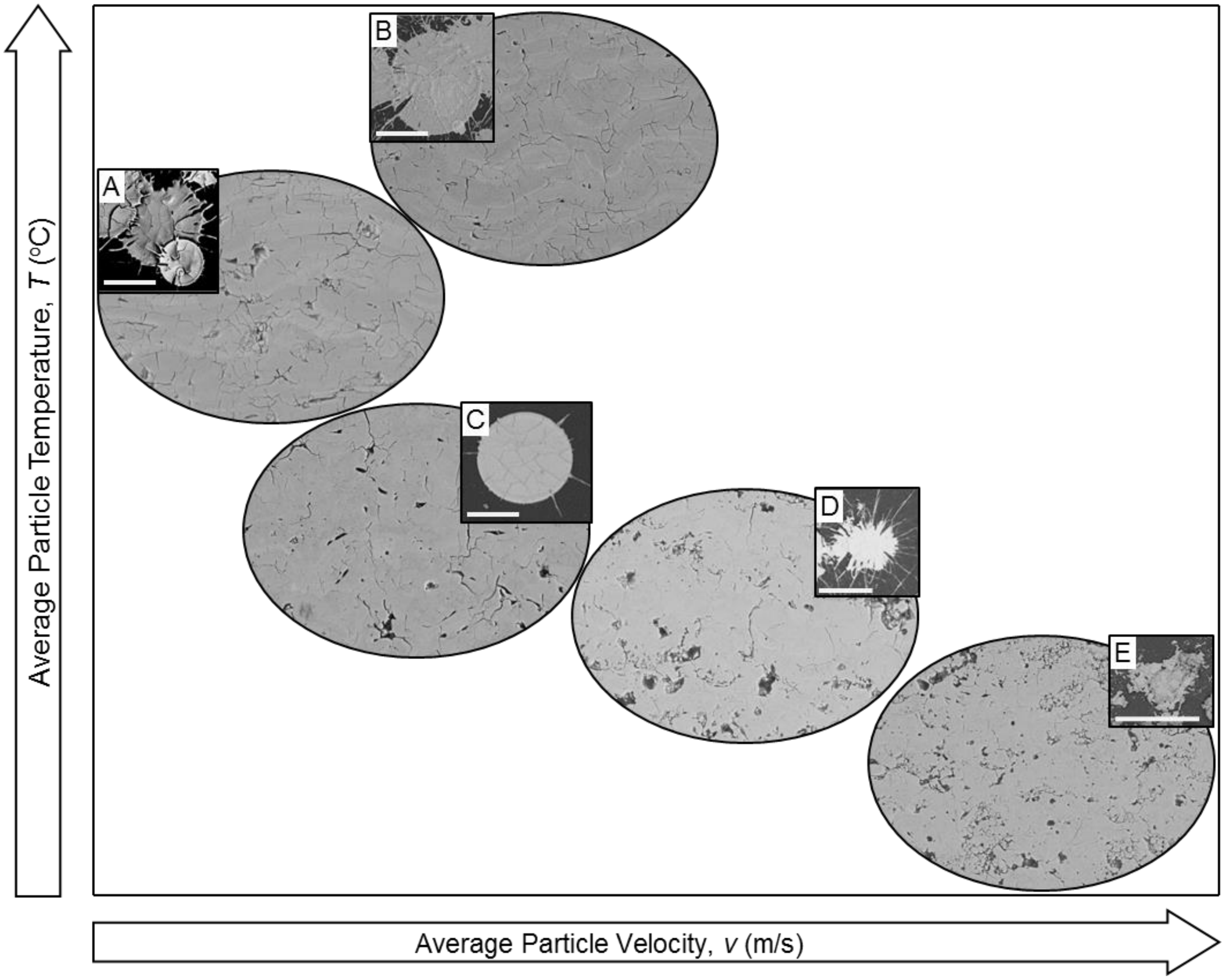

Figure 4.5 Cross-sectional SEM images of as-sprayed LSM coatings with 3.0k magnification. Inset: SEM images of splats. All scale bars represent 100 μm.

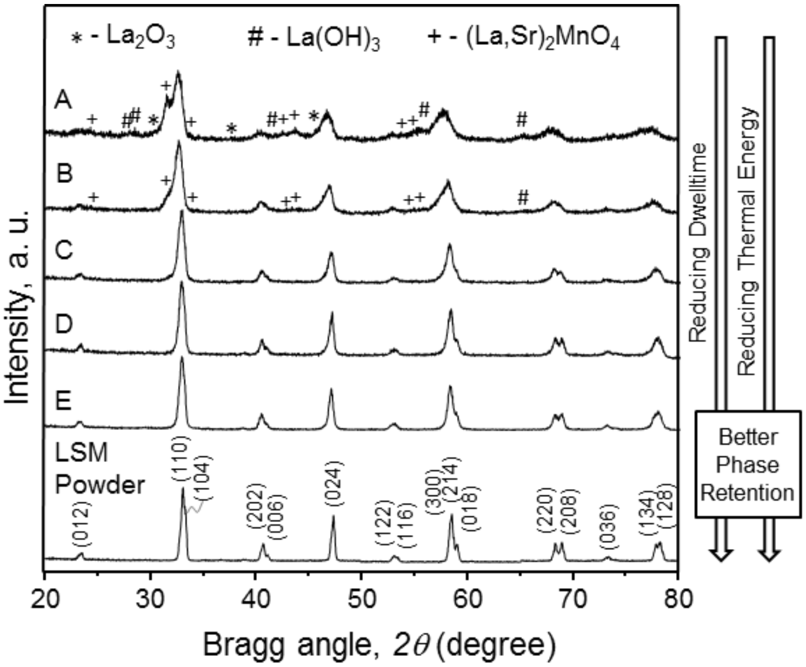

Figure 4.6 Powder XRD patterns of as-sprayed LSM coatings A through E and feedstock powder.

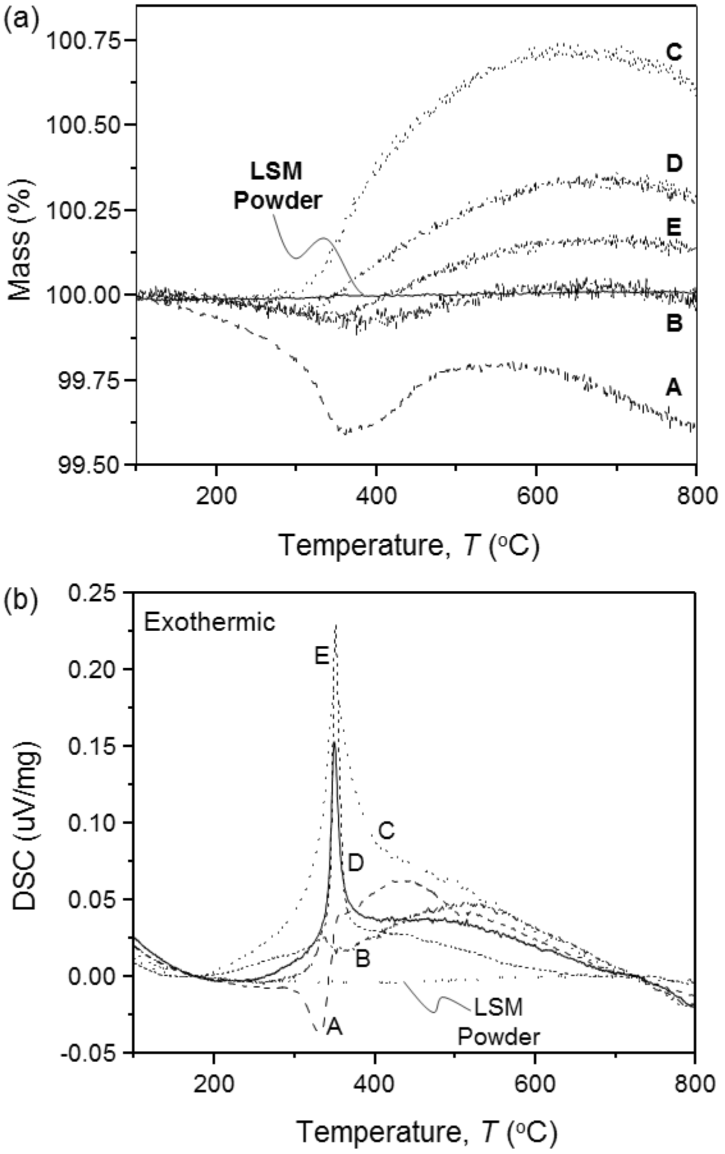

Figure 4.7 (a) TGA and (b) DSC curves of freestand LSM coatings and feedstock powder.

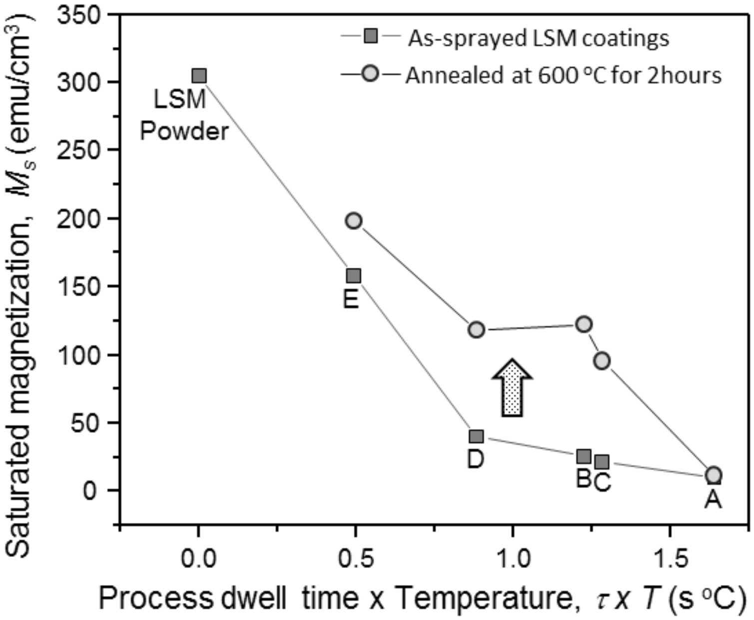

Figure 4.8 Saturated magnetizations (M_s) vs. product of process dwell time and temperature of LSM feedstock powder and freestand as-sprayed and annealed coatings A through E.

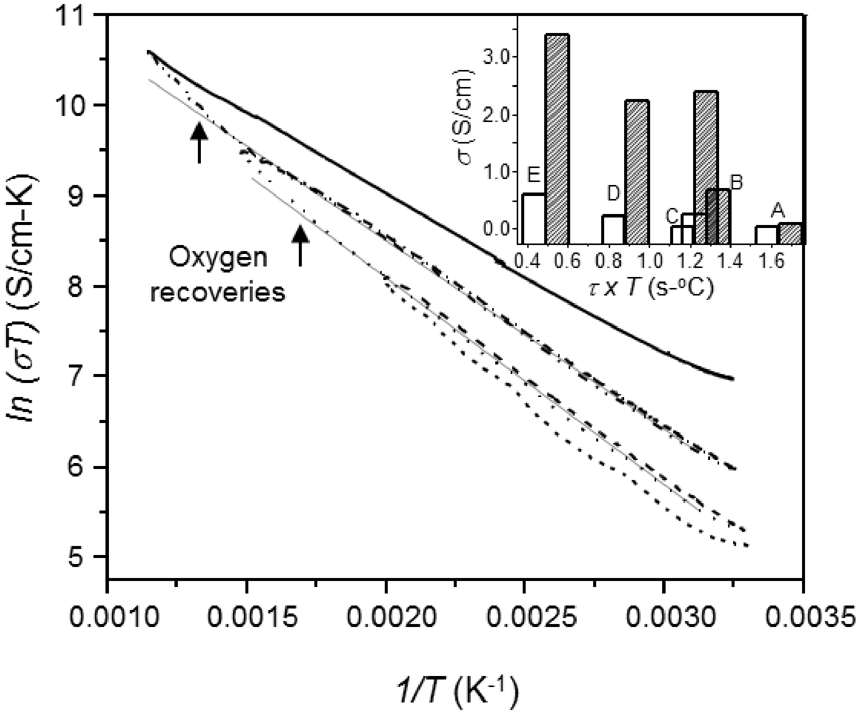

Figure 4.9 Temperature dependent electrical conductivity of coating E with successive 200 °C interval thermal cycles. Arrows indicate oxidation points. Both gray solid lines are extrapolation lines. Inset: Room temperature electrical conductivity of as-sprayed (empty block) and annealed at 600 °C (shaded block) LSM coatings.

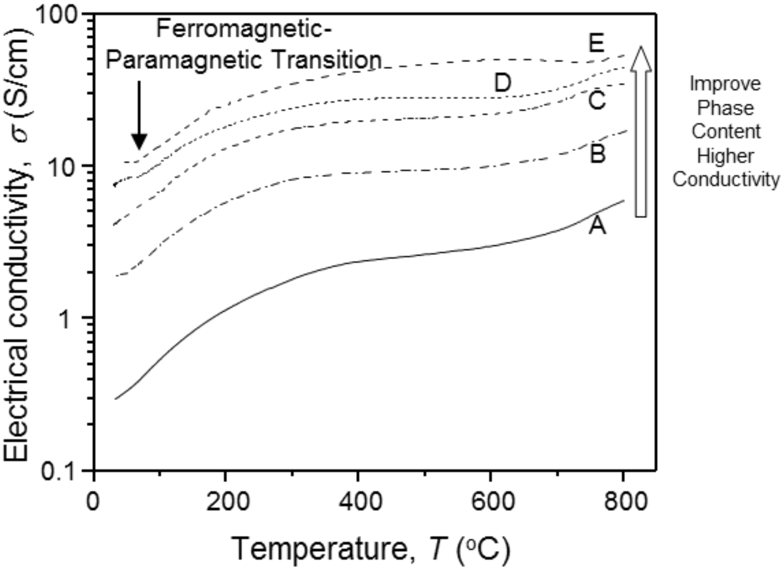

Figure 4.10 Temperature dependent in-plane electrical conductivities of A through E LSM coatings during cooling down from 800 °C after 24 hours annealing.

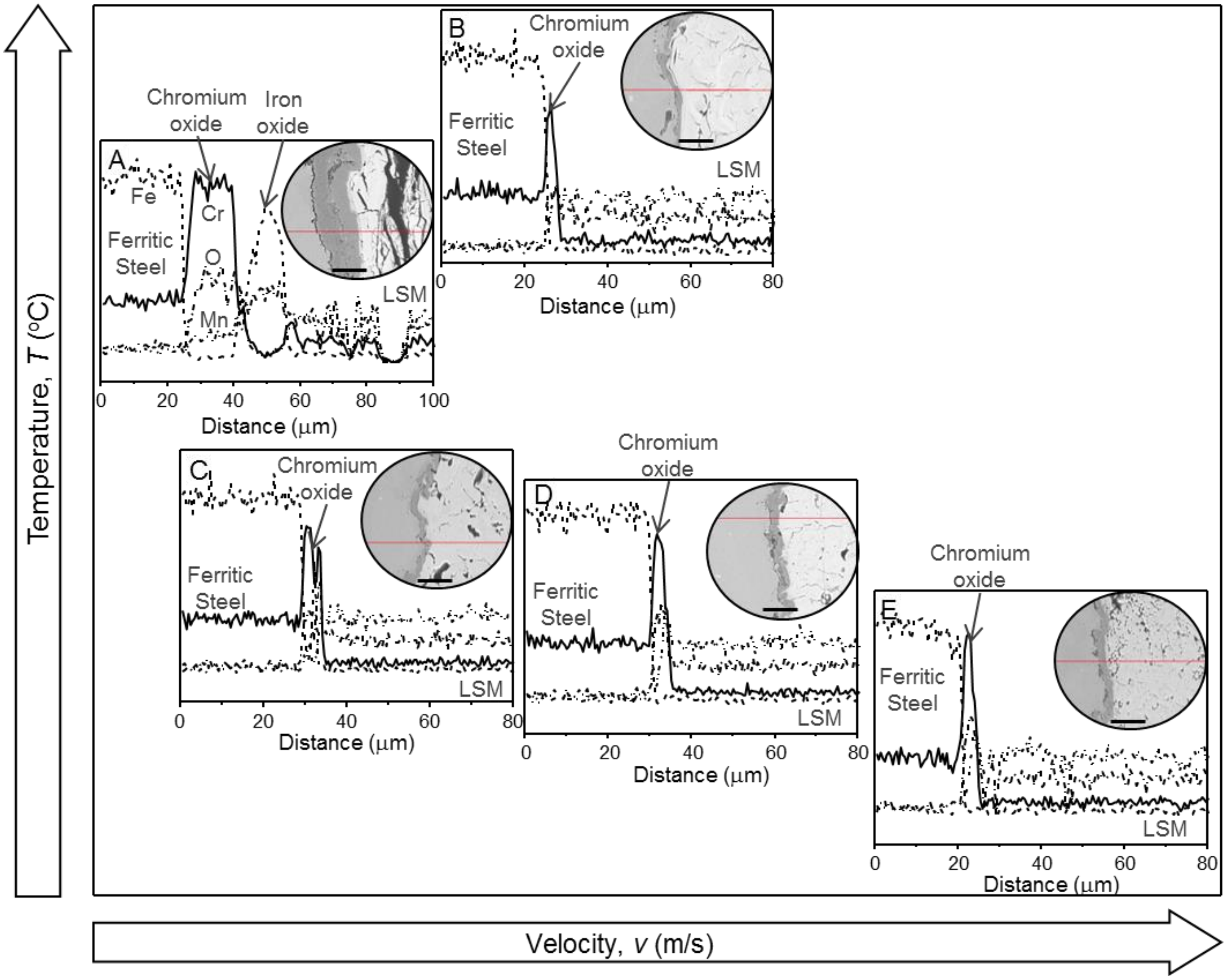

Figure 4.11 Oxide scale test results; cross-sectional SEM images and corresponding EDX line profiles of A through E LSM coatings after annealing process for 600 hours at 800 °C. The all of scale bars in the SEM pictures represent 25 μm.

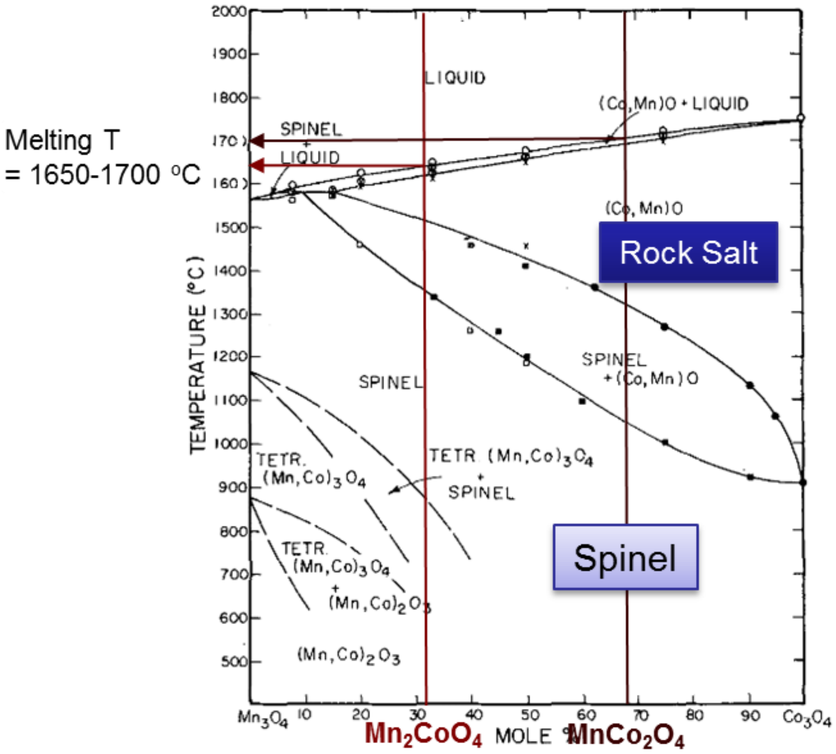

Figure 5.1 Phase diagram of Mn_3O_4–Co_3O_4 system.

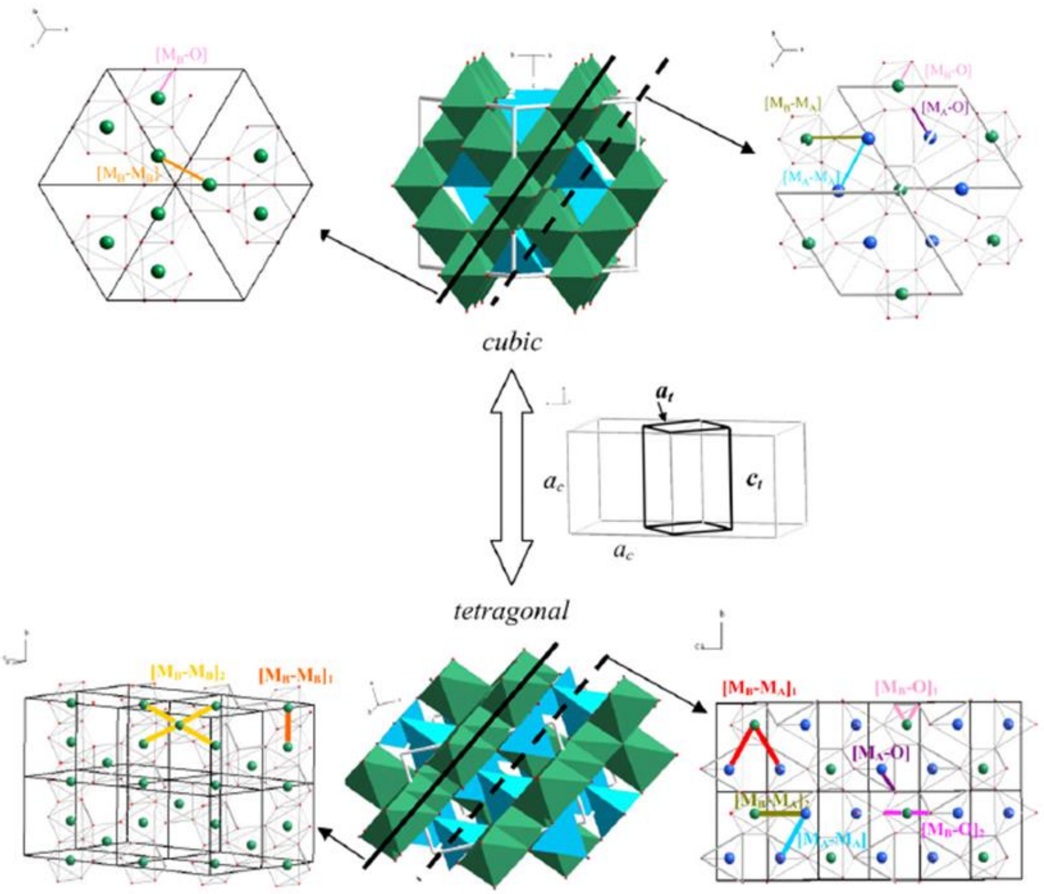

Figure 5.2 Cubic (top) and tetragonal (bottom) spinel structures showing the succession of kagome- (left) and mixte trigonal-type (right) plans formed by the oxygen. In the former plan, only octahedral sites can be occupied by cations, while in the latter both octahedral and tetrahedral sites are available. The shortest [M–M] and [M–O] distances are represented.
(Courtesy of H. Bordeneuve, C. Tenailleau, S. Guillemet-Fritsch, R. Smith, E. Suard, A. Rousset. Solid State Sciences **12** (2010) 379-386.)

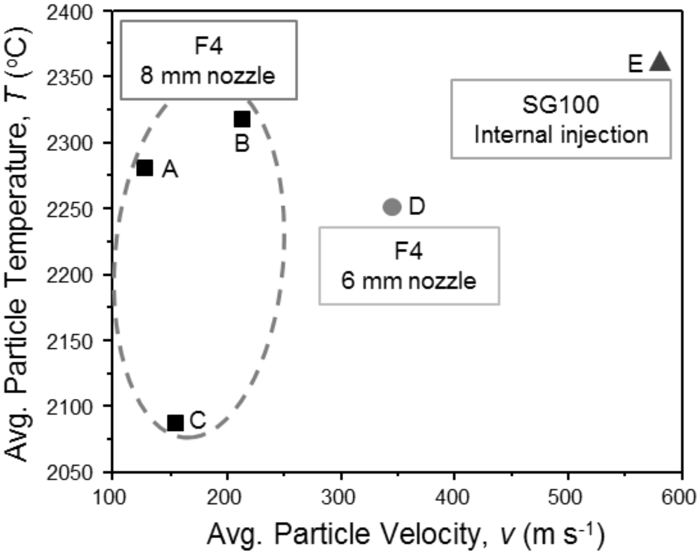

Figure 5.3 First-order *T*-*v* process map of MCO coatings with torch hardware information.

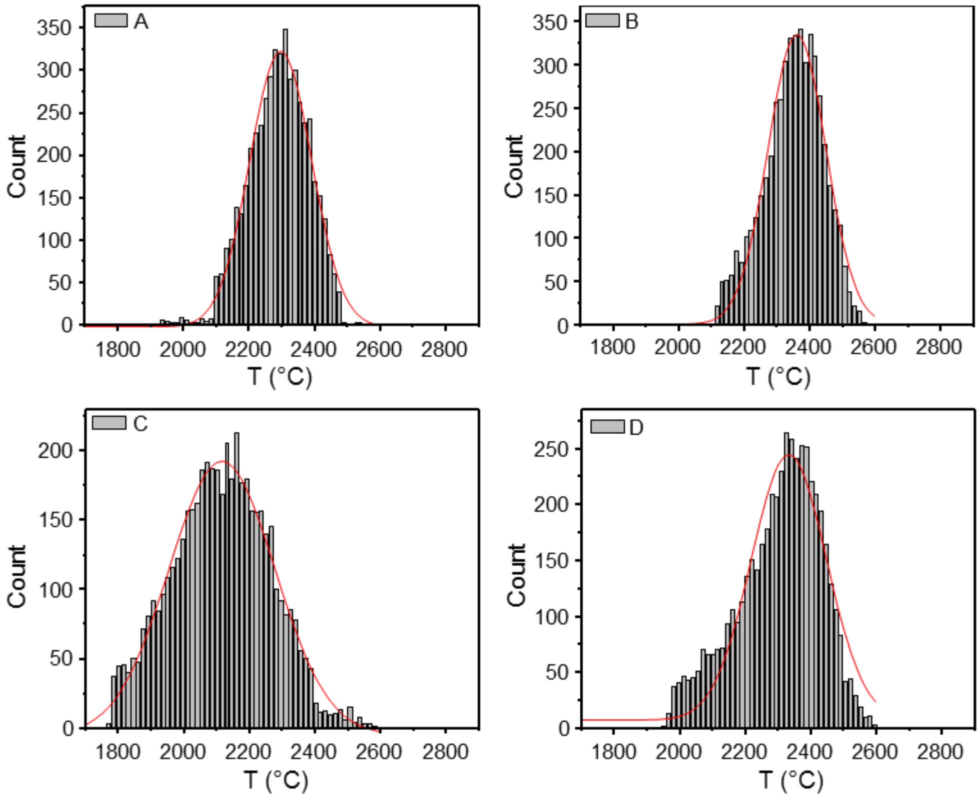

Figure 5.4 Results of 5000 MCO particle temperature diagnostic of A through D conditions.

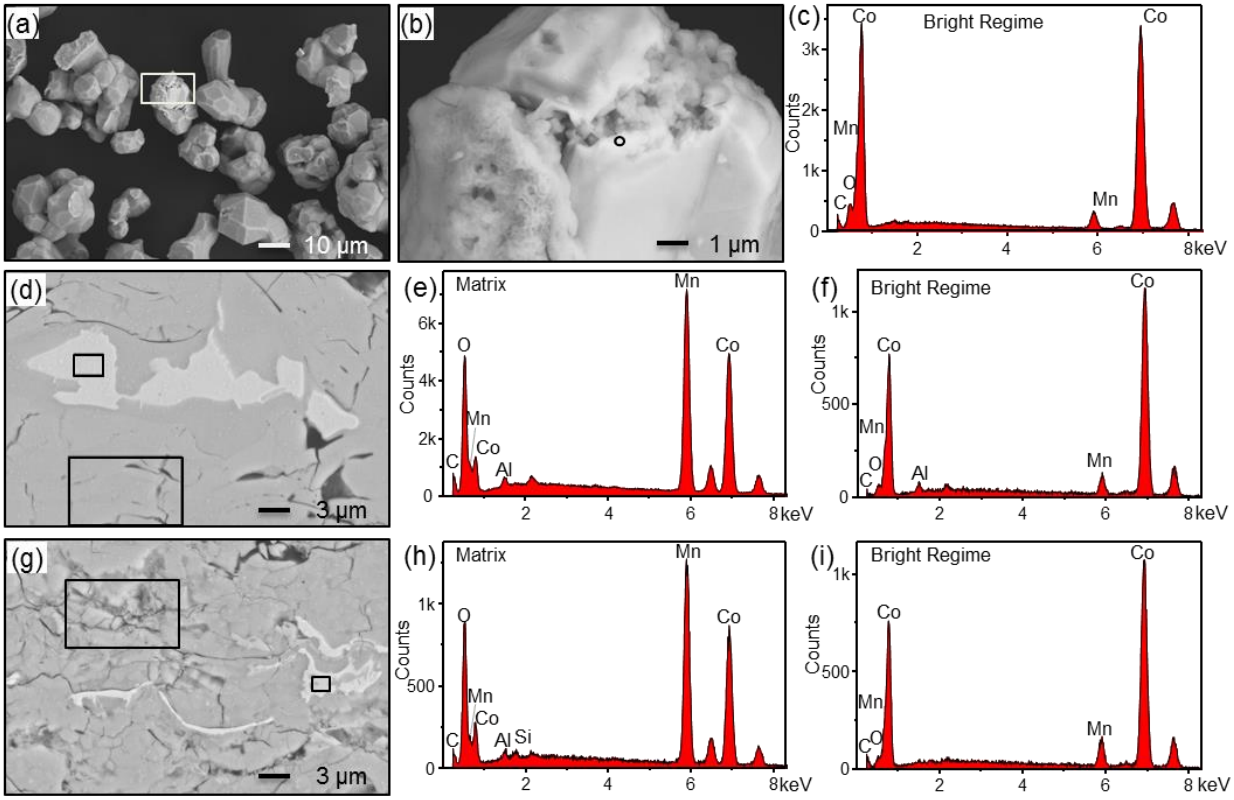

Figure 5.5 (a) Microstructure of feedstock MCO powder with 3.00k magnification. (b) Magnified image (×30.00k) of the box in Figure 5.3(a). (c) EDX spectrum at the marked bright regime in Figure 5.3(b). (d) and (g) Cross sectional microstructure with 10.00k magnification of C and E coatings, respectively. (e) and (h) EDX spectra at the matrix regimes in Figure 5.3(d) and (g), respectively. (f) and (i) EDX spectra at the bright regimes in Figure 5.3(d) and (g), respectively.

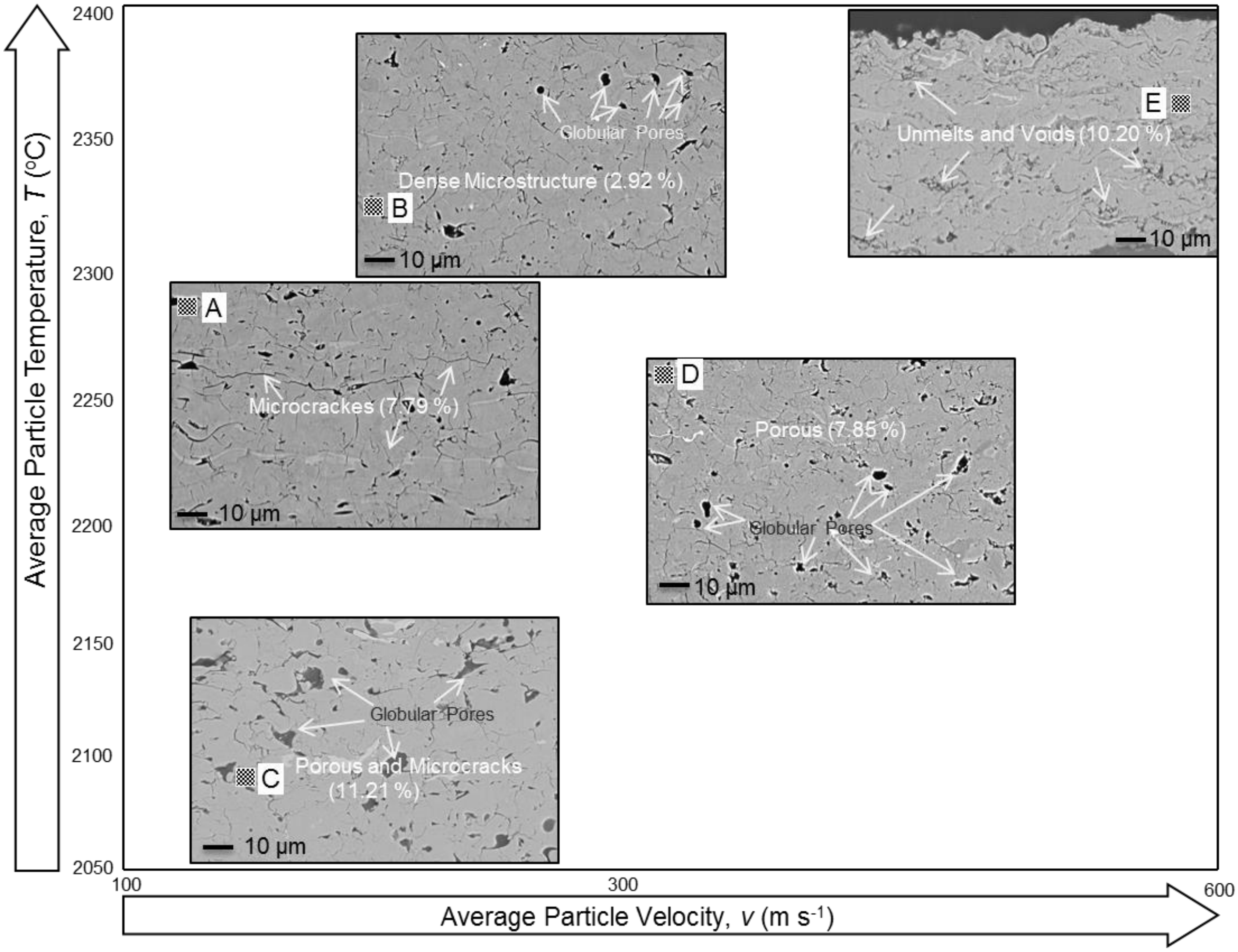

Figure 5.6 Cross-sectional SEM images with 3.00k magnification of as-sprayed MCO coatings on 1st order process map locations. Porosity (%) of coatings calculated by image analysis is displayed in the images.

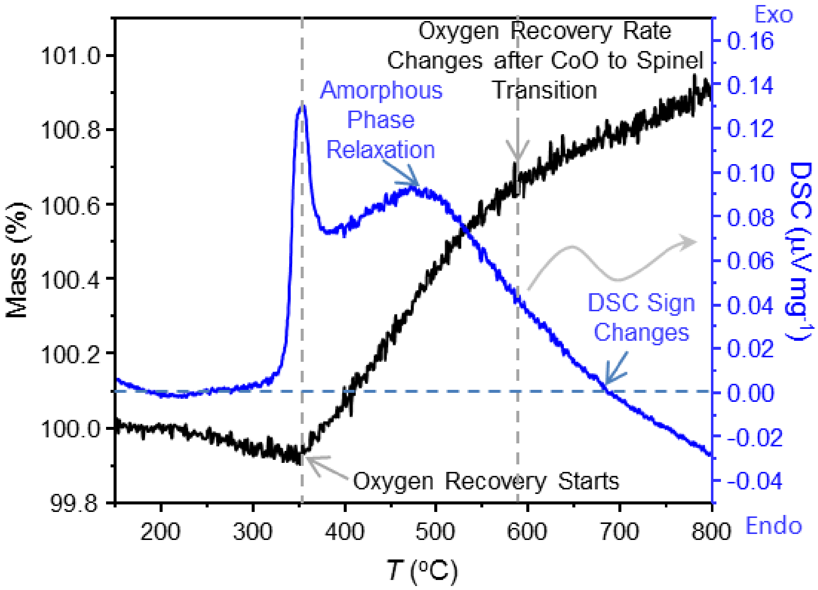

Figure 5.7 TGA/DSC curves of D coating.

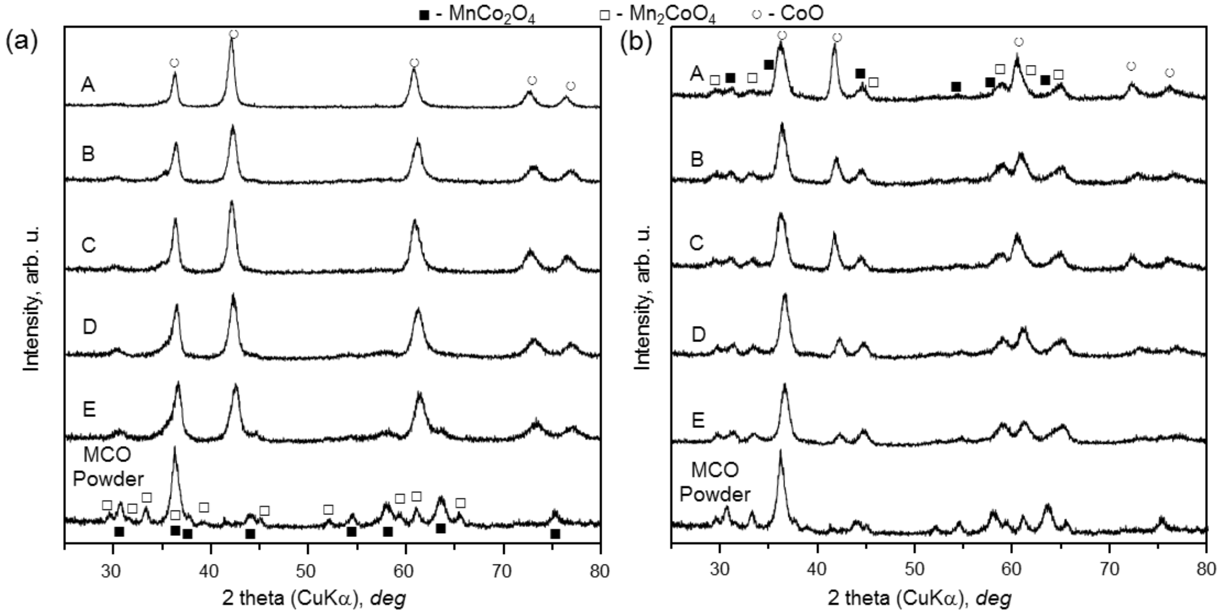

Figure 5.8 XRD patterns (Cu*Kα*) of as-sprayed (a) and annealed (b) MCO coatings and feedstock powder.

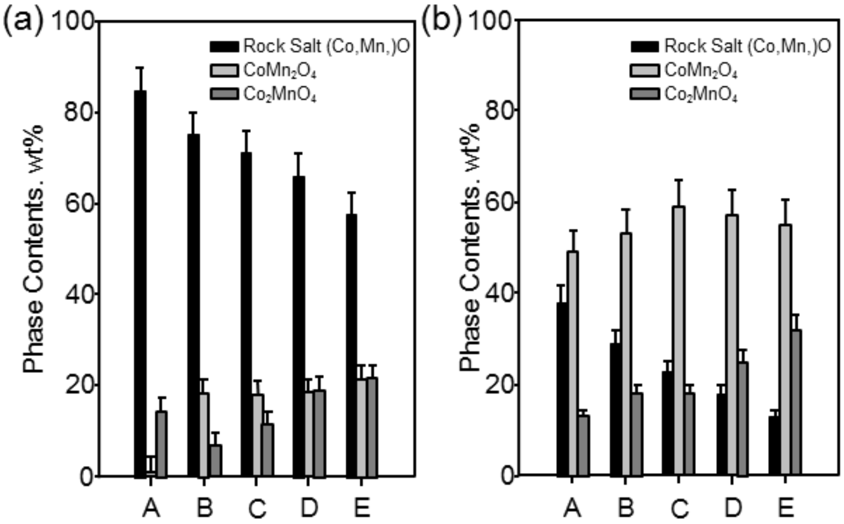

Figure 5.9 (a) coatings and after annealing at 700 °C for 2 hours (b) as determined by Rietveld refinement of XRD patterns.

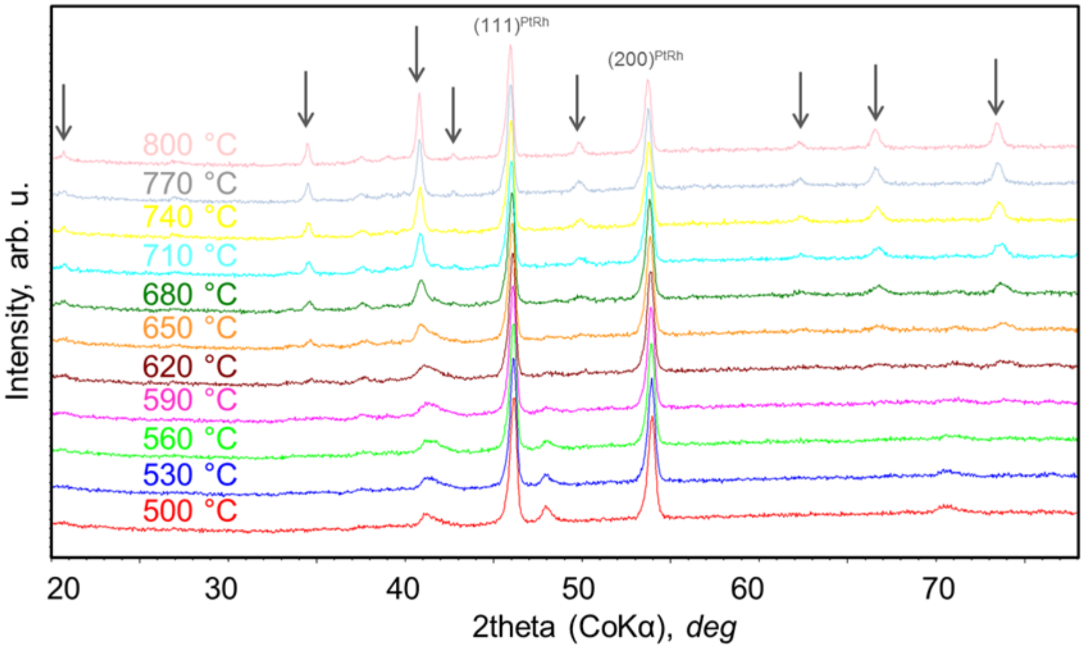

Figure 5.10 Temperature dependent XRD patterns (Co$K\alpha$) of A coating. The transition temperature is at ~620 °C (the 2 intensive reflections at 46 and 54 °2θ over the whole temperature range are from PtRh heating filament). The gray arrows are placed above the reflections of distorted tetragonal spinel.

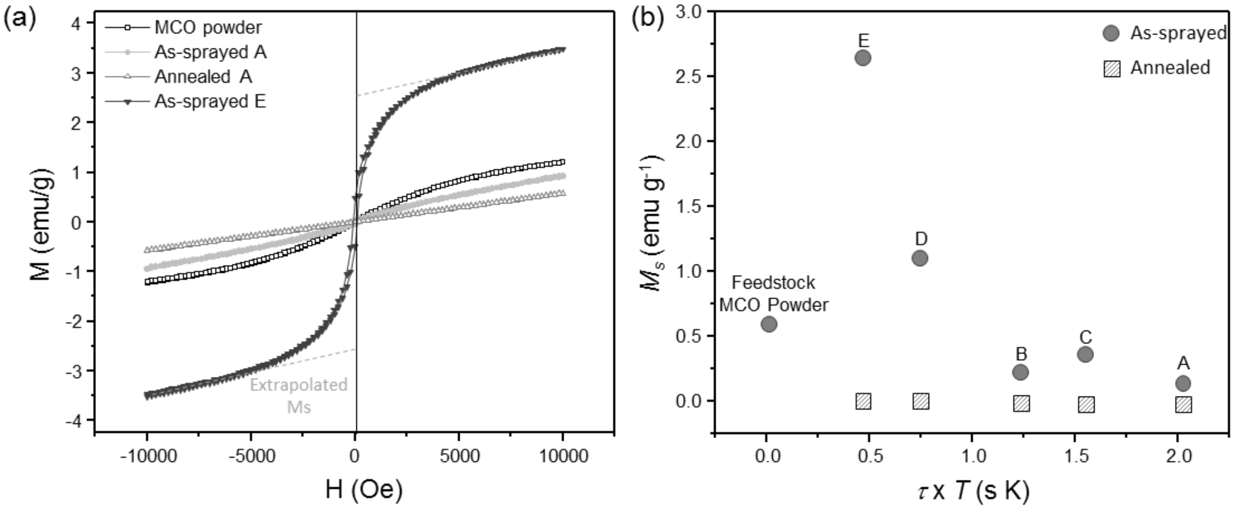

Figure 5.11 (a) Magnetic hysteresis curves of as-sprayed and annealed MCO coatings (A and E conditions) and feedstock powder. (b) Extrapolated saturated magnetizations (M_s) vs. product of process dwell time (τ) and temperature (T) of MCO feedstock powder and freestanding as-sprayed and annealed A through E coatings.

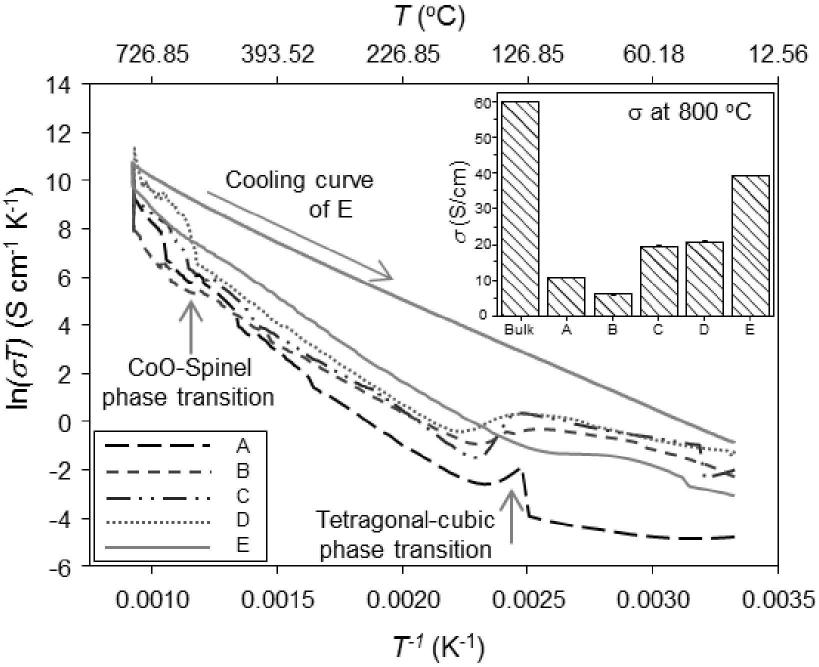

Figure 5.12 Temperature dependent electrical conductivity of A-E coatings up to 800 °C. Arrows indicate cubic-tetragonal and CoO-Spinel phase transition points, respectively. Cooling down curve is only provided for E condition due to the overlay with heating curves. Inset: Electrical conductivity of bulk and A-E MCO coatings at 800 °C.

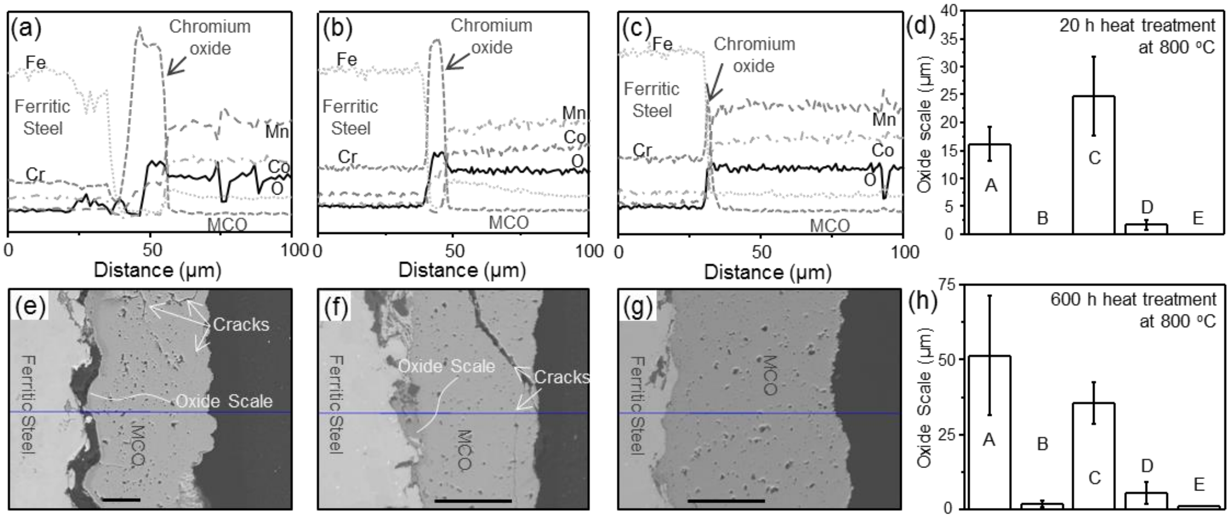

Figure 5.13 EDX line profiles (a)-(c) and 1.00k (A) or 2.00k (C and E) magnified SEM images (e)-(g) of A, C, and E MCO coatings on ferritic steel substrate after 600 hours oxidation at 800 ^{o}C. (EDX profiles and SEM images of coatings B and D are not shown since they are similar to those of coating E.) The all of scale bars in the SEM pictures represent 50 μm. Average oxide scales are provided by bar graphs after 20 h (d) and 600 h (h) heat treatments at 800 °C.

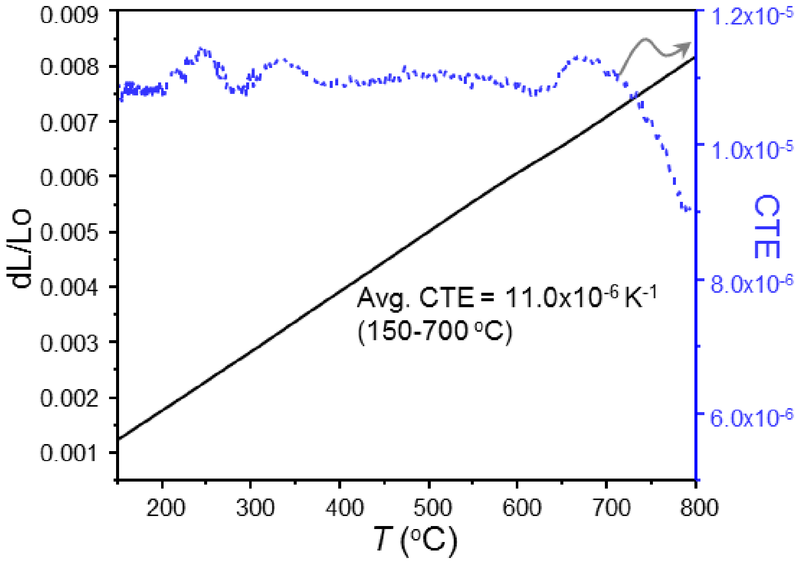

Figure 5.14 dL/Lo and CTE curves of coating D.

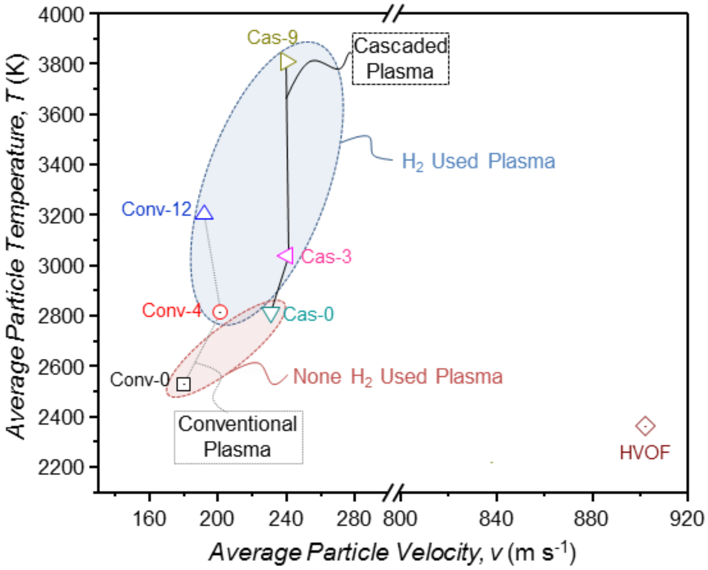

Figure 6.1 First-order process map of TiO_{2-x} coatings with feedstock stoichiometry of $TiO_{1.9}$. Conventional and cascaded plasmas represent F4MB-XL and SinplexPro torches, respectively. Red and blue circled area display non-hydrogen and hydrogen used conditions, respectively.

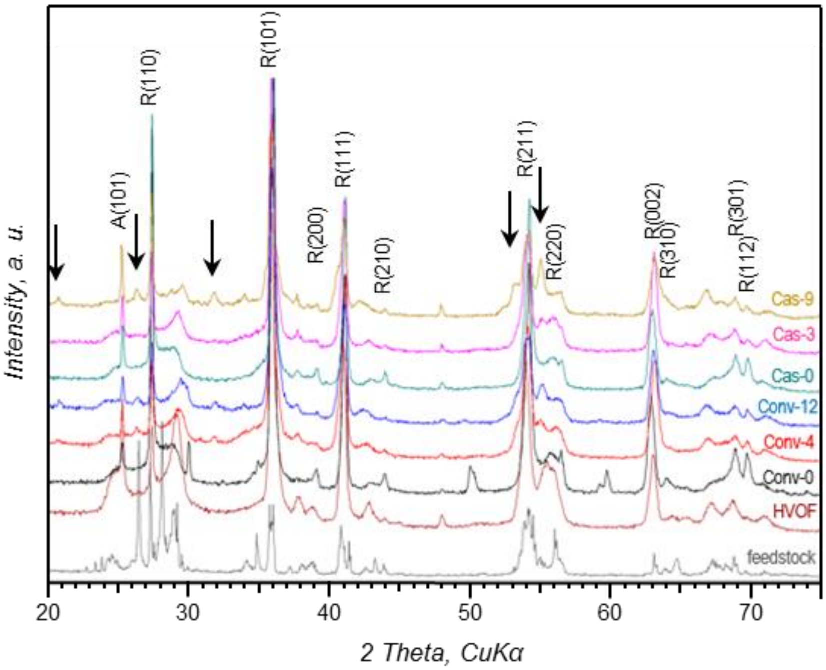

Figure 6.2 Powder XRD patterns of $TiO_{1.9}$ feedstock powder and surfaces of the as-sprayed coatings (R = Rutile, A = anatase, Arrows indicate the emergence of Ti_4O_7 phase. The rest of reflections from Magneli phases (n = 5 – 9)).

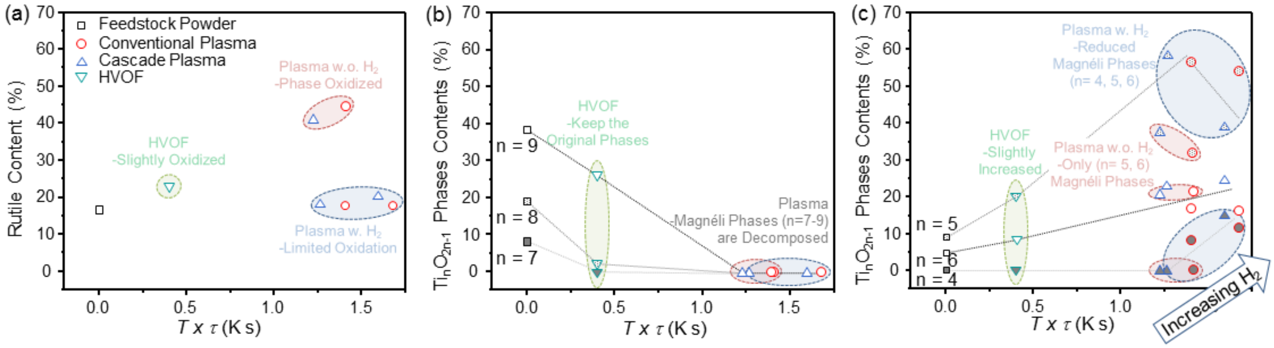

Figure 6.3 Process effect on phase contents in the TiO_{2-x} coatings produced with $TiO_{1.9}$ feedstock. (a) Rutile, (b) Magnéli phases (n = 7 – 9), and (c) Magnéli phases (n = 4 – 6) as a function of product of temperature (*T*) and residential time (*τ*) during the spray process.

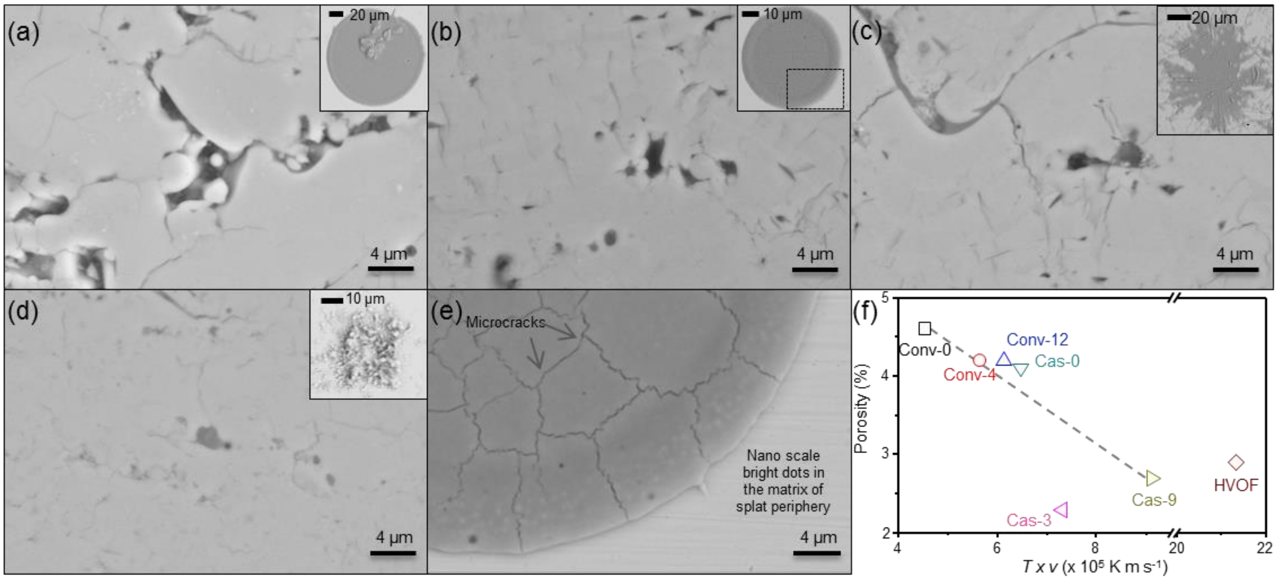

Figure 6.4 Cross-sectional microstructure images for 10.0 kx magnification of splats and coatings produced with TiO$_{1.9}$ feedstock; Conv-0 (a), Cas-0 (b), Cas-9 (c) and HVOF (d). (e) Enlarged splat microstructure of splat Cas-0 where boxed in (b). (f) Porosity of TiO$_{2-x}$ coatings calculated by image analysis as a function of product of process temperature and velocity.

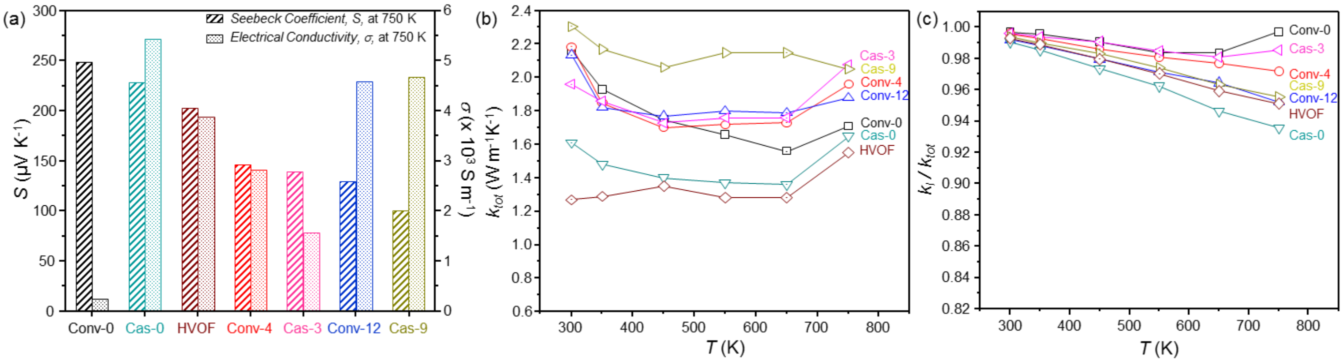

Figure 6.5 Thermoelectric properties of TiO_{2-x} coatings produced with $TiO_{1.9}$ feedstock. (a) Seebeck coefficients (s) and electrical conductivities (σ) of TiO_{2-x} coatings measured at 750 K. (b) Temperature dependent thermal conductivity of TiO_{2-x} coatings. (c) Temperature dependent k_l / k_{tot} of TiO_{2-x} coatings. k_l is obtained using $k_l = k_{tot} - L\sigma T$ where L is Lorenz number, 2.6 x 10^{-8} V^2 K^{-2}.[66]

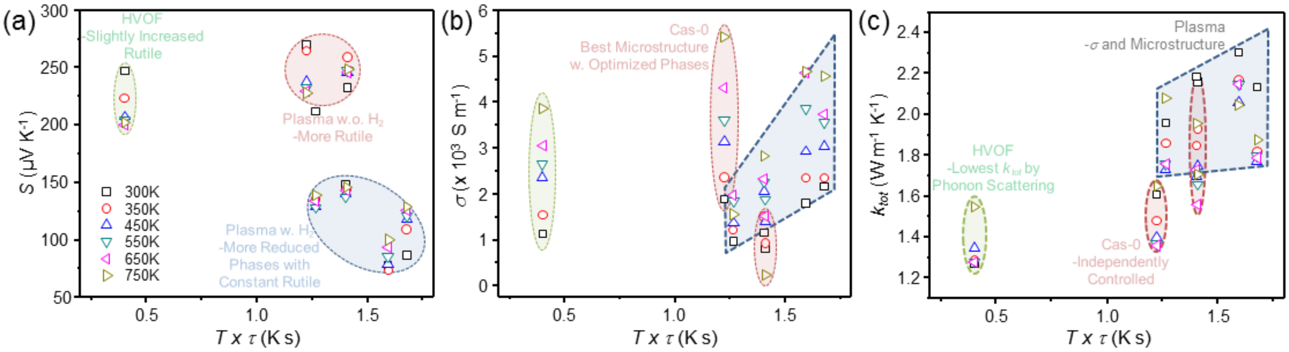

Figure 6.6 Process effect on thermoelectric properties of TiO_{2-x} coatings.

(a) Temperature dependent Seebeck coefficient, (b) temperature dependent electrical conductivity, and (c) temperature dependent thermal conductivity as a function of thermal exposure during the thermal spray process.

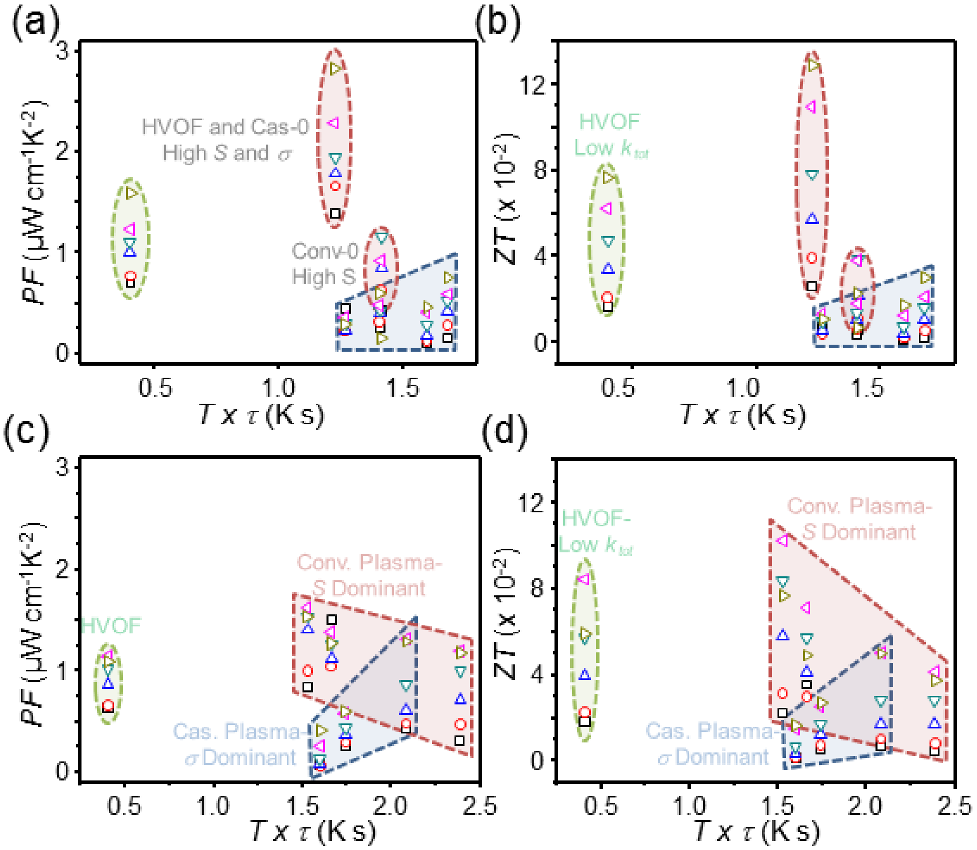

Figure 6.7 Process effects on TE power factor (*PF*) (a) and (c) and figure of merit (*ZT*) (b) and (d) as a function of product of temperature (*T*) and residential time (*t*) during the spray process of TiO_{2-x} coatings produce with and $TiO_{1.9}$ and $TiO_{1.7}$ feedstocks, respectively.

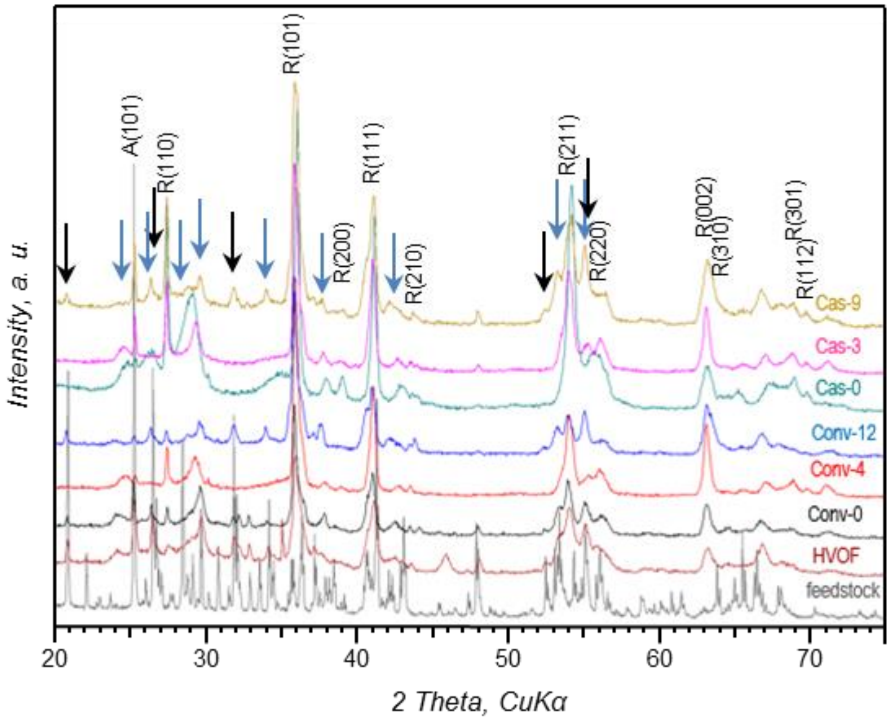

Figure 6.8 Powder XRD patterns of $TiO_{1.7}$ feedstock powder and surfaces of the as-sprayed coatings (R = Rutile, A = anatase, Arrows indicate Ti_4O_7 (Black) and Ti_8O_{15} (Blue) phases. The rest of reflections from Magneli phases (n = 3, 5, 6, 7, 9)).

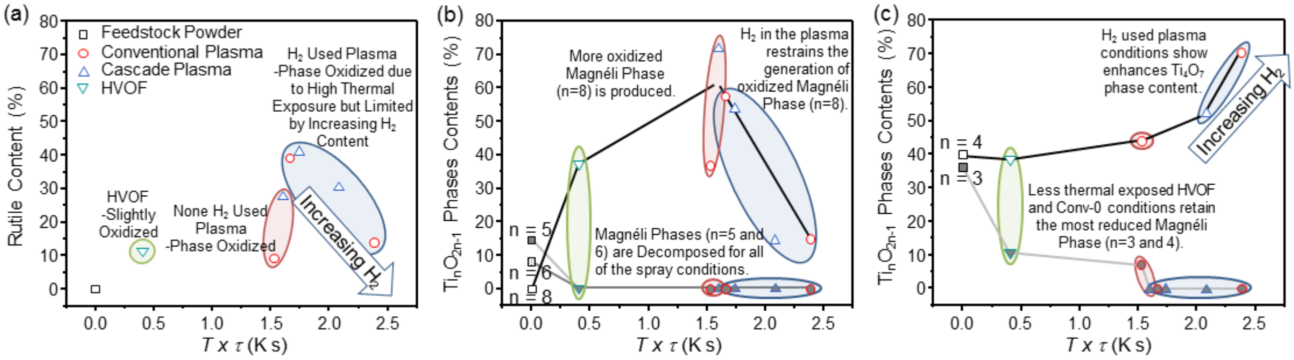

Figure 6.9 Process effect on phase contents in the TiO_{2-x} coatings produced with TiO1.7 feedstock. (a) Rutile, (b) Magnéli phases (n = 5, 6 and 8), and (c) Magnéli phases (n = 3 and 4) as a function of product of temperature (*T*) and residential time (*τ*) during the spray process.

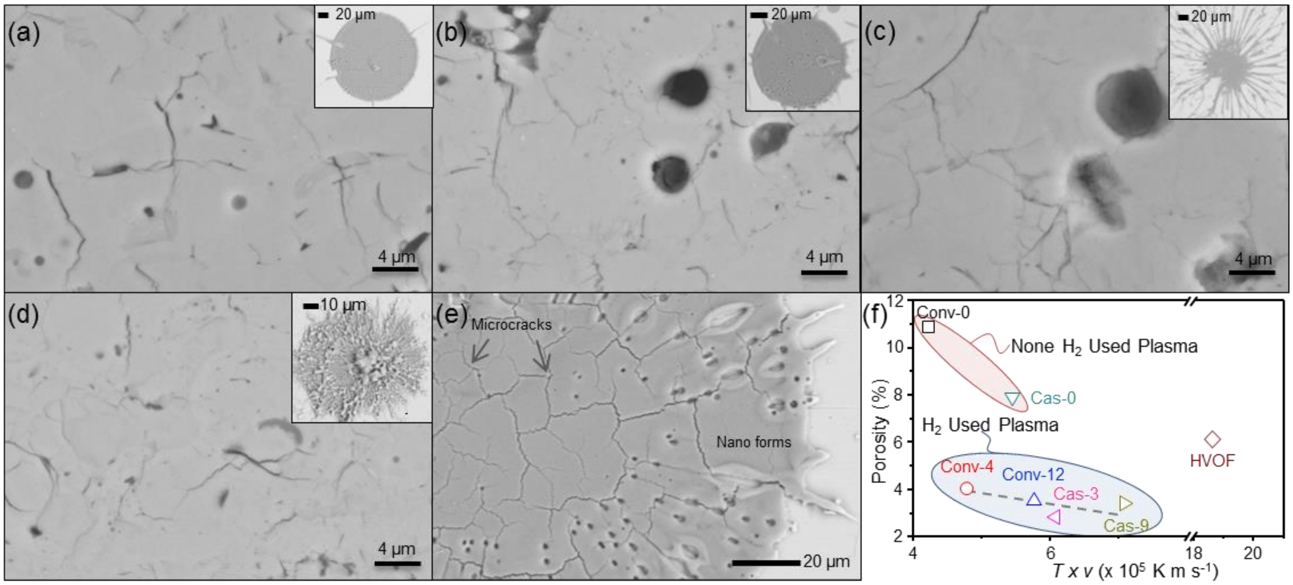

Figure 6.10 Cross-sectional microstructure images for 10.0 kx magnification of splats and coatings produced with $TiO_{1.7}$ feedstock; Conv-0 (a), Cas-0 (b), Cas-9 (c) and HVOF (d). (e) Enlarged splat microstructure of splat Conv-0. (f) Porosity of TiO_{2-x} coatings calculated by image analysis as a function of product of process temperature and velocity.

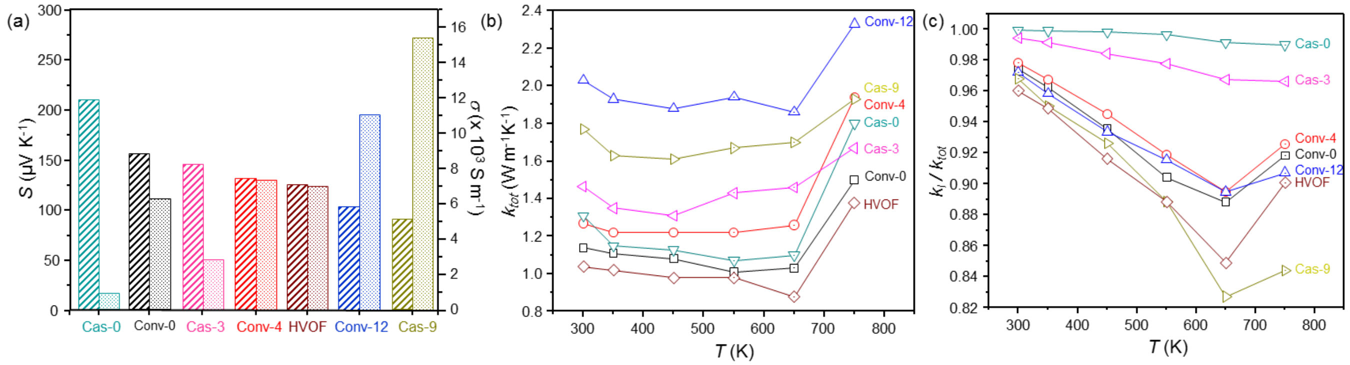

Figure 6.11 Thermoelectric Properties of TiO_{2-x} coatings produced with TiO1.7 feedstock. (a) Seebeck coefficients (s) and electrical conductivities (σ) of TiO_{2-x} coatings measured at 750 K. (b) Temperature dependent thermal conductivity of TiO_{2-x} coatings. (c) Temperature dependent k_l / k_{tot} of TiO_{2-x} coatings. k_l is obtained using $k_l = k_{tot} - L\sigma T$ where L is Lorenz number, 2.6 x 10^{-8} V^2 K^{-2}.[66]

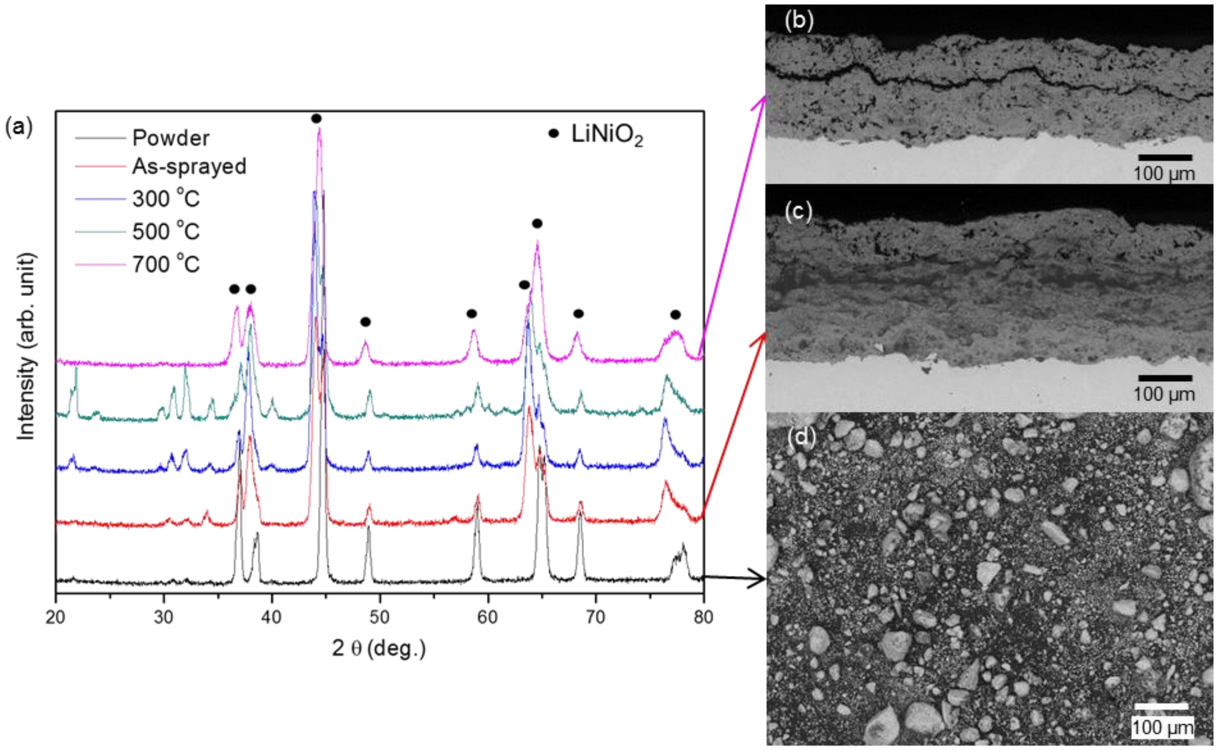

Figure 8.1 (a) XRD patterns of feedstock (black), as-sprayed (red), and annealed coatings at 300 °C (blue), 500 °C (green), and 700 °C (magenta) of $LiNi_{0.8}Co_{0.15}Al_{0.05}O_2$. Electron micrographs of annealed coating at 700 °C (b), as-sprayed coating (c) and feedstock (d) of $LiNi_{0.8}Co_{0.15}Al_{0.05}O_2$.

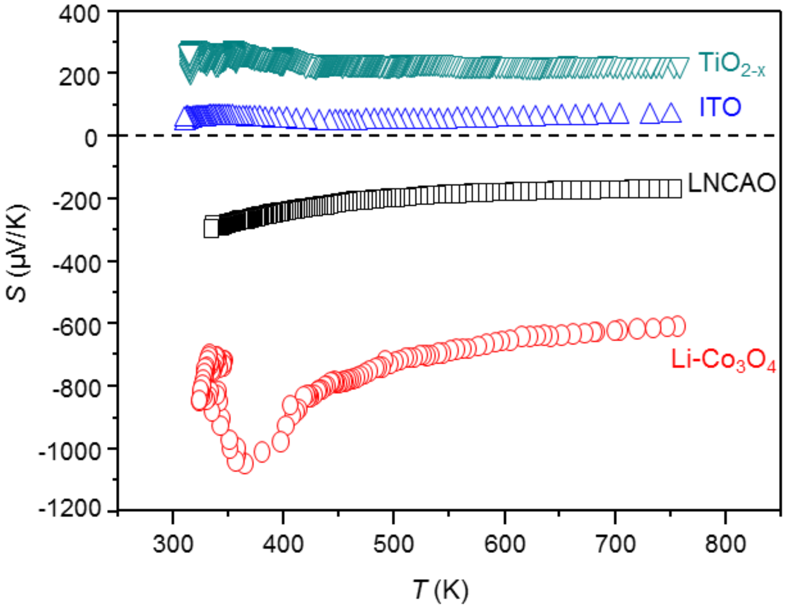

Figure 8.2 Comparisons of Seebeck coefficients as a function of temperature of $LiNi_{0.8}Co_{0.15}Al_{0.05}O_2$ (LNCAO), Li-doped Co_3O_4, and ITO coatings with respect to the optimized TiO_{2-x} coating.

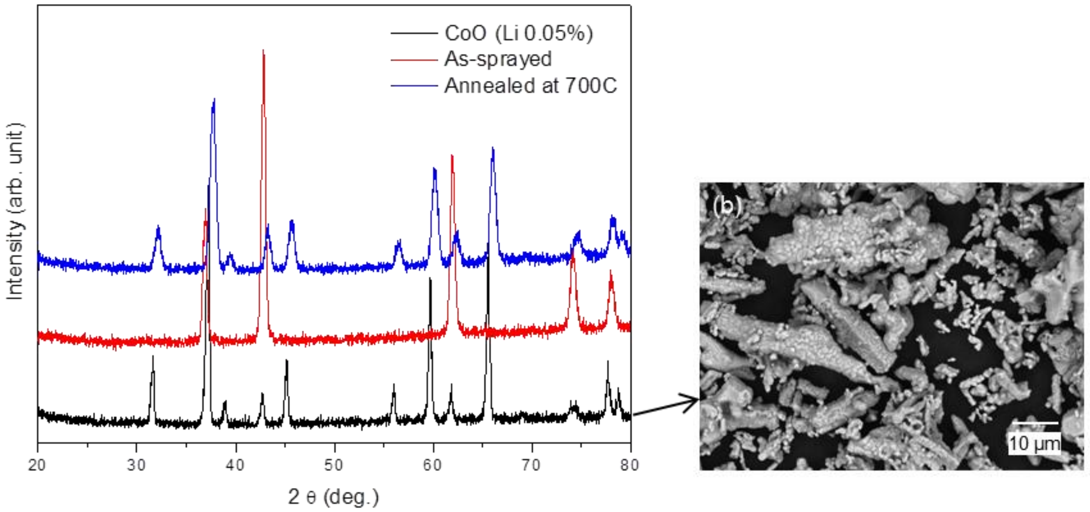

Figure 8.3 (a) XRD patterns of feedstock (black), as-sprayed (red), and annealed coatings at 700 °C (blue) of Li-doped CoO_2. (b) Electron micrograph of 0.05% Li-doped CoO_2 feedstock.

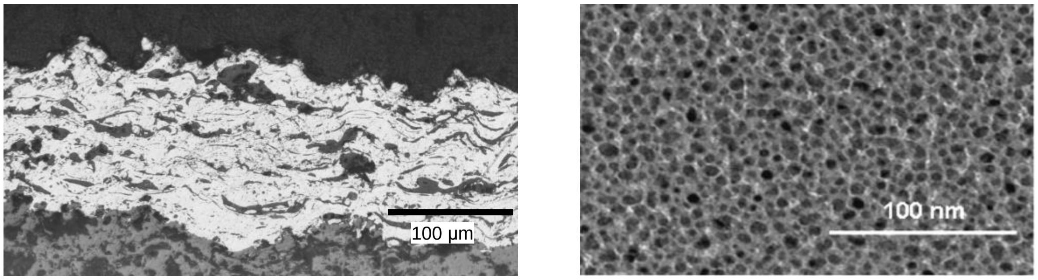

Figure 8.4 (a) Cross-sectional optical micrograph of as-sprayed NiCoCrAlY/Al_2O_3. (b) TEM micrograph of an as-deposited NiCoCrAlY/alumina nanocomposite. Note the black phase is Al2O3 and the lighter phase is NiCoCrAlY. (Courtesy of Otto J. Gregory et. al. Thin Solid Films 518 (2010) 6093–6098.)

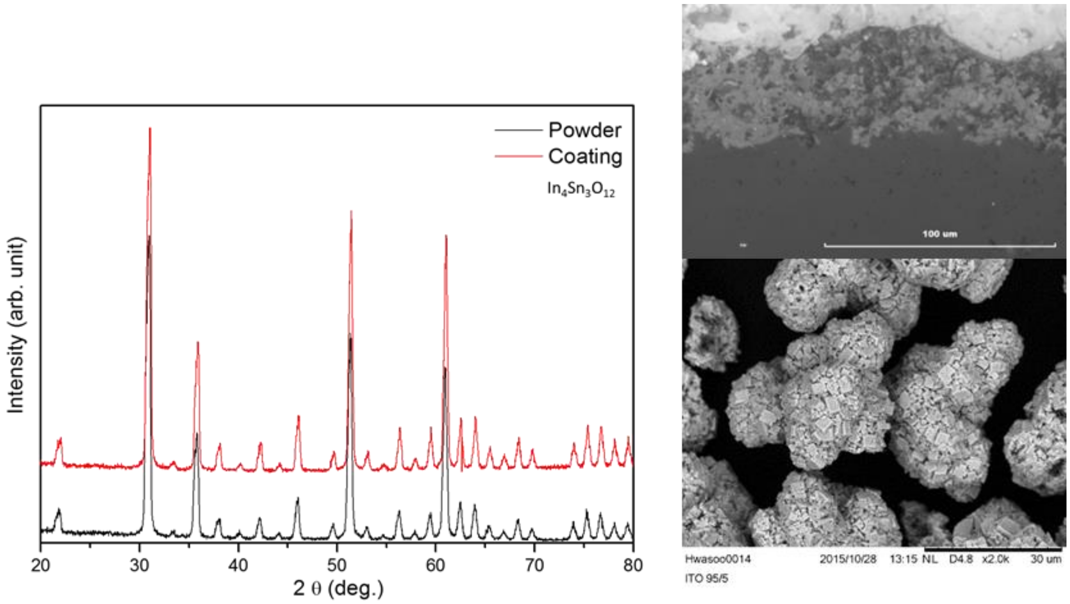

Figure 8.5 (a) XRD patterns of feedstock (black) and as-sprayed (red) of ITO. (b) Electron micrograph of ITO feedstock.

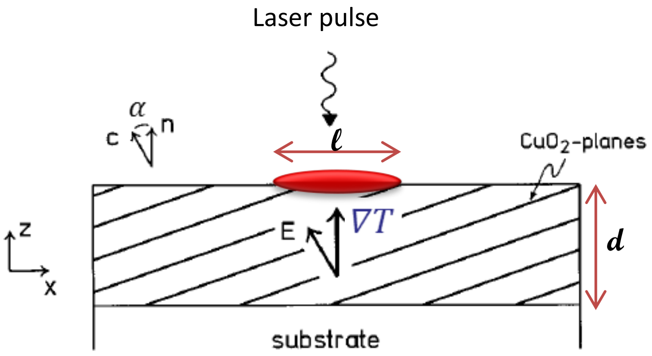

Figure 8.6 Schematic illustration of off-diagonal thermoelectric power generation.

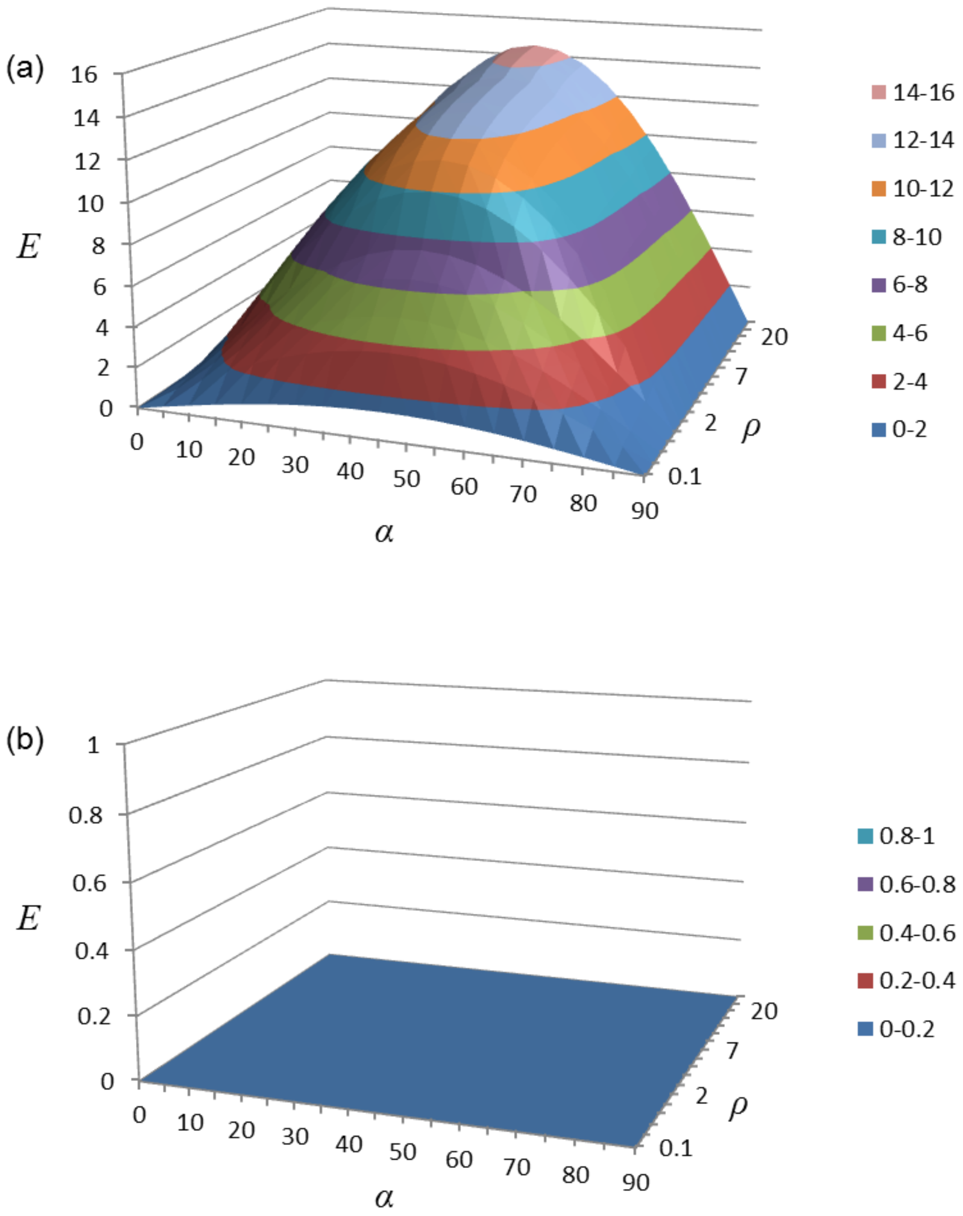

Figure 8.7 Schematic illustrations of torch angle effects on the morphology of splats. (a) Impact angles of 90 deg and (b) 30 deg.
(Courtesy of ref. 146)

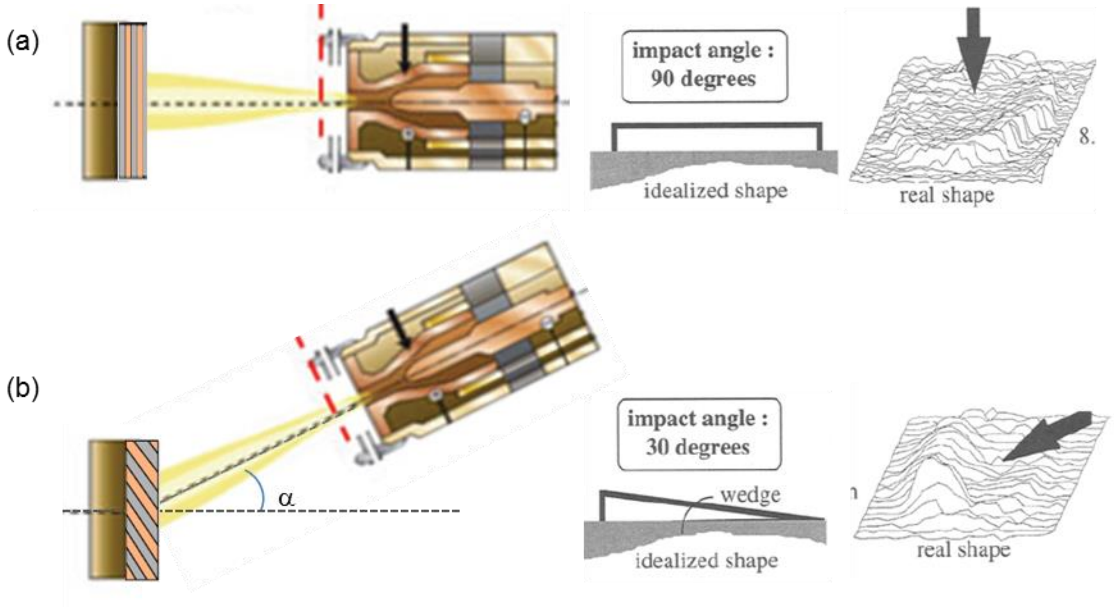

Figure 8.8 Schematic illustrations of torch angle effects on the morphology of splats. (a) Impact angles of 90 deg and (b) 30 deg.
(Courtesy of ref. 146)

Impact Angle (deg)	Optical Micrograph	Morphology of Splat	Profile of Cross Section
90	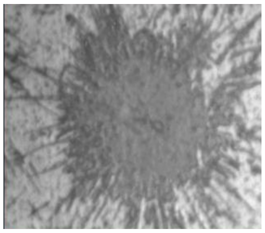	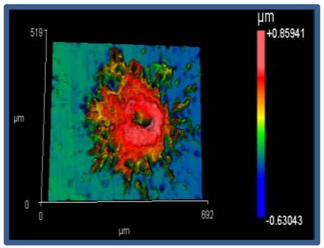	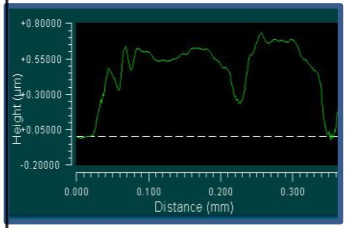
60	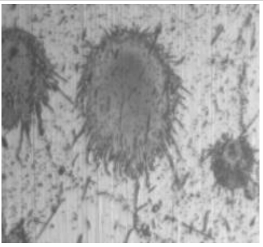	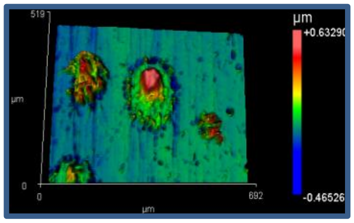	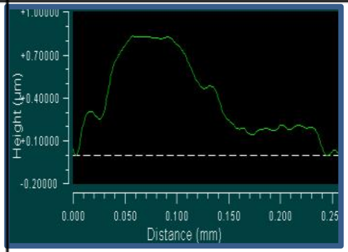
45	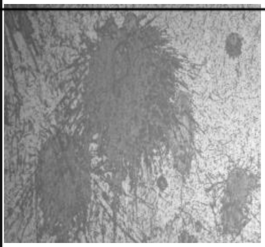	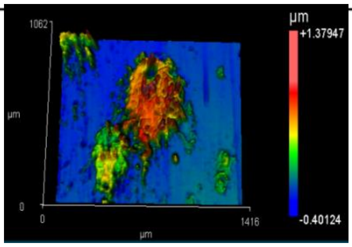	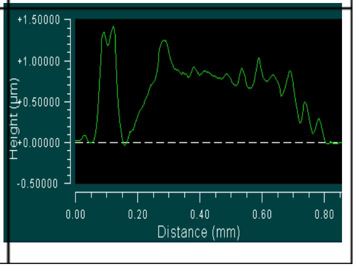

Figure 8.9 Splat morphologies and cross-sectional profiles of HVOF processed a LSM-TiO_2 mixture (50:50 v/v) with respect to the various torch angles (90, 60 and 45 degrees).

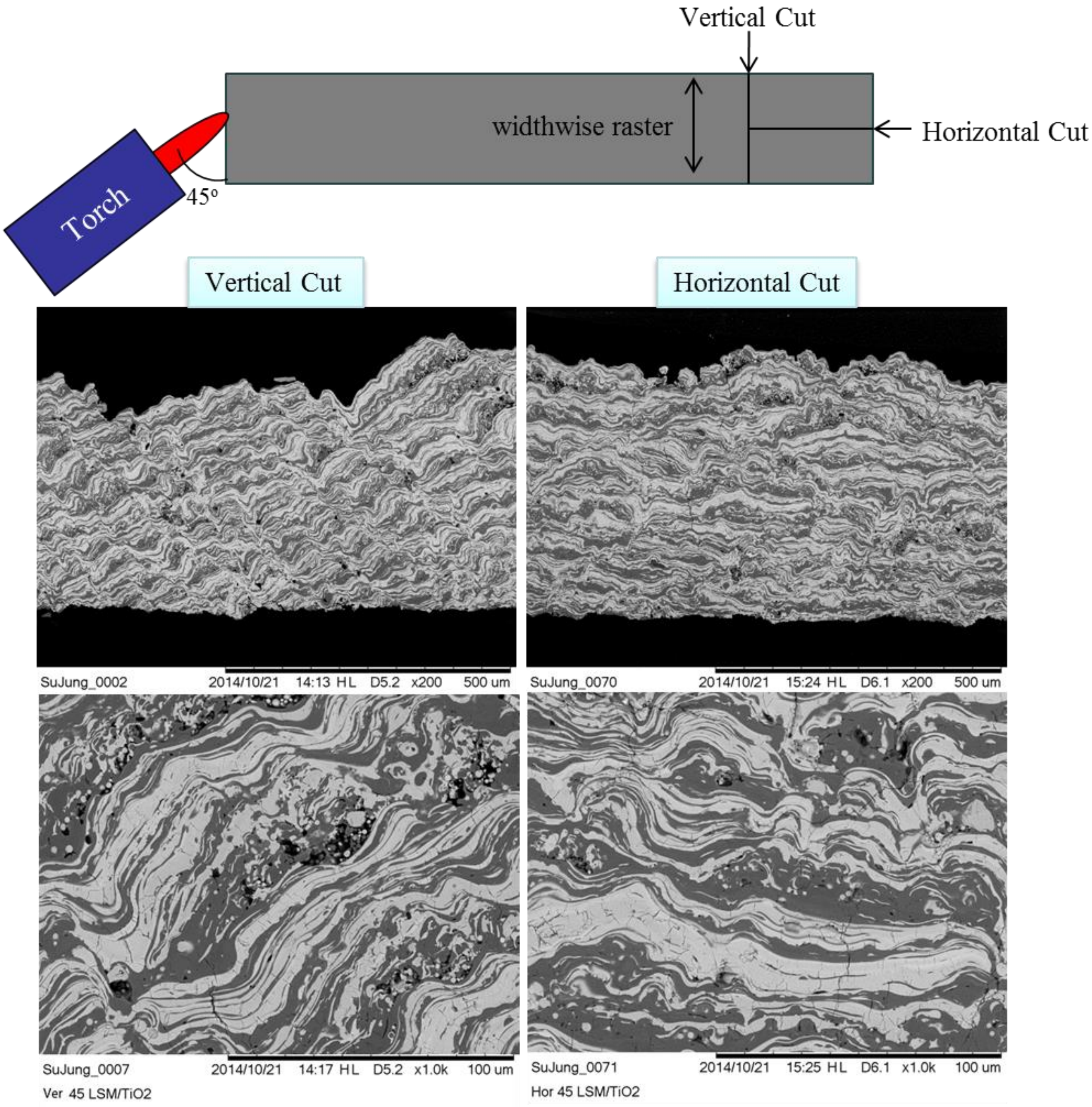

Figure 8.10 Electron micrographs of plasma sprayed LSM (bright)-TiO_2 (dark) (50:50 v/v) coating with 45 deg torch angle, cross-sectioned by vertical and horizontal directions.

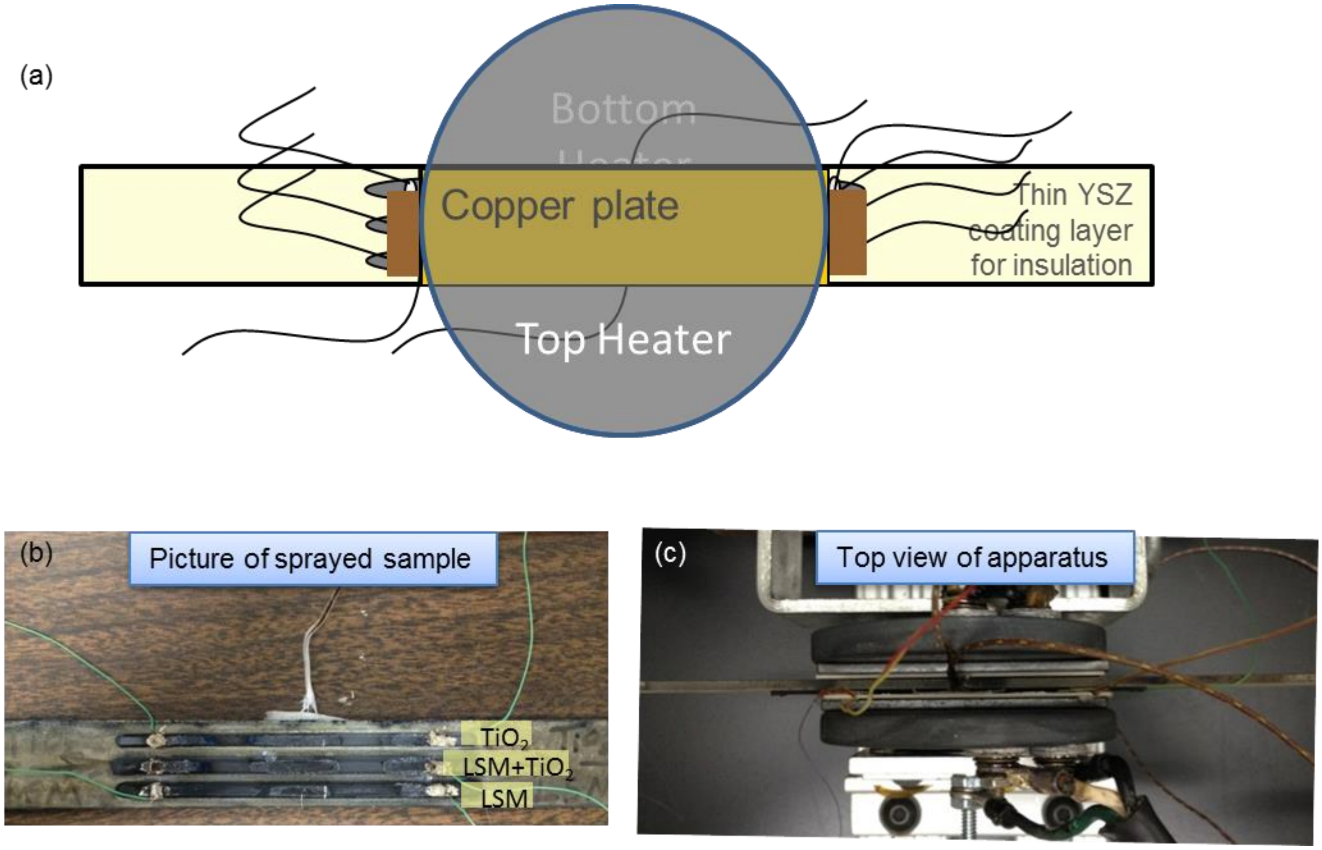

Figure 8.11 (a) Design of the Seebeck voltage measurements. (b) Picture of the actual sprayed coatings for the measurement. (c) Top view of the Seebeck voltage measurement set up.

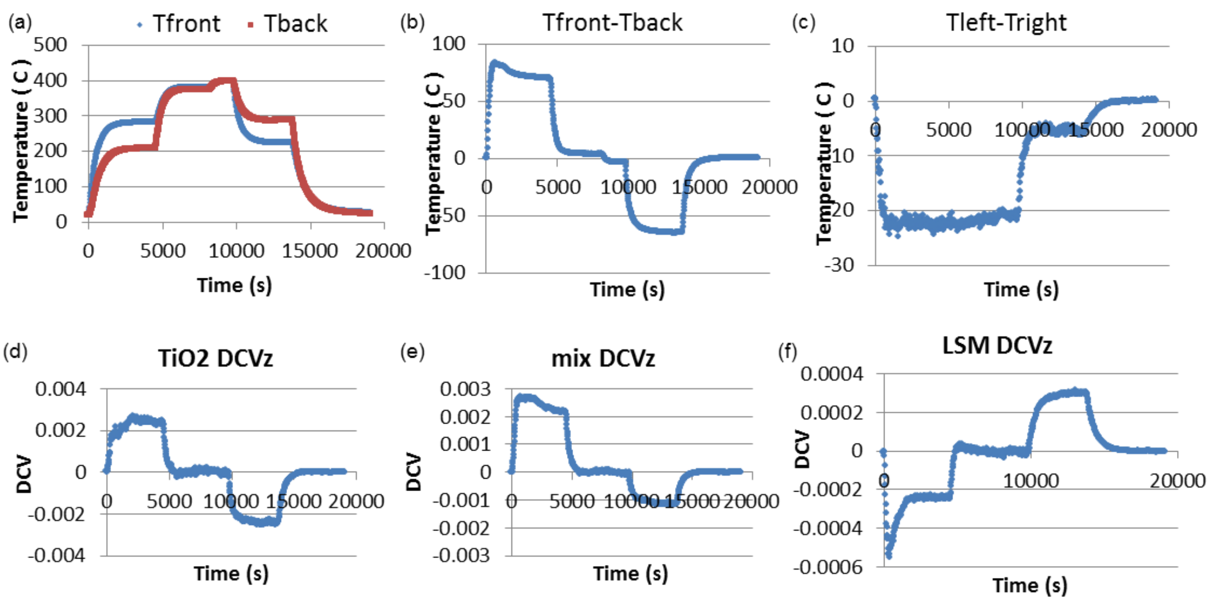

Figure 8.12 Transverse Seebeck voltage measurements of TiO_2 -LSM (50:50 v/v) mixture coating with 45 deg impact angle.

(a) Temperature at top and bottom (substrate) of the coating. (b) Temperature difference of the top and bottom of the coating. (c) Temperature difference of left and right sides of the coating. (d) Transverse voltage output of TiO_2 only coating. (e) Transverse voltage output of TiO_2 -LSM coating. (f) Transverse voltage output of LSM only coating.

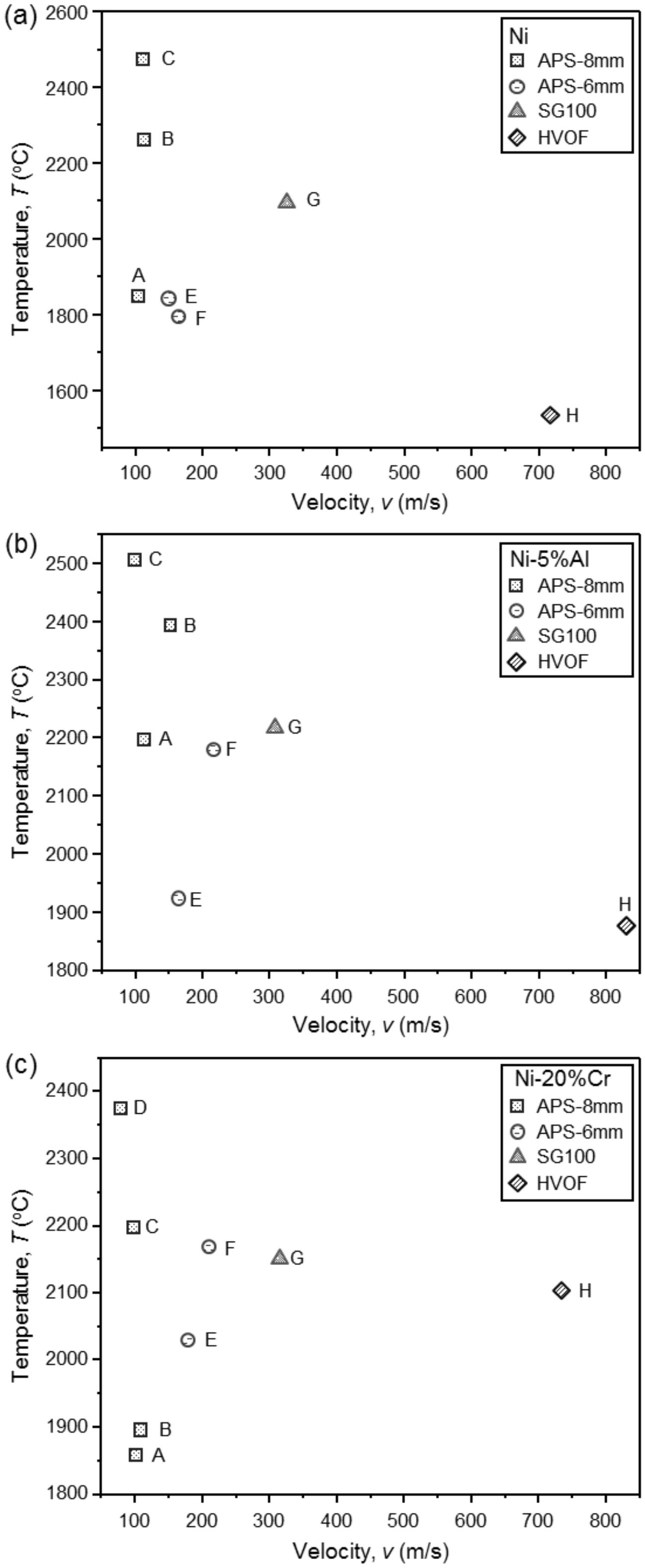

Figure 8.13 First-order *T*-*v* process map of (a) Ni, (b) Ni-5%Al, and (c) Ni-20%Cr coatings with torch hardware information.

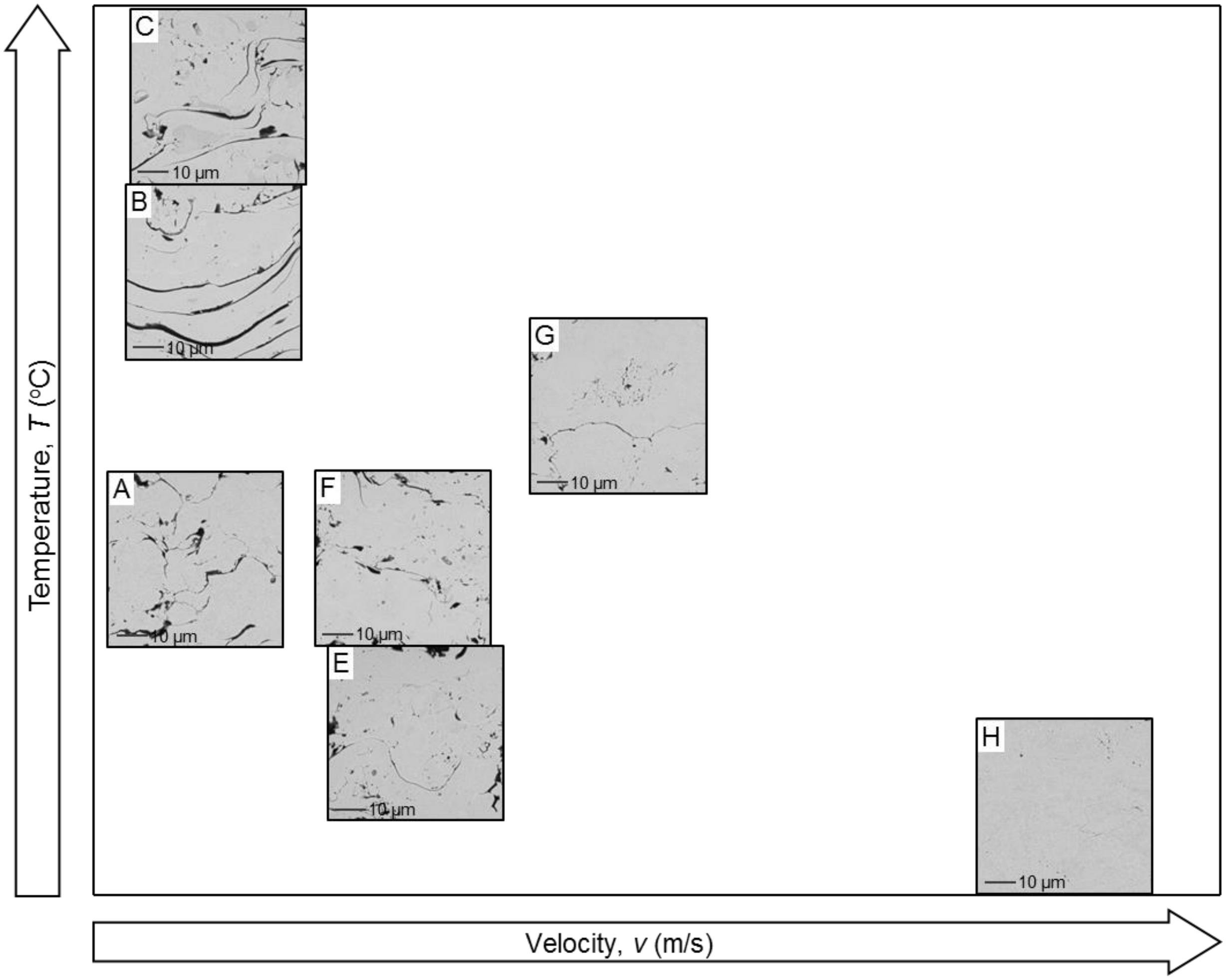

Figure 8.14 Cross-sectional SEM images of as-sprayed Ni coatings with 2.0k magnification.

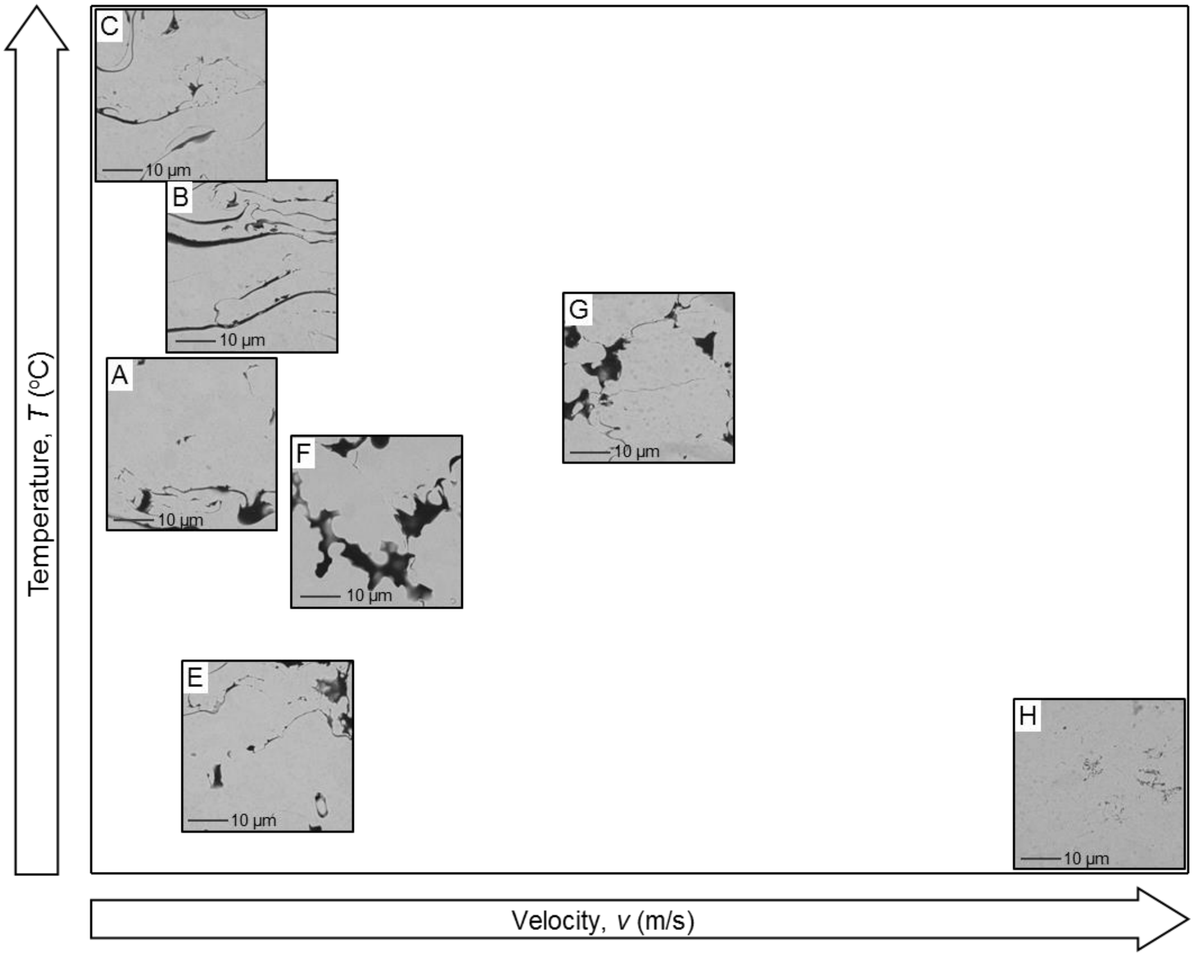

Figure 8.15. Cross-sectional SEM images of as-sprayed Ni-5%Al coatings with 2.0k magnification.

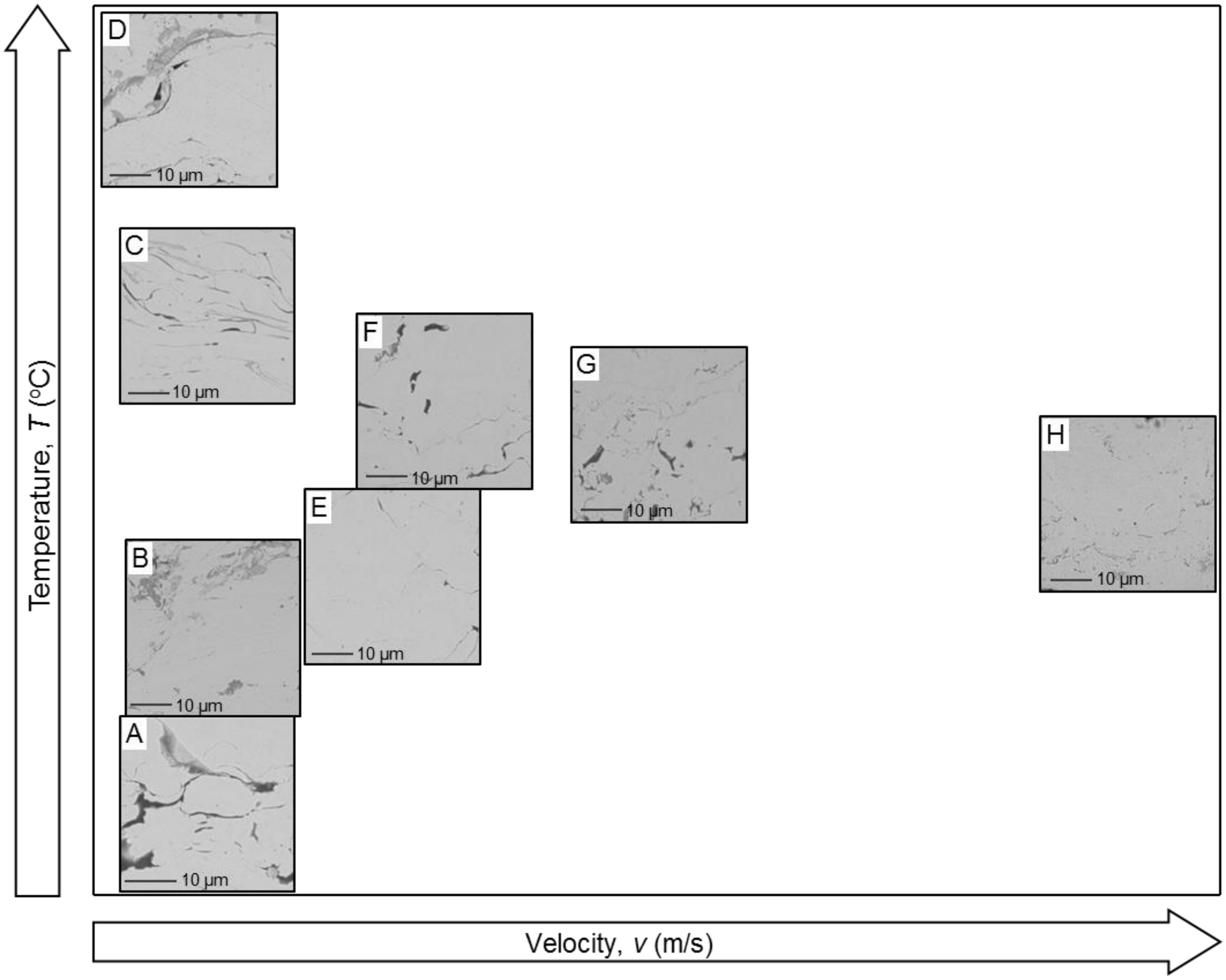

Figure 8.16 Cross-sectional SEM images of as-sprayed Ni-20%Cr coatings with 2.0k magnification.

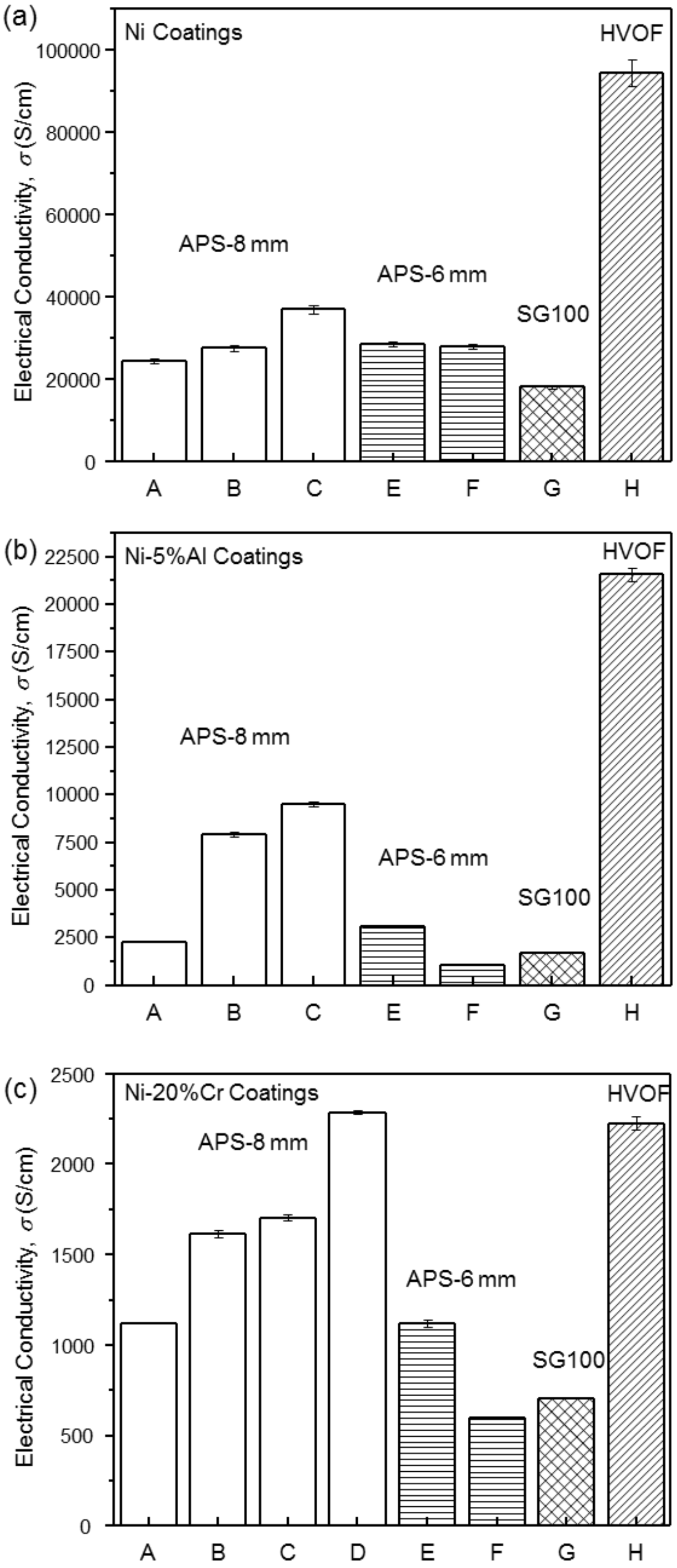

Figure 8.17 In-plane electrical conductivity of 100 μm thick (a) Ni, (b) Ni-5%Al, and (c) Ni-20%Cr coatings with torch hardware information.

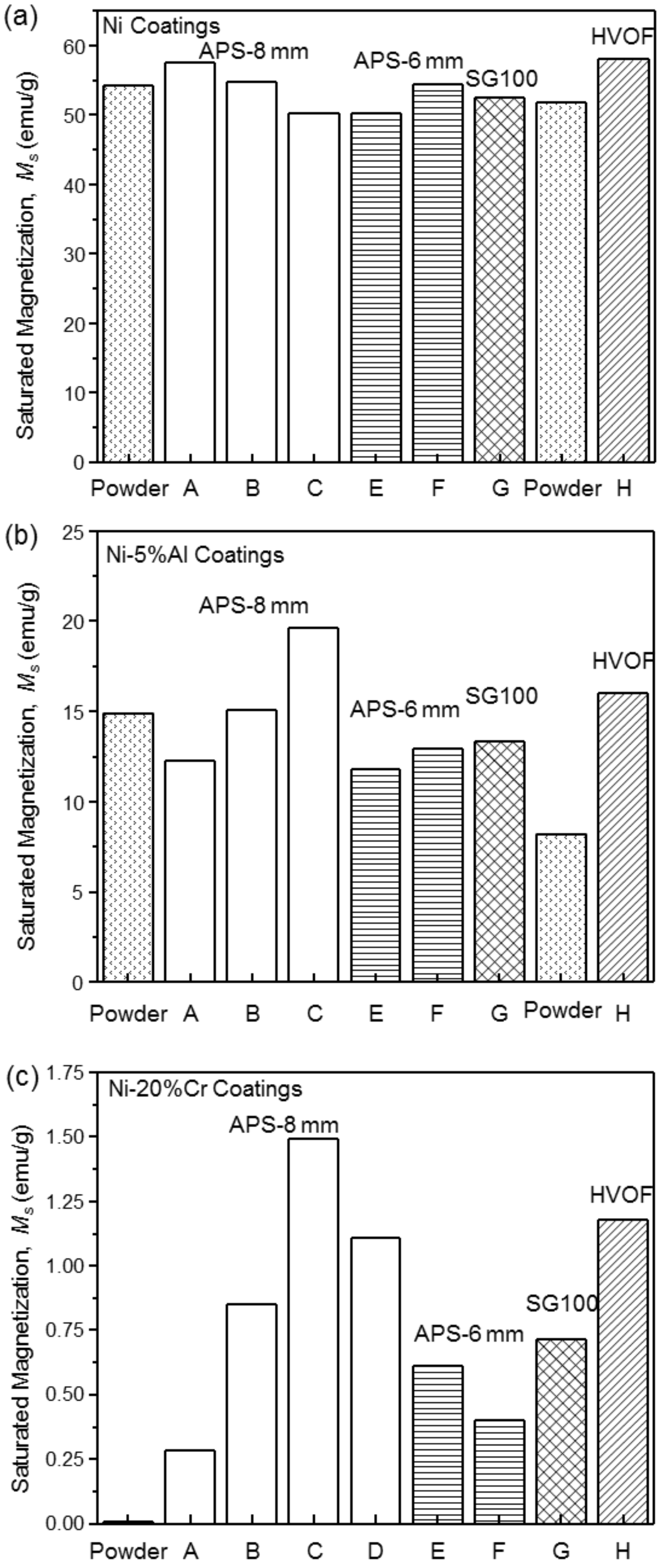

Figure 8.18 Saturated magnetization of (a) Ni, (b) Ni-5%Al, and (c) Ni-20%Cr coatings and feedstock powders with torch hardware information.

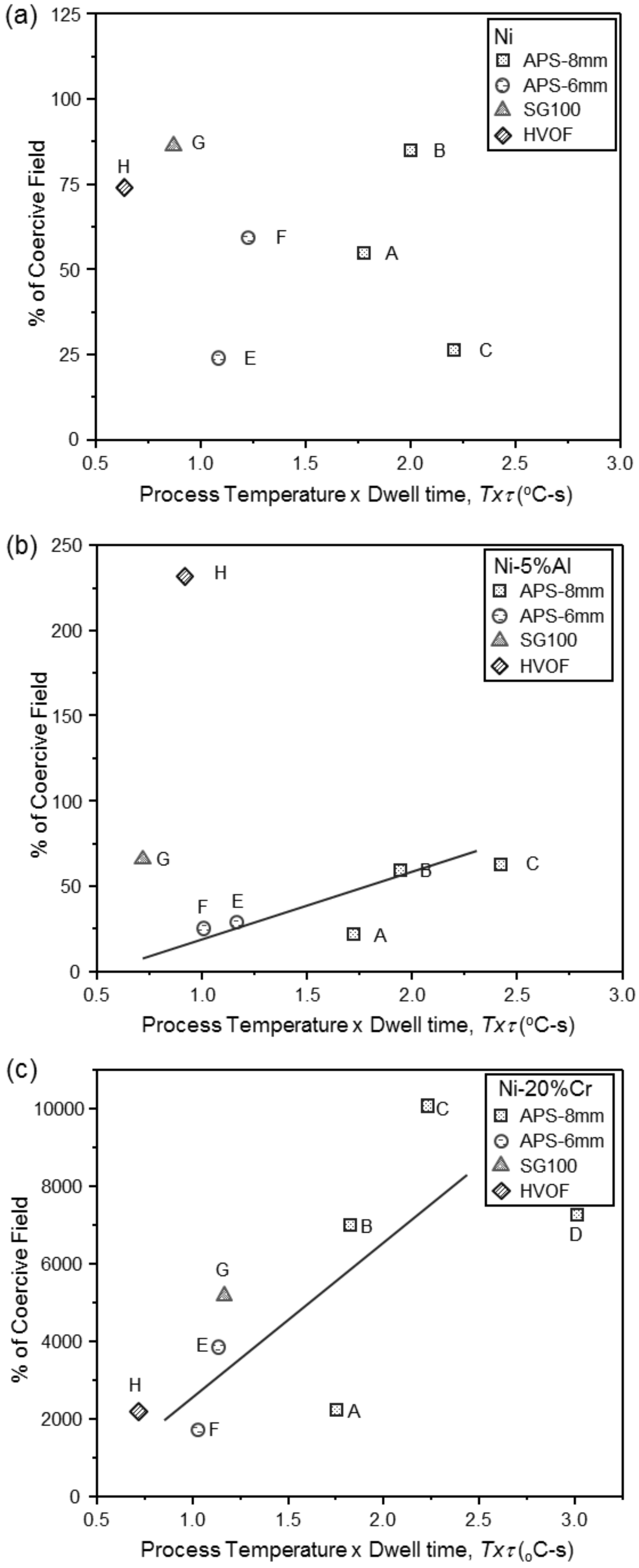

Figure 8.19 Percentage of coercive field of (a) Ni, (b) Ni-5%Al, and (c) Ni-20%Cr coatings and feedstock powders with torch hardware information.

Table 1.1 Functional oxides; overview of materials, functional requirements and processings.

Functional Classification	Requirements	Types of Materials	Applications	Processing
Dielectric Materials	High dielectric constant (κ) Low dissipation factor High permittivity Resistance to ionization	SiO_2, ZrO_2, HfO_2, TiO_2, MgO, Cr_2O_3, Al_2O_3, MgO-3Al_2O_3, Mg(Sr)TiO_3, Ba(Sr)TiO_3	Capacitor, Dielectric resonator, Dielectric resonator antenna, Gate in MOSFET	Thin-film deposition techniques: Molecular beam epitaxy (MBE), Hydride vapor phase epitaxy (HVPE), Liquid phase epitaxy (LPE), Metal-organic molecular beam epitaxy (MOMBE), Atomic layer deposition (ALD), Pulsed laser deposition (PLD), Chemical vapor deposition (CVD), Physical vapor deposition (PVD), Sol-gel, Sputtering. Thick-film deposition techniques: Thermal spray, Pressing and sintering, Ink-jet printing, Screen printing, Dip coating, Tape casting, Spark plasma sintering, Electrophoretic deposition.
Semiconducting Materials	High-purity (no unintentional impurities), Crystalline or amorphous (transparent applications), Controlled doping and oxygen vacancies for concentration and location	n-types: TiO_{2-x}, ZnO, In_2O_3, SnO_2, Ga_2O_3, ITO, ZTO, IZO, GIZO, IZTO, IGO, IHZO p-types: Cobaltites, La(Sr)MnO_3, $Mn_{2-x}Co_xO_4$, CuO, Cu_2O, $CuMO_2$ (M = Al, Ga, In, Y, Sc, La, Zn), SnO	Electronic components (Microprocessors, Microcontrollers, Static RAM, Digital logic circuits), Transparent electronics, Image sensors, Data converters, Highly integrated transceivers, Energy harvesting (Batteries, Solar cells, SOFCs, Thermoelectrics)	
Superconducting Materials	High current density (J_c) Higher upper critical field (H_{c2}) Minimum mass and critical current anisotropy	$YBa_2Cu_3O_{7-x}$, $YBa_2Cu_4O_y$, $Y_2Ba_4Cu_7O_y$ (YBCO), $La_{2-x}Ba_xCuO_4$ (LBCO), $Bi_2Sr_2CaCu_2O_{8+x}$ (BSCCO)	Electromagnets (MRI, NMR, Mass spectrometers, particle accelerator), RF and microwave filters, SQUIDs (superconducting quantum interference devices), Coated Conductor	
Magnetic Materials	Large M_R Small H_C Small conductivity (for motors, generators, electromagnets, signal transfer) Low w Linear M-H curve (for transformer)	Co, Mg, Mn, Ni, Zn-ferrites, Y_2O_3-Fe_2O_3 (Yttrium iron garnet, YIG)	Motors, Generators, Electromagnet, Navigation, Transformer, Transmitter, Transducer, Telecommunication devices, Microwave, Data storage	
Phosphors	Compositional homogeneity Phase stability Appropriate dopant concentration	Y_2O_3-Al_2O_3 (Yttrium aluminum garnet, YAG), YIG, YIG-YAG, Y_2O_3-TiO_2-ZrO_2, Y_2O_3, Eu-doped Y_2O_3, Eu/Cr-doped YAG, Zinc silicates	Sensor, Laser, Phosphor in cathode ray tubes, Scintillator in white light-emitting diodes, Thermometer	

Table 1.2 Overview of materials and requirements for SOFC cell components.
(Courtesy of P. Holtappels, U. Vogt and T. Graule. Advanced Engineering Materials vol. 7 (2005) 292-302.)

Component	Function	Requirements	Materials
Anode	Electrocatalytic activity $CO + H_2O \rightarrow H_2 + CO_2$ $2H_2 + 2O^{2-} \rightarrow 4e^- + 2H_2O$ Gas transport Current pick up	Long triple-phase boundary Activity for oxygen surface exchange Porosity Electronic conductivity Redox stability	Cermets Ni-$Y_{0.15}Zr_{0.85}O_{1.93}$ (Ni-YSZ)
Electrolyte	Oxygen ion transport Electronic insulator	Oxygen ion conductivity Gas tightness Mechanical stability fully dense microstructure thin layer (40 µm)	$Y_{0.15}Zr_{0.85}O_{1.93}$ (YSZ) doped cerium oxide doped bismuth oxide
Cathode	$O_2(g) + 4e^- \rightarrow 2O^{2-}$ Gas transport Current pick up	Long triple-phase boundary Activity for oxygen surface exchange Porosity Electronic conductivity	Perovskite $La_{1-x}Sr_xMnO_3$ (LSM) $La_{1-x}Sr_xCo_{1-y}Fe_yO_3$ (LSCF) $La_{1-x}Sr_xFeO_3$ (LSF)
Interconnect	Connect single cells Electrical current collection	100% electrical conductivity No porosity Inertness of electrode materials	$LaCrO_3$ (above 1000 °C) Ni based alloy (Inconel 600) (900 - 1000 °C) Ferritic steels (at 800°C) Stainless steels (below 700°C)

Table 3.1 Plasma Spray parameters for deposition of YSZ, LSM and MCO coatings. Temperature and velocity of particles are measured via Accuraspray particle diagnostics sensor. [a]Mean particle velocity and temperature of LSM. [b]Mean particle velocity and temperature of MCO. [c]Helium is used as secondary gas instead of hydrogen in this particle torch-parameter configuration.

Condition-Torch & Nozzle Size	Feed Rate (g min^{-1})	Ar flow (L min^{-1})	H_2 flow (L min^{-1})	Current (A)	Power (kW)	Mean Particle Velocity (m s^{-1})	Mean Particle Temperature (°C)
YSZ-F4 8mm	30	47.5	6	550	35.5	173	2840
A-F4 8mm	30	35	10	650	42.9	139 [a] 127[b]	2276 [a] 2281 [b]
B-F4 8mm	30	60	6	700	47.3	198 [a] 212 [b]	2425 [a] 2318 [b]
C-F4 8mm	30	60	3	400	23.5	171 [a] 154 [b]	2192 [a] 2087 [b]
D-F4 6mm	30	60	3	550	29.7	242 [a] 345 [b]	2137 [a] 2251 [b]
E-SG100	17	90	35[c]	590	39.2	350[a] 580[b]	1725[a] 2690[b]

Table 3.2 Thermal spray process parameters of for deposition of $TiO_{1.9}$ and $TiO_{1.7}$ coatings.

Torch Hardware		Powder Feed Rate (g/min)	Ar Flow (L/min)	Oxygen Flow (L/min)	H_2 Flow (L/min)	Carrier Gas Flow (L/min)	Current (A)
GUN	Nozzle Size (mm)						
F4MB-XL	8	30	45.0		0,4,12	5 (Ar)	550
SinplexPro™	9	30	45.0		0,3,9	5 (Ar)	380
HV 2000		15		236.1	566.5	21.2 (N_2)	

Table 4.1 Chemical compositions of ferritic steel alloys for SOFC interconnect.

Alloy & Supplier	E-brite ATI	Crofer 22 APU Thyssenkrupp VDM	ZMG232 Hitachi Metals	430 Outokumpu	441HP™ ATI
Cr	25.00-27.50	20.00-24.00	22.00	16.00-18.00	17.50-19.50
Mo	0.75-1.50				
Ni+Cu	0.50				
Ni	0.50		0.26		1.00
Si	0.40	0.50			1.00
Mn	0.40	0.30-0.80	0.50	1.00	1.00
Cb	0.05-0.20				0.30-0.90
Cu	0.20	0.50			
P	0.02	0.05			0.04
S	0.02	0.02		1.00	0.03
N	0.015				0.03
C	0.01	0.03	0.02	0.12	0.03
Al		0.50	0.21		0.05
Ti		0.03-0.20			0.10-0.50
La		0.04-0.20	0.04		
Zr			0.22		
Fe	Balanced	Balanced	Balanced	Balanced	Balanced
CTE at 800 °C ($\times 10^{-6}$ °C^{-1})	9.9	11.9	11.8	11.4	12.4

Table 4.2 Chemical analysis results of LSM feedstock powder and coatings via ICP-OES.

Sample	La	Mn	Sr	Total of other trace elements
Powder	46.8	25.2	7.8	0.1
A	53.09	15.88	7.98	0.09
B	50.61	20.11	7.70	0.16
C	46.37	23.31	7.53	0.09
D	48.88	23.99	7.21	0.07
E	45.84	24.40	7.40	0.09

Table 4.3 Estimated activation energies (E_a) of coatings A through E.

	E_a (eV)		
	As-sprayed (Up to 200 °C annealing)	After oxygen recovery (Up to 600°C annealing)	After 24 hours staying at 800 °C
A	0.202	0.184	0.155
B	0.187	0.171	0.130
C	0.229	0.167	0.127
D	0.207	0.152	0.122
E	0.190	0.150	0.112

Table 5.1 Refined lattice parameters of phases present in annealed A-E coatings; specifically for (Co,Mn)O the refined lattice parameters for as-sprayed coatings are given in parentheses.

Coating	CoO	Co_2MnO_4	$CoMn_2O_4$	
	a ± Δa (Å)	a ± Δa (Å)	a ± Δa (Å)	c ± Δc (Å)
A	4.336 ± 0.001	8.167 ± 0.004	5.756 ± 0.003	9.195 ± 0.007
B	4.328 ± 0.001	8.162 ± 0.004	5.755 ± 0.003	9.175 ± 0.006
C	4.306 ± 0.001	8.144 ± 0.004	5.750 ± 0.003	9.157 ± 0.006
D	4.296 ± 0.001	8.167 ± 0.003	5.734 ± 0.003	9.159 ± 0.005
E	4.296 ± 0.002	8.182 ± 0.003	5.736 ± 0.003	9.162 ± 0.005

Table 5.2 Phases’ quantity and lattice parameter of (Co,Mn)O changes of D condition MCO coating by analyzing temperature dependent XRD results from 130 to 200 °C via Rietveld Analysis.

T (°C)	Phases’ Quantities (%)			Lattice Parameter of CoO, a (Å)
	CoO	$CoMn_2O_4$	Co_2MnO_4	
130	48.75	8.75	42.49	4.285931
140	47.55	8.04	44.4	4.286651
150	47.71	10.14	42.15	4.286649
160	45.38	10.17	44.46	4.288496
170	47.24	11.22	39.54	4.288941
180	45.05	6.77	48.18	4.291645
190	48.42	8.76	42.82	4.291482
200	48.37	9.91	41.72	4.292028

Table 5.3 Estimated activation energy (E_a) values of A through E coatings via calculating slope of cooling down curves in Arrhenius plot (Figure 5.10).

	A	B	C	D	E
E_a (eV)	0.53	0.47	0.64	0.54	0.40

Table 8.1 Plasma spray parameters for deposition of TE candidates.

Material	Torch Hardware		Powder Feed Rate (g/min)	Ar Flow (L/min)	H_2 Flow (L/min)	Carrier Gas Flow (L/min)	Current (A)	Power (KW)
	GUN	Nozzle Size (mm)						
$LiNi_{0.8}Co_{0.15}Al_{0.05}O_2$	F4MB-XL	8	30	45.0	6	4 (Ar)	550	39.5
Li doped Co_3O_4	SinplexPro^{TM}	9	2	45.0	0	10 (Ar)	380	29.3
NiCoCrAlY/Al_2O_3	SinplexPro^{TM}	9		45.0	3	4	380	
ITO	F4MB-XL	8	30	40.0	6	5	550	39.9

Table 8.2 Comparisons of coefficients of thermal expansion of TE candidates.

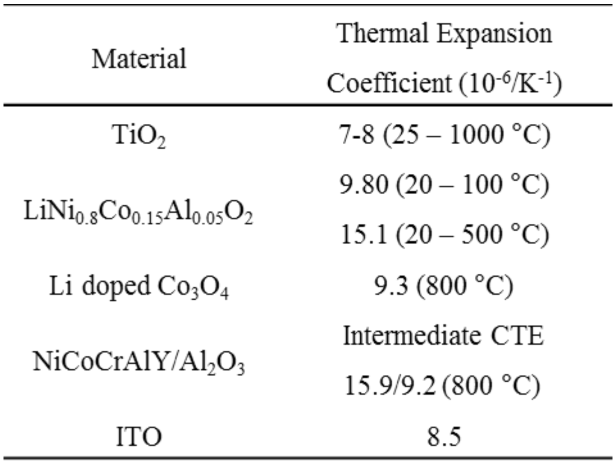

Material	Thermal Expansion Coefficient (10^{-6}/K^{-1})
TiO_2	7-8 (25 – 1000 °C)
$LiNi_{0.8}Co_{0.15}Al_{0.05}O_2$	9.80 (20 – 100 °C)
	15.1 (20 – 500 °C)
Li doped Co_3O_4	9.3 (800 °C)
NiCoCrAlY/Al_2O_3	Intermediate CTE 15.9/9.2 (800 °C)
ITO	8.5

Table 8.3 Transport data of the possible candidates for the transverse thermoelectric materials.

Material	Seebeck Coefficient (μV/K)	Electrical Conductivity (S/m)	Thermal Conductivity (W/mK)
Al	-1.66	4×10^7	232
Cu	1.7	5.9×10^7	400
Constantan	-37	0.2×10^7	19.5
Chromel	22	0.14×10^7	19
Ni	-15	0.625×10^7	51
Si	1500	100	156

Table 8.4 Spray parameters for deposition of alumina, Ni, Ni-5%Al and Ni-20%Cr coatings. [a]Helium is used as secondary gas instead of hydrogen in this particle torch-parameter configuration.

Condition-Torch Hardware	Feed Rate (g/min)	Ar flow (L/min)	H_2 flow (L/min)	Current (A)	Power (kW)
Alumina-F4 8mm nozzle	30	60	4	550	34.4
A-F4 8mm nozzle	15	80	2	450	25.0
B-F4 8mm nozzle	15	70	4	500	31.1
C-F4 8mm nozzle	15	60	6	550	35.5
D-F4 8mm nozzle	15	50	8	600	40.7
E-F4 6mm nozzle	15	60	3	550	31
F-F4 6mm nozzle	15	75	6	550	37.3
G-SG100	18	90	35[a]	590	35.8
H-HVOF	80	20 (N_2)	6.8 fuel*1740 O_2		